

**OPTIMIZATION TECHNIQUE FOR DESIGN OF AUTOMOTIVE
AIR FILTER HOUSING WITH IMPROVED
FLUID DYNAMIC PERFORMANCE**

By

Abdel Salam Al-Sarkhi

Master of Mechanical Engineering

Jordan University of Sciences & Technology

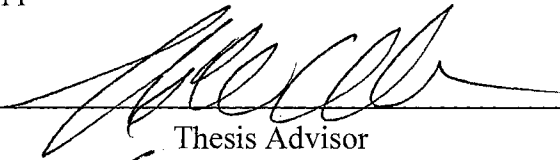
Irbid, Jordan

1993

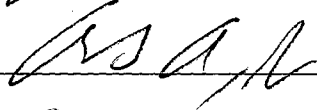
Submitted to the faculty of the
Graduate College of the
Oklahoma State University
In partial fulfillment of
The requirements for
The Degree of
DOCTOR OF PHILOSOPHY
December, 1999

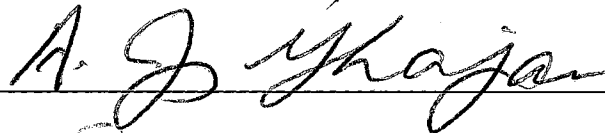
**OPTIMIZATION TECHNIQUE FOR DESIGN OF AUTOMOTIVE
AIR FILTER HOUSING WITH IMPROVED
FLUID DYNAMIC PERFORMANCE**

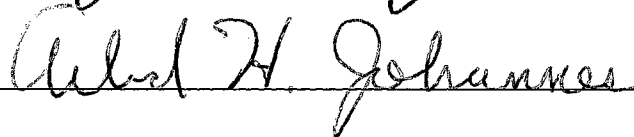
Thesis Approved:

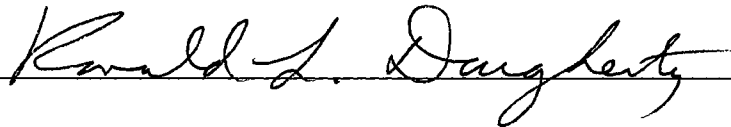


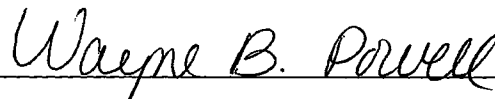
Thesis Advisor











Dean of the Graduate College

ACKNOWLEDGMENTS

Praise be to Allah, the Cherisher and Sustainer of the worlds.

I would like to take this opportunity to thank and to express my sincere appreciation to my major advisor, Dr. F. W. Chambers, for his continuous support and motivation. His invaluable guidance, encouragement and help will stay unforgettable throughout my life. I admire Dr. Chambers for his honesty and characters toward people. I am also thankful to Dr. R. L. Dougherty my first graduate advisor, I will never forget his help during the first few weeks I came to Stillwater, his help and support through my program is appreciated. Dr. A. J. Ghajar, your help is appreciated. I enjoyed your courses and remarks. I thank Dr. A. Arena for his smart ideas and suggestions. I learned much from his class; he was a very good teacher. I am also thankful to Dr. A.J. Johannes for all his great suggestions and remarks and as the undergraduate students say “Yes A. J.” I would say “Yes A. J.” too.

Specials thank to my dear friend and brother Dr. K. Gassem for his support and help. A thank-you is extended to my colleague, S. H. Yao for his cooperation and help. I would also like to thank James Davis and other MAE North Lab personnel for their support.

I extended my appreciation to the Purolator Products, Inc. and Oklahoma Center for the Advancement of Science and Technology (OCAST) for their financial support.

Finally I would like to thank the people who gave me the pure and true love, my parents, brothers and sisters.

TABLE OF CONTENTS

Chapter	Page
1. INTRODUCTION.....	1
1.1 BACKGROUND.....	1
1.2 LITERATURE REVIEW	4
1.2.1 Heat exchanger header design	4
1.2.2 Inverse method.....	8
1.2.3 Filter and filtration theory.....	14
1.2.4 Filtration efficiency models	15
1.3 OBJECTIVES OF THIS RESEARCH	20
2. THEORETICAL APPROACH.....	22
2.1 NUMERICAL TECHNIQUES	22
2.2 CFD ROUTINE	24
2.2.1 Governing equations	25
2.2.2 Finite difference equations.....	27
2.2.3 Initial and boundary conditions	31
2.2.4 Solution procedure.....	32
2.2.5 Numerical stability considerations.....	34
2.3 OPTIMIZATION ROUTINE	36
2.3.1 A nonlinear least square problem	36
2.3.2 Numerical methods and subroutines.....	37
2.3.3 Solution procedure	39
2.4 CONVERGENCE CRITERIA	42
2.5 FILTRATION MODEL.....	44
2.5.1 Combined particle efficiencies	45
2.5.2 Interception model	46
2.5.3 Inertial impaction model.....	47
2.5.4 Combined interception and inertial impaction model.....	48
2.5.5 Adhesion model	49

2.5.6	Application of the efficiency model	50
2.5.7	Summary of filtration efficiency approach and assumptions	52
3.	EXPERIMENTAL APPROACH	54
3.1	FLOW FIELD	55
3.2	FILTER and FILTER HOUSINGS	57
3.2.1	Stage 1: Five different housing configurations.....	57
3.2.2	Stage 2: Housing configuration of the optimized model	60
3.2.3	Coordinate system and experimental grid points.....	61
3.3	LDA SET UP FOR VELOCITY MEASUREMENTS.....	62
3.3.1	Data and LDA signal processing parameters.....	64
3.3.2	Set up for pressure measurements.....	65
3.3.3	Procedure for taking pressure measurement data	66
4.	RESULTS AND DISCUSSIONS.....	68
4.1	MEAN VELOCITY DISTRIBUTIONS.....	72
4.1.1	Axial velocities	73
4.1.2	Normal velocities	75
4.2	RMS VELOCITY FLUCTUATION DISTRIBUTIONS.....	81
4.3	EFFECT OF FILTER RESISTANCE ON VELOCITY DISTRIBUTION.....	83
4.4	COMPARISONS OF MEAN VELOCITY DISTRIBUTIONS ON HOUSING AXIAL CENTERLINE	85
4.5	OPTIMIZED MODEL RESULTS FOR THE CASE OF LAMINAR FLOW.....	88
4.5.1	Optimization program results	88
4.5.2	Laminar flow velocity distribution results.....	89
4.6	OPTIMIZED MODEL PRESSURE MEASUREMENT RESULTS	95
4.6.1	Pressure distribution in the inlet plenum of housing	96
4.6.2	Pressure distribution in the exit plenum of housing.....	102
4.6.3	Pressure drop across the filter (filter only)	107
4.7	COMPARISON OF PRESSURE DROP ACROSS THE FILTER FOR CALCULATED AND EXPERIMENTAL MEASUREMENTS.....	112
4.8	CALCULATED CLEAN FILTER EFFICIENCY DISTRIBUTIONS...	114

4.8.1	Tangential inlet housings	115
4.8.2	Normal inlet housing.....	123
4.8.3	Optimized tangential inlet housing	126
4.9	CALCULATED OVERALL CLEAN FILTER EFFICIENCY	129
5.	MODEL EVALUATION AND DATA VALIDATION	135
5.1	FLOW UNIFORMITY CRITERIA.....	135
5.2	STATISTICAL ANALYSIS OF THE OPTIMIZATION PROGRAM RESULTS	141
5.3	STATISTICAL ANALYSIS OF THE LDA RESULTS FOR RANDOM TESTS.....	142
5.3.1	Repeatability results.....	143
5.3.2	Percentage of deviations	146
6.	CONCLUSIONS AND RECOMMENDATIONS.....	150
6.1	CONCLUSIONS.....	150
6.2	RECOMMENDATIONS.....	152
	REFERENCES.....	153
	APPEENDICES	158
	APPENDIX A: AXIAL VELOCITY DISTRIBUTION	159
	APPENDIX B: NORMAL VELOCITY FLUCTUATION	163
	APPENDIX C: OPTIMIZATION MODEL RESULTS	166
	APPENDIX D: PRESSURE MEASUREMENT RESULTS	168
	APPENDIX E: MEAN VELOCITY DISTRIBUTION AT DIFFERENT HEIGHTS	176
	APPENDIX F: COMPARISON OF TWO OPTIMIZED PROFILES	178

LIST OF TABLES

Table	Page
Table 3.1: Filter Specifications	57
Table 4.1 Reynolds numbers- Flow rate conversions.....	72
Table 4.2: Pressure taps and axial locations	96
Table 4.3: Predictions of overall efficiencies for clean filter.....	134
Table 5.1: Statistical parameters of LDA case study (212 m ³ /hr)	149
Table C.1: Optimization program output results	167
Table F.1: Statistical parameters of two profiles resulting from the optimization program	178

LIST OF FIGURES

Figure	Page
Figure 1.1: Tangential entrance housing with angled wall	3
Figure 1.2: Heat exchanger header configurations	5
Figure 1.3: Particle capture mechanisms in gas filtration (Grant, et al. (1988)).....	19
Figure 2.1: Outlet plenum configuration	23
Figure 2.2: Inlet plenum configuration	23
Figure 2.3: Inlet flow distributions	25
Figure 2.3: The cells of the computational domain	27
Figure 2.4: The finite difference variables arrangement in a cell	28
Figure 2.5: Boundary conditions on the boundary cells of the angled wall	32
Figure 2.6: Flow chart of the optimization routine	40
Figure 2.7: Stokes number dependence of filter efficiency estimated with model of interception and inertial impaction filtration for typical filter parameters	51
Figure 3.1: Flow field set up for normal entry housing	55
Figure 3.2: Coordinate system and filter housing configurations.....	58
Figure 3.3: Tangential entry model; mixing box, entrance duct, and housing	59
Figure 3.4: Detail dimensions of the optimized model (dimensions in mm)	60
Figure 3.5: Pressure tap spacing details (dimensions are in mm).....	60
Figure 3.6: Pressure hole details in side wall of the housing (dimensions are in mm).....	61
Figure 3.7: Grid points and coordinate system	62

Figure 3.8: Fiber Drive schematic diagram	64
Figure 3.9: Schematic diagram of coupler arrangement.....	64
Figure 3.10: Schematic of pressure transducer setup.....	66
Figure 4.1: Tangential inlet housing (code TIH)	68
Figure 4.2: Tangential inlet housing with step (code TISH)	69
Figure 4.3: Tangential inlet housing with angled wall (code TIAH).....	69
Figure 4.4: Tangential inlet housing with step and angled wall (code TIASH)	69
Figure 4.5: Normal inlet housing (code NIH).....	70
Figure 4.6: Optimized housing geometry (code OTIH).....	70
Figure 4.7: Filter only and filter with an additional sheet arrangement.....	71
Figure 4.8: Axial velocity distributions in TIH model 13 mm above filter	74
Figure 4.9: Axial velocity distributions in NIH model 13 mm above filter	74
Figure 4.10: Normal velocity distributions in TIH model 13 mm above filter.....	76
Figure 4.11: Normal velocity distributions in OTIH model 8 mm above filter.....	77
Figure 4.12: Normal velocity distributions in NIH model 13 mm above filter	77
Figure 4.13: Normal velocity distributions in TISH model, 22 mm above filter	78
Figure 4.14: Normal velocity distributions in TISH model 13 mm above filter	78
Figure 4.15: Normal velocity distributions in TIASH model 13 mm above filter	79
Figure 4.16: Normal velocity distributions in TIAH model 13 mm above filter.....	79
Figure 4.17: Normal velocity distribution in OTIH model, 8 mm filter.....	80
Figure 4.18: Normal velocity fluctuation in TIH model, 13 mm above filter	82
Figure 4.19: Normal velocity fluctuations in OTIH model 8 mm above filter.....	82
Figure 4.20: Axial velocity distribution in model TIAH without filter	84
Figure 4.21: Normal velocity distribution in model TIAH without filter.....	85

Figure 4.22: Axial velocity distribution at centerline of filter	86
Figure 4.23: Normal velocity distribution at centerline of filter.....	87
Figure 4.24: Computed pressure distribution resulting from housing design optimization program.....	89
Figure 4.25: Axial velocity distribution 8 mm above filter (laminar flow).....	90
Figure 4.26: Axial velocity distribution 8 mm above filter with an additional sheet (laminar flow)	90
Figure 4.27: Normalized axial velocity distributions: Calculated-Experimental	91
Figure 4.28: Normalized velocity profiles along the housing axial position.....	91
Figure 4.29: Normal velocity distribution 8 mm above filter (laminar flow, filter only)	94
Figure 4.30: Normal velocity distribution 8 mm above filter with an additional sheet.....	94
Figure 4.31: Normalized normal velocity distributions: Calculated-Experimental.....	95
Figure 4.32: Pressure drop: ambient to port 1 (inlet plenum, filter only).....	97
Figure 4.33: Pressure distributions in inlet plenum (filter only).....	98
Figure 4.34: Normalized pressure distribution in inlet plenum (filter only).....	98
Figure 4.35: Normalized pressure distribution in inlet plenum at different ports	100
Figure 4.36: Normalized pressure distributions in inlet plenum.....	101
Figure 4.37: Normalized pressure distribution in inlet plenum at different ports	102
Figure 4.38: Normalized pressure distributions in exit plenum (filter only)	103
Figure 4.39: Normalized pressure distributions in exit plenum (filter only).....	104
Figure 4.40: Normalized pressure distributions in exit plenum (with sheet).....	105
Figure 4.41: Normalized pressure distributions in exit plenum at different ports (filter with an additional sheet).....	106
Figure 4.42: Normalized pressure drop across the filter (filter only)	108

Figure 4.43: Normalized pressure distributions across the filter at different ports (filter only).....	110
Figure 4.44: Normalized pressure distributions across the filter at different flow rate (filter with an additional sheet).....	110
Figure 4.45: Normalized pressure distributions across the filter at different ports (filter with an additional sheet).....	112
Figure 4.46: Comparison of calculated-experimental results of pressure drop across filter (filter only, laminar flow)	113
Figure 4.47: Comparison of calculated-experimental results of pressure drop across filter (filter with an additional sheet, laminar flow)	114
Figure 4.48: Elemental efficiency predictions for TIH model, 1 μ m diameter particles (perfect adhesion model).....	115
Figure 4.49: Elemental efficiency prediction for TIH model, 1 μ m diameter particles (imperfect adhesion model)	116
Figure 4.50: Elemental efficiency prediction for TIH model, 10 μ m diameter particles (perfect adhesion model).....	118
Figure 4.51: Elemental efficiency predictions for TIH model, 10 μ m diameter particles (imperfect adhesion model)	118
Figure 4.52: Elemental efficiency predictions for TISH model, 1 μ m diameter particles (perfect adhesion model).....	119
Figure 4.53: Elemental efficiency predictions for TISH model, 1 μ m diameter particles (imperfect adhesion model)	119
Figure 4.54: Elemental efficiency predictions for TISH model, 10 μ m diameter particles (perfect adhesion model).....	120
Figure 4.55: Elemental efficiency predictions for TISH model, 10 μ m diameter particles (imperfect adhesion model)	120
Figure 4.56: Elemental efficiency predictions for TIAH model, 1 μ m diameter particles (perfect adhesion model).....	121
Figure 4.57: Elemental efficiency predictions for TIAH model, 1 μ m diameter particles (imperfect adhesion model)	121

Figure 4.58: Elemental efficiency predictions for TIAH model, 10 μ m diameter particles (perfect adhesion model).....	122
Figure 4.59: Elemental efficiency predictions for TIAH model, 10 μ m diameter particles (imperfect adhesion model)	123
Figure 4.60: Elemental efficiency predictions for NIH model, 1 μ m diameter particles (perfect adhesion model).....	124
Figure 4.61: Elemental efficiency predictions for NIH model, 1 μ m diameter particles (imperfect adhesion model)	125
Figure 4.62: Elemental efficiency predictions for NIH model, 10 μ m diameter particles (perfect adhesion model).....	125
Figure 4.63: Elemental efficiency predictions for NIH model, 10 μ m diameter particles (imperfect adhesion model)	126
Figure 4.64: Elemental efficiency predictions for OTIH model, 1 μ m diameter particles (perfect adhesion model).....	127
Figure 4.65: Elemental efficiency predictions for OTIH model, 1 μ m diameter particles (imperfect adhesion model)	127
Figure 4.66: Elemental efficiency predictions for OTIH model, 10 μ m diameter particles (perfect adhesion model).....	128
Figure 4.67: Elemental efficiency predictions for OTIH model, 10 μ m diameter particles (imperfect adhesion model)	128
Figure 4.68: Predictions of overall filter efficiency using measured velocity distributions and perfect adhesion model.....	130
Figure 4.69: Predictions of overall filter efficiency using measured velocity distributions and imperfect adhesion model.....	131
Figure 5.1: Flow uniformity criterion along the centerline of the filter.....	136
Figure 5.2: Flow uniformity criterion along the centerline of the filter (filter with an additional sheet, 14 m ³ /hr, Re=2,000)	137
Figure 5.3: Flow non-uniformity criterion (filter only, 14 m ³ /hr, Re=2,000).....	138
Figure 5.4: Flow non-uniformity criterion (filter with an additional sheet, 14 m ³ /hr, Re=2,000).....	139

Figure 5.5: Deviations of the computed pressures for the optimized housing from the ideal pressure distributions (numerical results)	142
Figure 5.6: Repeatability of mean axial velocity along the centerline, 13 mm above filter	144
Figure 5.6: Repeatability of mean axial velocity along the centerline, 13 mm above filter	144
Figure 5.8: Repeatability of axial velocity fluctuating component.....	145
Figure 5.9: Repeatability results of fluctuating component of normal velocity	145
Figure 5.10: Percentage of deviations of mean velocity data	148
Figure 5.11: Percentage of deviations of the fluctuation component of the velocity	148
Figure A.1: Axial velocity distributions in TISH model 22 mm above filter (filter only).....	160
Figure A.2: Axial velocity distributions in TISH model 13 mm above filter (filter only).....	160
Figure A.3: Axial velocity distribution in TIAH model 13 mm above filter.....	161
Figure A.4: Axial velocity distribution in TIASH 13 mm above filter	161
Figure A.5: Axial velocity distributions in OTIH model 8 mm above filter (filter only).....	162
Figure A.6: Axial velocity distribution in OTIH model housing 8 mm above (filter with an additional sheet).....	162
Figure B.1: Normal velocity fluctuations in TISH model 13 mm above filter.....	164
Figure B.2: Normal velocity fluctuations in TIASH model 13 mm above filter.....	164
Figure B.3: Normal velocity fluctuations in TIAH model 13 mm above filter	165
Figure B.4: Normal velocity fluctuations in OTIH model 8 mm above filter (filter only).....	165
Figure D.1: Normalized pressure drop: ambient to port 1 (inlet plenum, filter only)	169

Figure D.2: Pressure distributions in inlet plenum at different ports (filter only)	169
Figure D.3: Pressure drop: ambient to port 1 (filter with an additional sheet)	170
Figure D.4: Normalized pressure drop: ambient to port 1 (filter with an additional sheet)	170
Figure D.5: Pressure distributions in inlet plenum (filter with an additional sheet).....	171
Figure D.6: Pressure distributions in inlet plenum at different ports (filter with additional sheet)	171
Figure D.7: Pressure distributions in exit plenum (filter only).....	172
Figure D.8: Pressure distributions in exit part at different ports (filter only)	172
Figure D.9: Pressure distributions in exit plenum (filter with an additional sheet).....	173
Figure D.10: Pressure distributions in exit part (filter with an additional sheet).....	173
Figure D.11: Pressure drop across the filter (filter only).....	174
Figure D.12: Pressure distributions across the filter (filter only)	174
Figure D.13: Pressure distributions across the filter (filter with an additional sheet)	175
Figure D.14: Pressure distributions across the filter (filter with an additional sheet)	175
Figure E.1: Axial velocity distribution at different height above the filter	177
Figure E.2: Normal velocity distribution at different height above the filter	177
Figure F.1: Different housing roof profiles from the optimization program	178

NOMENCLATURE

c	filter solidity or packing density (= volume of fibers/total volume of filter)
C_c	Cunningham slip correction factor
d_f	diameter of fiber (m)
d_p	diameter of particle (m)
D_h	hydraulic diameter (m)
e	exit plenum (below filter)
g	acceleration due to gravity (m/s^2)
H	duct height
h_i	air density times the square of the duct exit velocity, ρU_i^2
i	inlet plenum (above filter)
Ku	Kuwabara hydrodynamic factor
L	filter length (m)
OF	optimized function
$P_{i,j}$	pressure in the inlet plenum above the filter at port number j, P_x
$P_{e,j}$	pressure in the exit plenum below the filter at port number j, $P_{e,x}$
R_p	particle radius (μm)
R	interception parameter, diameter ratio of particle to fiber = R_p/R_f
Re	duct Reynolds number, $\frac{\rho U D_h}{\mu}$

Re_p	particle Reynolds number, $\frac{\rho_p U D_p}{\mu}$, used in Ptak and Jaroszczyk (1990) model
R_f	radius of fiber (μm)
St	Stokes number, $\frac{C \rho_p d_p^2 U}{18 \mu d_f}$
t	time (seconds)
TIH	tangential inlet housing
TISH	tangential inlet housing with a step
TIAH	tangential inlet housing with angled wall
TIASH	tangential inlet housing with a step and angled wall
NIH	normal inlet housing
OTIH	optimized tangential inlet housing
P_e	elemental penetration ($1-\eta_e$)
U	axial velocity in x-direction (m/s)
V	normal velocity in z-direction (m/s)
u_∞	measured normal velocity upstream of the filter media (m/s)
U_i	housing inlet velocity (m/s), duct exit velocity
X	axis along the centerline of the filter
\bar{x}	vector of the shape parameters in the optimization function
X/L	normalized length, axial distance with respect to filter length
Y	axis perpendicular to the centerline of the filter
Z	axis orthogonal to filter surface
β	porosity of filter media

Δp	total pressure drop across a filter (Pa)
Δp_1	pressure drop across a clean filter (Pa)
ΔP_{filter}	change in pressure drop across a filter from inlet to exit (Pa)
η_1, η_2	independent collection efficiencies
η_{adh}	adhesion efficiency
η_{coll}	overall collision efficiency
η_e	elemental efficiency
η_{IR}	collision efficiency
η_{R}	collection efficiency
η_f	overall efficiency averaged over all of the grid points
η_s	single fiber efficiency
μ	dynamic viscosity of air (Pa s)
ρ	density of air (kg/m^3)
ρ_p	density of particles (kg/m^3)
ω	computational over-relaxation factor

CHAPTER 1

INTRODUCTION

1.1 BACKGROUND

Automotive engine and cabin air filter housings often are designed with a major consideration given to fit the available space. The automotive air filter should provide the engine with clean air, and at the same time maintain the least resistance to the airflow system. The automotive air filter located in the air intake system of the engine performs the task of separation of the dust and any other particles from the combustion air. The filter and the housing that hold the filter must perform the previous mentioned task while offering the least resistance to the flow path (least pressure drop across the filter). Since the pressure drop available across the air intake system is predetermined by the configuration of the air intake system, any excessive resistance in the filtration process would result in a reduced supply of air, which means the engine would operate at lower efficiency and provide reduced performance.

The efficiency of filtration and the pressure drop across the filter are both a strong function of aerosol velocity through the media and the particle size. The velocity distribution above and across the filter is determined by the configuration of the housing that holds the filter. Therefore, the study of the effect of the particle size and the airflow

inside the housing of the filter is very important for improvement of the automotive air filter performance.

Poon and Liu, (1997), stated different parameters that might affect the performance of automotive air filters. Some of these parameters are: the material of the filter itself (synthetic, cellulose, etc.), the pleat design of this material, type of contaminant, contaminant size range, loading and charge, driving conditions, environment, and housing design, which is the factor that is going to be examined in this research.

The actual automotive filter generally does not have a well-behaved, uniform flow. Consequently, the flow field above the filter may be very complex and not uniform with regions of large-scale recirculation and separation. Better control of this flow distribution above the filter can improve filter performance. For better filter performance the normal velocity perpendicular to the filter surface is quite important. It is the component of the air velocity which is responsible for carrying the solid particles in the airflow to the filter surface. This component should be uniform such that the complete surface area of the filter would be an effective filtration area in equal manner. What kind of filter housing could provide this type of velocity profile? So far these issues have not been studied up to the present author's knowledge. For that reason Al-Sarkhi et al. (1997) investigated experimentally the flow distribution dependence on housing geometry for tangential inlet automotive air filter housings. All these experiments were performed with the same fully developed rectangular duct flow at the entrance to the housing. Their study focused on the effects of the housing configuration on the flow distribution just upstream of the filter. For that purpose different housing configurations were studied

experimentally. Their results showed that the housing geometry of an automotive air filter could have a significant effect on the flow field upstream of the filter. The efficiency, restriction and capacity of the filter are affected by the mean velocity distribution entering the filter and the particles carried with the flow. Among four different housing geometries the results showed that the tangential entrance housing with angled wall (see figure 1) was the best, but might not be the optimal one.

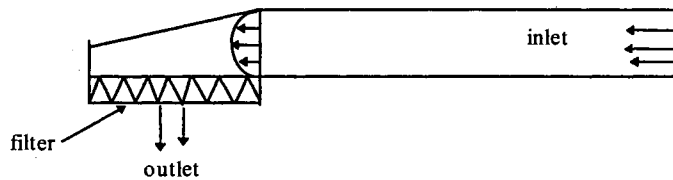


Figure 1.1: Tangential entrance housing with angled wall.

Al-Sarkhi et al. (1999) conducted a study of the effect of vehicular air filter housing configuration and filter resistance on filter flow distributions and filtration. The objective of this research was to evaluate effects of filter resistance and filter housing geometry on the filter flow distribution and initial efficiency. This objective was motivated by the problems that can arise from designing filters for uniform face velocities and installing them in housings providing non uniform velocities. The magnitudes of flow distribution effects on filter performance have been unclear. Experiments have been performed measuring velocity distributions with a Laser Doppler Anemometer just upstream of the filter location in simple housings with and without the filter installed. Predictions of local filter efficiency were performed over the cross section of the filter using the measured velocities with a simple filtration model. The results of the study include measured velocity distributions, predicted local filter efficiency distributions over the filter cross section, and overall filter efficiencies. The results show that filter resistance and housing

geometry can have large effects on the flow field. The efficiency predictions suggest that these factors can have a significant, though lesser, effect upon installed filter efficiency, particularly for smaller particles. The results suggested that the housing geometry might be used to tailor the flow distribution through the filter to improve filter performance. The idea of applying inverse design method to the problem of housing design came to mind and appeared worthy of investigation.

The present flow is analogous to a single-pass parallel flow compact heat exchanger header, which is going to be discussed in the first subsection of the literature review section.

1.2 LITERATURE REVIEW

1.2.1 Heat exchanger header design

In energy conversion systems involving gas flow heat exchangers (for example the regenerative cycle gas turbine engine) the header configurations have an ultimate effect on system envelope geometry. If the pressure drop across the core (core is analog to a filter, London, et al. (1968)) is not uniform the flow distribution above the transfer surfaces will not be uniform and a great reduction in heat exchanger performance will be obtained. The best design of the header is the one, which provides uniform flow with acceptable geometry. As a result the flow distribution uniformity above the core face is the dominating factor of the header design.

London, et al. (1968) conducted analysis to find the best header design for heat exchangers. His analysis was based on Heyda (1960). Models used in this work consist of a parallel duct connected with an inlet part which is the one above the matrix (matrix or

core is similar to the filter in our case) similar to Figure 1 and outlet part which is below the matrix fixed as a rectangular shape duct. The outlet part is mounted in either two ways. The first allows the flow in the same direction as the inlet called a parallel flow arrangement. The second lets the flow go in the opposite direction of the inlet, called the counter flow configuration as illustrated in Figure 1.2.

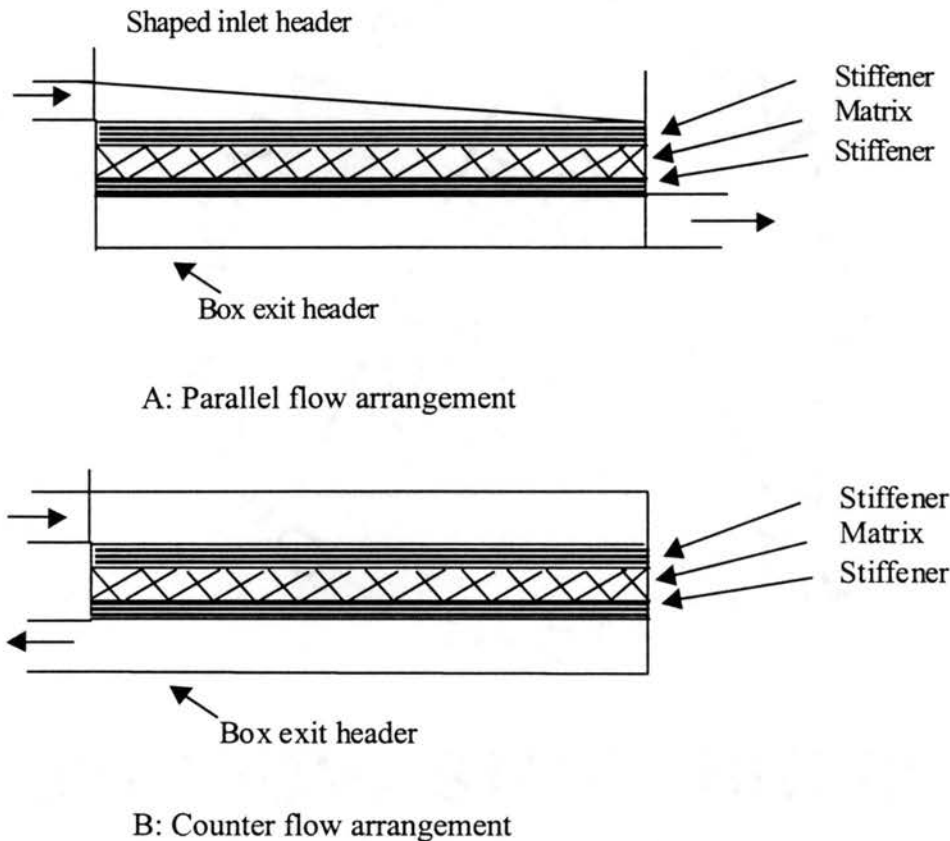


Figure 1.2: Heat exchanger configurations (London et al. (1968))

The outlet pressure profile is derived for a uniform velocity distribution leaving the matrix, assuming pressure a function of X only, but allowing the stream velocity to be a function of X and Y coordinates. X is the axial distance from the inlet to the endwall of the header divided by the length of the header L , Y is the orthogonal axis on X . The inlet header shape is selected to provide a $P(X)$ (pressure as a function of x -coordinate) which

matches the header pressure distribution profile, this will maintain a constant ΔP_{matrix} and a uniform normal velocity distribution through the matrix. The analysis started from the outlet part as follows: The outlet pressure profile is derived for a uniform velocity distribution leaving the matrix from the Euler equation for steady, constant density, inviscid flow ($-\frac{\partial P}{\partial y} = \frac{\rho}{g_c} (u \frac{\partial v}{\partial x} + v \frac{\partial v}{\partial y})$). P as a function of x only condition was imposed on the Euler equation. After integration of the Euler equation along a streamline, the Bernoulli equation for incompressible flow was obtained. The assumption that the velocity in the inlet part is only function of x makes the inlet velocity (u_i) equal to the velocity entering the matrix (porous media). The previous assumption makes the analysis simple and achievable. The continuity principle ($-u.dy = v.dx$) was applied for a constant density to the stream tube bounded by streamlines and substituted into Bernoulli equation yielded to an improper integral equation which has been solved by Heyda (1960). By applying the solution to a box outlet shape, the pressure distribution in the outlet part was derived. So far four conditions have been imposed to the solution: constant density flow, the flow through the matrix is uniform, pressure is a function of x only and inviscid flow. Now the same equations (Bernoulli and continuity) were applied to the inlet part and a new equation for the pressure distribution in the inlet part was derived. The pressure equation for the inlet part has to match that of the exit part. Combining the two pressure distribution equations provided a closed form solution of the desired inlet header shape. The specifications involved in this technique were as follows: first, constant density flow, second, both pressure and velocity were essentially functions of x only, third, inviscid flow assumption, fourth, the entering flow to the inlet part was uniform, and the pressure distribution profile matched that of the exit box header.

Cabuk and Modi (1989) developed an algorithm to find optimum shapes for two-dimensional potential flow through the header. They defined the optimum shape for a 90-degree turn flow header producing minimum flow non-uniformity at the heat exchanger core surface. The minimized function was the non-uniformity and it was minimized with respect to the variation of the inner wall boundary, fixing the upper wall as a 90-degree turn. Numerical solutions of these shapes were achieved using a boundary integral equation method for the flow in this 90-degree turn.

Araya and Modi (1988) proposed a new algorithm for design of an optimum header shape for two-dimensional inviscid irrotational flow. The goal was to find the optimum oblique flow header profile that yields a desired downstream flow field. To make full use of the active surface of the heat exchanger an inlet header design that provides uniform flow through the resistance is desirable. The algorithm is based on calculation of the first variation of the downstream flow due to system boundary variation. The computation of this variation is implemented utilizing the same boundary element method procedure as that for the calculation of two-dimensional potential flow. The optimum profile is the domain that minimizes an objective function (in their case the non-uniformity of the exit flow) that depends on the domain by a boundary value problem (in this case the potential flow) defined on the domain.

1.2.2 Inverse method

Optimal shape design in applied aero-thermodynamics is one of the most important challenges of the CFD field, since the development of this technique will reduce the required human expertise and the cost for the best design. Also this will increase the reliability and quality of the design product itself. The inverse problem for internal flow is invoked for determination of the shape of the walls of a duct once the pressure or velocity distribution is prescribed. Stanitz (1953) is one of the oldest studies of the inverse problem. His case was two-dimensional potential compressible or incompressible flow. By employing the potential function and stream function as independent variables, he derived the inverse potential flow equations. Stanitz (1980) extended his original 2-D potential inverse method to three-dimensional flows. His method applies for both external and internal flow fields. The velocity distribution is prescribed as a function of arc length along streamlines on the boundary of the flow field, $q(s)$ where s is the distance along the streamlines on the boundary. The relation between the velocity potential, $\phi(s)$, and the velocity distribution, $q(s)$, was used ($\phi(s) = \int q(s).ds$). At the end the prescribed velocity distribution $q(s)$ on the boundary of the unknown shape, becomes the prescribed velocity distribution in terms of ϕ or $q(\phi)$ along the known curvilinear coordinate ϕ . Two stream functions in a curvilinear coordinate were introduced ($\psi(x,y,z)$ and $\eta(x,y,z)$). Unbranched ducts with uniform velocities at the upstream and downstream boundaries and with arbitrary prescribed velocity distributions along streamlines on the lateral boundaries were considered. After solving the partial differential equation of the prescribed velocity distribution using the finite difference technique, the designed shape was prescribed accordingly. By

prescribing the velocity along the lateral boundary, the boundary-layer separation losses and the shock losses in compressible flow and cavitation in incompressible flow can be avoided. Stanitz (1988) reviewed his work on inverse methods for the design of ducts when the velocity distribution is prescribed on the boundaries, for two or three-dimensional potential flows.

Zannetti (1980) produced a time-dependent method for solving the inverse problem for internal flows. His objective was to find a numerical method to design ducts with known pressure distribution at the walls. This method is applicable for two dimensional or axisymmetric inviscid compressible flows, and it was based on the time dependent technique. In this inverse problem a duct with movable and impermeable wall were considered. The shape of this wall can vary with time, but the pressure on it was fixed and specified as a boundary condition. During the transient the movable wall moves in a wavy fashion until it reaches the steady state shape that satisfies the prescribed pressure distribution. The pressure distribution was given as a function of a spatial variable. The details of how the inlet and exit surfaces behave during the flow and the algorithm used on these boundaries are described in Pandolfi (1978).

Dedoussis et al. (1993) produced an inverse design method for 2-dimensional, rotational, incompressible internal flow. The problem can be stated as follows: given a prescribed-target-velocity distribution along the solid boundaries and along the inlet and outlet of a channel, as well as prescribed entropy variation along the inlet, determine its geometry. In most of the cases, inverse methods assume that the flow is both inviscid and

irrotational but Dedoussis et al. (1993) did his experiment for rotational, inviscid flow. The method is based on the stream function - potential function formulation and according to the Clebsch formulation, the velocity vector V is decomposed to a potential and rotational part. The velocity equations were solved in conjunction with a transport equation.

Dedoussis et al. (1995) produced a 3-D methodology applied for designing axisymmetric ducts. An inverse technique was used to design a duct using inviscid potential flow. Their method depends on stream function / potential function formulation. The main advantage of this method is that the geometry and the flow field are decoupled, i.e., after the flow field is determined, the geometry of the duct is computed independently. The equation for the velocity magnitude is provided by another equation. For aspect ratio of the cross section of the elementary stream tube, a new variable t is defined as an aspect ratio of cross-section ($\phi = \text{constant}$). The elementary stream tube is defined by stream surfaces ψ and η . Finally, two equations have been derived, velocity equation (V) and aspect ratio (t) equation. These two equations provide the flow solution. The derived t -equation is a strongly coupled mode with the main V -equation, so in this case the need of iteration between the flow field and geometry solution is reduced and the stability becomes much better than Stanitz (1980). Basically, the t -equation represents an equation of a local radial distance of the cross section of the duct.

Bokar and Ozisik (1995) conducted an inverse problem to estimate the time varying inlet temperature of a thermally developing, hydrodynamically developed laminar flow between parallel plates. The inlet temperature is estimated by knowing the temperature down stream of the entrance by using a single thermocouple located there. In

this transient problem, tests were also taken at different locations of the thermocouple down stream. Their estimations were more accurate when the thermocouple was placed near the entrance. The inverse analysis used in this work was based on utilization of the conjugate gradient method of minimization, which needs the solution of the direct problem, the sensitivity problem and the adjoint problem as discussed in references mentioned in their article. When the inlet temperature distribution is known, this is a well-posed problem, which is the direct problem. When the inlet temperature distribution is unknown this is the inverse problem, which is ill posed and will be determined from the measurement of the temperature downstream. The three problems are described in details in this reference.

Liu and Ozisik (1996) extended the work on laminar flow in Bokar and Ozisik (1995) to turbulent flow and studied inverse analysis of transient turbulent forced convection heat transfer inside parallel plate ducts. The inverse problem was to estimate the unknown boundary heat flux from the knowledge of time varying readings taken at a certain location. The solution of this inverse problem was done by minimization of a defined residual function $J(Q)$ such that $J(Q) = \int_0^{t_f} (\Theta - Z)^2 dt$ where Θ is the temperature computed from the solution of the direct problem. The direct problem is the problem when the wall heat flux, Q , is known (by using the estimate for Q); and Z is the down stream measured temperature at the sensor location. So the inverse problem is changed into an optimization problem. Using the conjugate gradient method of optimization solved this optimization problem.

Chaviaropoulos et al. (1995) and Dedoussis et al. (1995) studied the inverse potential target pressure problem for three-dimensional steady, compressible, inviscid

and irrotational flow. The perfect gas assumption is also assumed. Their method is based on a potential function / stream function formulation. For a given prescribed target velocity distribution on the entire (inlet, outlet and lateral) boundary of a three-dimensional flow field, find the corresponding boundary shape. This 3-D inverse problem is an ill-posed problem accepting multiple solutions. Using elementary streamtubes with orthogonal cross sections reduces this multiplicity. The orthogonal stream surfaces assumption reduces the number of dependent variables by one, transforming the governing equations to an elliptic partial differential equation for the velocity magnitude and to a second order ordinary differential equation for streamtube aspect ratio. The flow field is produced by the solution of these two equations. Their approach was similar to Stanitz (1980) approach.

Selig et al. (1992) produced a generalized multipoint inverse method for designing an airfoil. Their problem was to find the airfoil shape corresponding to a specified velocity distribution. First the airfoil is divided into segments, then the velocity distribution or boundary layer development may be prescribed on all segments of the airfoil. The airfoil shape is found by coupling a potential flow, incompressible inverse airfoil method with a direct integral boundary layer analysis method. The inverse airfoil design method was based on conformal mapping. This method allows for both the design of cusped and finite trailing-edge angle airfoils. The resulting nonlinear system of equations is solved by the Newton iteration technique.

Radwan and Lekoudis (1984) studied the inverse mode for incompressible boundary layer flows over infinite swept wings. Laminar and turbulent, three dimensional boundary layer equations were solved in the inverse mode. The assumptions of an ideal

and approximate yawed cylinder were used with a modification that suppressed the oscillations in the solution. The Keller box method was used. The governing equation and the boundary conditions were used as follows: the time averaged Navier-Stokes equation with an algebraic eddy-viscosity model for the Reynolds stresses, no-slip boundary condition at the wall. The initial conditions for the inverse calculations were generated by the solutions of the boundary layer equations in the direct mode. The numerical code that was used to solve the incompressible two-dimensional turbulent boundary layer equations in the inverse mode is available in Bradshaw et al. (1981).

Radwan and Lekoudis (1986) solved the turbulent boundary layer equation for three-dimensional incompressible turbulent flow, using the inverse formulation on an ellipsoid. In this method the displacement thickness was prescribed instead of the pressure distribution to be able to handle flows with separation. The no slip condition was used as a boundary condition and the pressure terms were eliminated using the Euler equation at the edge of the boundary layer. The eddy-viscosity model was used for turbulence stresses.

Delery and Formery (1983) developed a finite difference method to solve three-dimensional turbulent boundary layer flow by an inverse technique. Their prescribed parameter was the displacement thickness or the wall shear stress components. Two transport equations and an algebraic turbulence model were used, so the Reynolds shear stresses were expressed in terms of an isotropic eddy viscosity.

Hsun et al. (1991) produced a bordering algorithm for solution of boundary-layer equations in the inverse mode. They used the tridiagonal matrix technique with some

modification. Their algorithm is based on that of Keller (1983). The formulation of the inverse problem conformed to that where the external velocity is prescribed.

1.2.3 Filter and filtration theory

Filtration is a process for separating dry dispersed particles from a dispersed fluid stream. In fibrous filtration, the dusty fluid flows into the porous medium (the filter), leaving the dust retained by the fibers. The flow field approaching the filter may be complex, with regions of large-scale recirculation and separation. Gurumoorthy (1990) and Gurumoorthy et al. (1990) have computationally predicted and measured large-scale velocity non-uniformities in filter housings. Chen et al. [38] have performed computational fluid dynamics studies of flow through pleated filters, showing that the flow through the pleats has local, small scale non-uniformities. Previous flow visualization and velocity field measurements in filter test housings performed in OSU laboratory (Sabnis et al. (1994), Newman et al. (1997)) have also revealed large-scale velocity non-uniformities. The measured velocities in these studies were used with simple models of initial filter efficiency to predict that efficiencies for real flows can vary significantly from those for uniform flows, particularly for small particles. Sabnis results showed that there is a strong dependence of the filtration efficiencies on the fluid velocities and characteristics of the aerosol particles being filtered. The measurements of Liu et al (1996) have shown that the flow distribution in filter test housings is not substantially improved as dust loading occurs. Their experiments were conducted to measure the changes that occur in the velocity distribution in the plane 12.7 mm above the filter (in the present work measurements were performed in the plane 13 mm above

filter) as it is loaded with dust. Measurements of velocity distribution were conducted for a production engine air filter in the SAE universal panel filter test housing. Tests were performed on a clean air filter, and dust loaded filters at additional pressure drops corresponding to 50, 100 and 150 percent of design terminating pressure value. The results show that dust loading does make the velocity profiles less non-uniform, but that the changes not dramatic. Thus it may be concluded that filter housings provide non-uniform flow to filters, that these non-uniform flows may alter predicted initial efficiencies, and that these effects are not reduced significantly as the filter is loaded with dust. Thus, filter performance may be improved throughout the life of the filter by designing filter housings that provide better flow distributions to the filter.

A number of simple rigorous filtration efficiency models have been developed by different investigators over the past forty years (Landahl and Herrmann, (1949); Freshwater and Stenhous, (1972); Suneja and Lee, (1974); First and Hinds, (1976); Lee and Liu, (1982); Flagan and Seinfeld, (1988); Ptak and Jaroszczyk, (1990); Brown, (1993) and many others).

Filtration efficiency is one of the most important factors in evaluating the performance of the filter. Several different mechanisms are responsible for the collection of the particles. Some of the filtration models will be reviewed in the following section.

1.2.4 Filtration efficiency models:

a. Lee and Liu (interception model)

Particle capture due to direct interception occurs when a particle, following the streamlines of the flow around a fiber cylinder, is of a finite size sufficiently large that is

touches the surface of the fiber cylinder. The single fiber efficiency due to interception η_R is defined

$$\eta_R = \left(\frac{1 - \alpha}{Ku} \right) \frac{R^2}{1 + R} \quad (1.1)$$

Where

α is the packing density (volume fraction or solidity).

R is the interception parameter, diameter ratio of particle to fiber = R_p/R_f

Ku is the hydrodynamic factor of Kuwabara flow = $-\frac{1}{2} \ln \alpha - \frac{3}{4} + \alpha - \frac{1}{4} \alpha^2$

Kuwabara flow as described by Flagan and Seinfeld (1988) is: a fiber of radius R_f is assumed to be surrounded by an imaginary cell of radius b_1 . Navier-Stokes equations for flow transverse to the cylinders were used with no-slip condition boundary condition at the surface of the fibers and zero velocity also on the surface of the b_1 cell cylinder then the flow solution in terms of the stream function ψ is:

$$\psi = \frac{u_\infty r}{2Ku} \left[2 \ln \frac{2r}{D_f} - 1 + \alpha + \frac{D_f^2}{4r^2} \left(1 - \frac{c}{2} \right) - \frac{2cr^2}{D_f^2} \right] \sin \theta \quad (1.2)$$

Where r and θ are the cylindrical coordinates. The Ku is the Kuwabara hydrodynamic factor given above, D_f is the fiber diameter, u_∞ is the velocity inside the filter.

Equation 1.1 was compared with others obtained by other investigators and it gave good agreement with them. (Lee and Liu, (1982)).

b. Landahl and Herrmann (Inertial impaction model)

Particle capture due to inertial impaction occurs when particle is unable to follow the rapidly curving streamlines because of its inertia. The efficiency of collection of an object depends principally upon the size of the particles, particle density, flowing speed, adherence to the object, and the object diameter. Landahl and Herrmann (1949) expressed their results by the following empirical relationship

$$\eta_I = \frac{St^3}{St^3 + 0.77St^2 + 0.22} \quad (1.3)$$

Where St is Stokes number

$$St = \frac{C_m \rho_p D_p^2 U}{18 \mu_a D_f} \quad (1.4)$$

Such that:

C_m is constant called Cunningham slip correction factor

U is the Velocity

ρ_p is the density of aerosol particle

D_p is the diameter of the particle

μ_a is the dynamic viscosity of the air

D_f is the fiber diameter.

c. Ptak and Jaroszczyk (Combined filtration mechanisms)

This model is the most interesting one for the present work since this adhesion model was implemented in the present work filtration model. Ptak and Jaroszczyk conducted experimental-theoretical filtration model at intermediate Reynolds numbers. Combined

theoretical efficiency equation was developed including single fiber efficiency, collection efficiency, adhesion probability factor, and filter solidity factor. The collection coefficient was calculated using dimensional analysis. Parameters responsible for dust particle adhesion and bouncing were included in the coefficient. The interference effect of neighboring fibers was represented by the solidity factor. The efficiency equation of their model was given as:

$$\eta = 1 - \exp \left\{ \frac{-4 \cdot \beta \cdot b}{\pi \cdot d_f (1 - \beta)} \left[\frac{(St - 0.75 Re^{-0.2})^2}{(St + 0.4)^2} + R^2 \right] \cdot \frac{90.6}{\beta^{0.3} (St \cdot Re_p)^{0.68} + 190} \right\} \quad (1.5)$$

Where:

β is the solidity

b is the filter thickness

St is Stokes number ($St = \frac{C_m \rho_p D_p^2 U}{18 \mu_a D_f}$)

Re is Reynolds number = $(D_f U / \nu)$, d_f is fiber diameter, U aerosol velocity and ν is the air kinematics viscosity

R is the parameter of direct interception = (dp / d_f)

Equation (1.5) is the final form of the efficiency equation after substituting all the constants. The constants in the efficiency equation were determined experimentally under the conditions: Reynolds numbers from 0.4 to 5.75 and Stokes numbers from 1 to 120. Reynolds number was defined as $(d_f U / \nu)$ and ν was the air kinematic viscosity. In finding the adhesion probability factor, which is already substituted in the efficiency equation, a dimensional analysis was performed and two dimensionless numbers were

determined. The first one is the Stokes number and the second is $(\Pi_2 = \frac{\rho_p \cdot d_p \cdot u}{\mu_o} = Re_p)$ where ρ_p is the particle density, not air density. Careful attention should be paid in order not to confuse the dimensionless number Re_p with the Reynolds number Re . The range of fiber Reynolds number and Stokes number (mentioned above) that were used to determine its empirical constants determined the limits of this model. The following conditions were used in the experiment for finding the constants in the efficiency equation: Filter media was made of polyamide and polyester fibers (fiber diameter 23-43 μm). The filter thickness was changed from 0.4 to 2 cm and solidity from 0.015 to 0.06. Tests were run at aerosol velocity from 0.4 to 2.0 m/s. The particles diameter ranged from 2.5 to 14.5 μm . The various mechanisms of filtration discussed so far and a few other mechanisms involved in air filtration are shown schematically in Figure 1.3. Gravitational settling occurs in large particles as a result of low velocities. The electrostatic forces of repulsion or deposition occur when the particles and fibers are charged relative to each other.

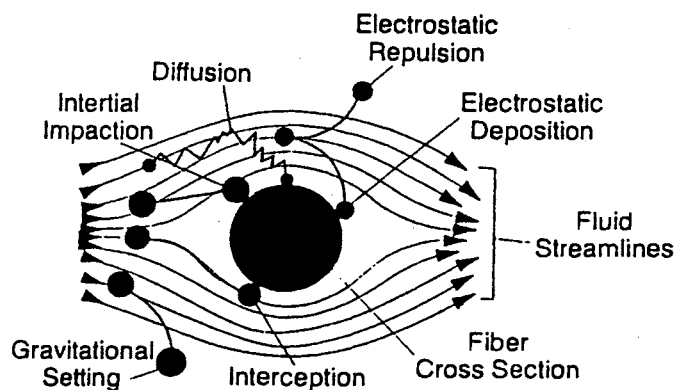


Figure 1.3: Particle capture mechanisms in gas filtration (Grant et al. 1988)

In the present filtration model the inertial impaction and interception models are considered.

In summary, the inverse techniques found in the literature have focused on finding the shape of a duct with flexible and impermeable walls once the pressure or velocity distributions are prescribed. The flow generally was inviscid and the stream function – potential function technique was used. The optimization technique was found in the literature, applied to find the optimum shape of heat exchanger headers. For this inverse technique, inviscid flow was again assumed and the stream function potential function approach was used. The present work aimed at solving a problem similar to header design using a viscous flow analysis. The optimization technique appeared to provide an appropriate approach.

1.3 OBJECTIVES OF THIS RESEARCH

Although there are has been lot of experimental and numerical work about the flow over and through the filter, the effect of housing geometry on the flow field distribution have not been reported in the literature up to the author's knowledge. In this research, first the work was focused on proving that the housing configuration may affect the flow distribution and the overall filter efficiency as well. Several housing configurations were tested experimentally to find an optimum housing geometry. The best way for achieving that goal is not to keep changing the configurations and testing them but to find out a new inverse technique to tell which is the best one then to do experimental verification for that configuration. The main goal of this research was to establish an inverse technique for finding an optimum housing geometry using a numerical technique. The problem can be

stated as follows: given inlet and outlet velocity distribution or the pressure distribution across the filter, determine the optimum housing upper wall geometry.

other goals of this research are as follows:

- To study the effect of the resistance of the filter material and its relation with the flow rate and the other important parameters like velocity and pressure distribution above the filter.
- To develop further previous filtration models and apply it to the present experimental result.

CHAPTER 2

THEORETICAL APPROACH

2.1 NUMERICAL TECHNIQUES

Numerical techniques have been studied and invoked to solve fluid flow problems for more than 100 years. Three-dimensional calculation gives a complete picture of the flow field. Sometimes, for certain purposes and certain flow fields, two-dimensional calculations give enough information that the savings in calculation time and the simplicity of the two-dimensional calculation is sufficient to make it more cost effective than the three-dimensional calculation. For the purpose of the present work, the flow inside housings similar to those in the present work could be approximated with two-dimensional calculations. Three-dimensional effects are most important at the end corners of the housing. The flow visualization we have done on a simple rectangular housing, with and without an angled wall at the end of the housing, showed the existence of complicated three-dimensional eddies at the far end corners of the housing. Otherwise the flow could be considered a nearly two-dimensional flow.

The objective of the present work is to find the shape of the housing that gives us a certain (uniform) outlet velocity distribution above the filter. So the need of the exact details of the vortices and circulation of the flow on the entire grid points, at the end

corners, in the third direction could be avoided. Recall that the equation which calculates the profile of the housing, only contains the average velocities. The velocity in the side direction (Z-direction) if it exists, will likely be only a sort of circulation near the end corners. 3-D calculations might not change the shape of the wall significantly and the 2-D calculations could be a practical way to give the optimum shape of the upper wall required. Later, in Chapter 5 the velocity distribution for laminar flow above the filter will be shown, and nearly two-dimensional behavior will be seen.

The housing of the automotive air filter used in the present work consists of two compartments, the one above the filter or the inlet plenum, and the one below the filter or the outlet plenum. In this research the outlet part of the housing was kept as a simple rectangular box shape.

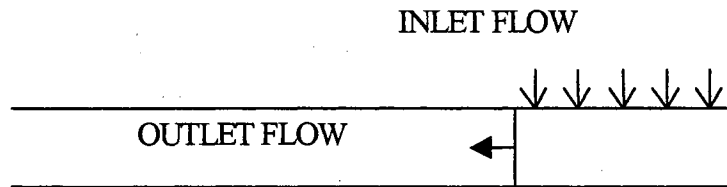


Figure 2.1: Outlet plenum configuration

The inlet part profile was changed until it attains a shape that gives a good filter flow distribution. Good filter performance requires a uniform pressure drop across the filter, which implies uniform velocity distribution.

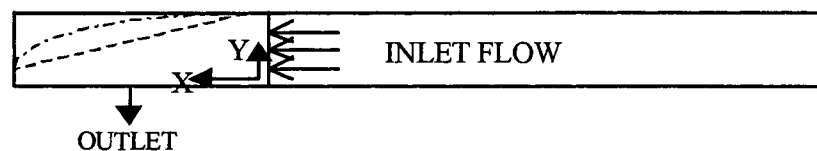


Figure 2.2: Inlet plenum configuration

A CFD code based on solving the two-dimensional Navier-Stokes equations was used in order to get the pressure distribution directly below the filter in the outlet part and along the length of the filter. For a certain shape of the inlet part the CFD model was applied to the inlet part and the pressure distribution was found directly above the filter in the inlet part, then the two pressure distributions (directly above and below the filter) were compared by an optimization routine. The optimization routine changes the shape of the profile of the inlet part until the pressure distribution directly above the filter matches the one directly below the filter. The main driving program consists of two main routines, each routine contains several subroutines and functions. The first routine contains the CFD code, which solves the Navier-Stokes equations in laminar form at Reynolds number equal to 2,000 and a function that communicates with the optimization routine to change the shape of the housing wall profile and the boundary condition on it. The second routine handles the numerical optimization problem.

In the following sections, the two main numerical routines will be discussed. First a CFD routine for solving Navier-Stokes' equation for a laminar, incompressible flow inside the housing of the filter will be discussed. Second an optimization method for finding the best shape is explained. Finally, the mechanism of coupling the routines will be discussed.

2.2 COMPUTATIONAL FLUID DYNAMICS ROUTINE

This CFD code was used to solve a time-dependent incompressible fluid flow problem. The flow was laminar (Reynolds number equal to 2,000). This routine was based on Hirt et al. (1975) technique and CFD course notes Lilley (1992). The routine

provides the pressure distribution to the optimization routine. The CFD routine will be used to solve the flow field in two parts of the housing as follows:

First: the flow in the outlet part of the housing. The outlet part was fixed as a simple rectangular box shape as shown in Figure 2.1. The inlet flow was set to be uniform flow. The outlet flow was handled as continuative outflow. On the walls the no-slip condition was used.

Second: the flow in the inlet part of the housing. Several trials have been performed to get the best shape of the upper wall profile for minimum deviations between the inlet and exit pressure (details will be discussed in the optimization routine section). The inlet flow was set to be uniform flow except at the last two cells at the boundary as shown in Figure 2.3.

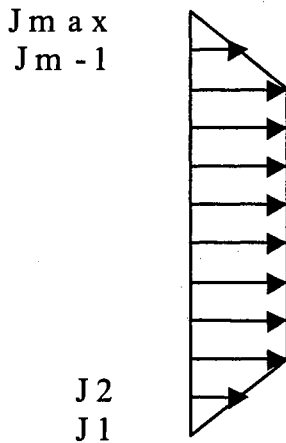


Figure 2.3: Inlet flow distributions

2.2.1 Governing equations

The governing differential equations were written in Cartesian coordinates X, Y .

The continuity equation was:

$$\frac{\partial u}{\partial x} + \frac{\partial v}{\partial y} = 0 \quad (2.1)$$

The equations of motion were the Navier-Stokes equations, given in normalized form as:

$$\frac{\partial u}{\partial t} + u \frac{\partial u}{\partial x} + v \frac{\partial u}{\partial y} = -\frac{\partial p}{\partial x} + \frac{1}{\text{Re}} \left(\frac{\partial^2 u}{\partial x^2} + \frac{\partial^2 u}{\partial y^2} \right) \quad (2.2)$$

$$\frac{\partial v}{\partial t} + u \frac{\partial v}{\partial x} + v \frac{\partial v}{\partial y} = -\frac{\partial p}{\partial y} + \frac{1}{\text{Re}} \left(\frac{\partial^2 v}{\partial x^2} + \frac{\partial^2 v}{\partial y^2} \right) \quad (2.3)$$

The velocity components u , v were in the coordinate directions x , y . P was the normalized pressure and Reynolds number Re defined as:

$$\text{Re} = \frac{UH}{\nu}$$

$$P = \frac{P}{\rho U^2}$$

$$v = \frac{v^*}{U}, \quad u = \frac{u^*}{U}$$

$$t = \frac{t^* U}{H}$$

$$x = \frac{x^*}{H}, \quad y = \frac{y^*}{H}$$

Where U is the average inlet velocity,

H is the inlet duct height

ν is the kinematic viscosity

v^* is the mean velocity in the normal direction

u^* is the mean velocity in the axial direction

t^* is the time

2.2.2 Finite difference equations

The computational domain is discretized into a mesh as illustrated in Figure 2.3

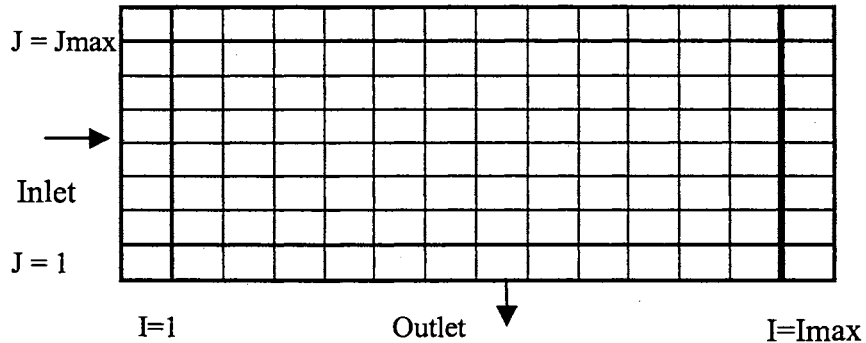


Figure 2.3 the cells of the computational domain

The boundary cells (bolded area) are fictitious (additional cells to help in fixing the boundary conditions). The staggered mesh arrangements of the cells were used for numerical solving of the above equations. The mesh consists of rectangular cells of width Δx and height Δy as shown in Figure 2.4. The angled upper wall profile of the flow field domain starts from J_{\max} to I_{\max} was controlled by a mathematical function with the cell number as a dependent variable. The upper angled wall starts from the third cell in the axial direction ($I=3, J=J_{\max}$) to give more stability to the code. The boundary condition on the angled wall will be discussed in the next section.

The length of the filter (19.3 cm) was divided into 42 grid points and the height above the filter (5 cm) was divided into 28 grid points. The grid independence test was done in the first stages of this research and this numbers of the grid showed independent

of the results on the number of grid points used. (The tested numbers of cells were from 20 to 40 cells in the x- direction and from 15 to 30 in y- direction).

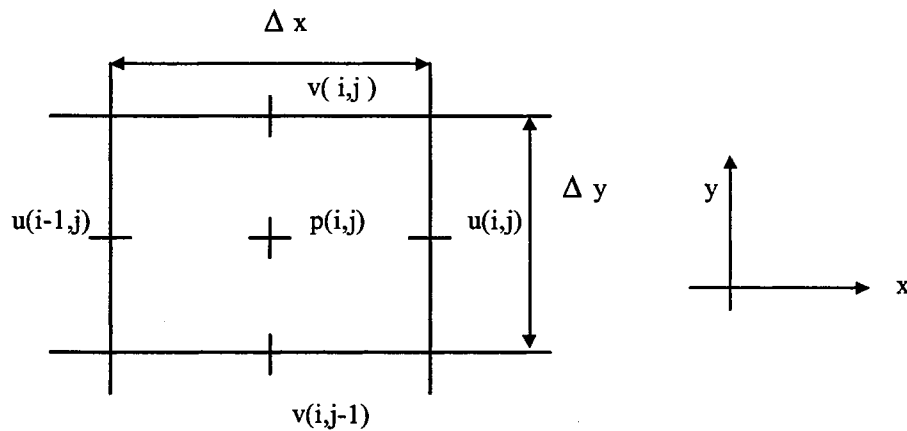


Figure 2.4 The arrangement of the finite difference variables in a cell.

The locations of the velocity components on the cell are as follows: u-velocity at the middle of the vertical sides of a cell, v-velocity at the middle of the horizontal sides of the cell, and the pressure at the center of the cell. A forward difference scheme was used for the discretization of the continuity equation and the pressure terms in the momentum equations. The convection terms in the momentum equation were discretized using the combination of the central difference and the upwind schemes. The weight of the upwind scheme is controlled by the factor α (in equation 2.4 and 2.5) when α equals zero, the convection terms will be discretized by the central scheme. It is well-known that the central scheme can have an instability problem if the selection of the time step is inappropriate, but the pure upwind scheme introduces some unnecessary calculations (Hirt et al. (1975)). The momentum equations were discretized using the explicit method

with respect to time derivatives. Discretization of equation (2.1), the continuity equation, using a forward difference scheme yields:

$$\frac{1}{\Delta x} (u_{i,j}^{n+1} - u_{i-1,j}^{n+1}) + \frac{1}{\Delta y} (v_{i,j}^{n+1} - v_{i,j-1}^{n+1}) = 0 \quad (2.4)$$

Where superscript n+1 denotes time increments after the initiation. Δx and Δy are the grid spaces in the x and y-directions for cell (i,j), respectively. The finite difference form of the momentum equations, equations 2.2 and 2.3, are:

$$u_{i,j}^{n+1} = u_{i,j}^n + \Delta t \left(\frac{1}{\Delta x} [p_{i,j}^n - p_{i+1,j}^n] + g_x - FUX - FUY + VISX \right) \quad (2.5)$$

$$v_{i,j}^{n+1} = v_{i,j}^n + \Delta t \left(\frac{1}{\Delta y} [p_{i,j}^n - p_{i,j+1}^n] + g_y - FVX - FVY + VISY \right) \quad (2.6)$$

Where the convection and the viscous terms are defined as:

$$FUX = \frac{1}{4\Delta x} \left(\begin{aligned} & \left[u_{i,j} + u_{i+1,j} \right]^2 + \alpha |u_{i,j} + u_{i+1,j}| \cdot [u_{i,j} - u_{i+1,j}] - \\ & \left[u_{i-1,j} + u_{i,j} \right]^2 - \alpha |u_{i-1,j} + u_{i,j}| \cdot (u_{i-1,j} - u_{i,j}) \end{aligned} \right) \quad (2.7)$$

$$FUY = \frac{1}{4\Delta y} \left(\begin{aligned} & \left[v_{i,j} + v_{i+1,j} \right] \cdot [u_{i,j} + u_{i,j+1}] + \alpha |v_{i,j} + v_{i+1,j}| \cdot [u_{i,j} - u_{i,j+1}] - \\ & \left[v_{i,j-1} + v_{i+1,j-1} \right] \cdot [u_{i,j-1} + u_{i,j}] - \alpha |v_{i,j-1} + v_{i+1,j-1}| \cdot [u_{i,j-1} - u_{i,j}] \end{aligned} \right) \quad (2.8)$$

$$FVX = \frac{1}{4\Delta X} \left[\begin{aligned} & (u_{i,j} + u_{i,j+1}) \bullet (v_{i,j} + v_{i+1,j}) + \alpha |u_{i,j} + u_{i,j+1}| \bullet (v_{i,j} - v_{i+1,j}) \\ & (u_{i-1,j} + u_{i-1,j+1}) \bullet (v_{i-1,j} + v_{i,j}) - \alpha |u_{i-1,j} + u_{i-1,j+1}| \bullet (v_{i-1,j} + v_{i,j}) \end{aligned} \right] \quad (2.9)$$

$$FVY = \frac{1}{4\Delta y} \left[\begin{aligned} & (v_{i,j} + v_{i,j+1})^2 + \alpha |v_{i,j} + v_{i,j+1}| \bullet (v_{i,j} - v_{i,j+1}) - \\ & (v_{i,j-1} + v_{i,j})^2 - \alpha |v_{i,j-1} + v_{i,j}| \bullet (v_{i,j-1} - v_{i,j}) \end{aligned} \right] \quad (2.10)$$

And the viscous terms are:

$$\begin{aligned} VISX &= \frac{1}{\text{Re}} \left[\frac{1}{\Delta x^2} (u_{i+1,j} - 2u_{i,j} + u_{i-1,j}) + \frac{1}{\Delta y^2} (u_{i,j+1} - 2u_{i,j} + u_{i,j-1}) \right] \\ VISY &= \frac{1}{\text{Re}} \left[\frac{1}{\Delta x^2} (v_{i+1,j} - 2v_{i,j} + v_{i-1,j}) + \frac{1}{\Delta y^2} (v_{i,j+1} - 2v_{i,j} + v_{i,j-1}) \right] \end{aligned} \quad (2.11)$$

To complete one cycle of calculation in this routine, the code does the following steps:

First, computing guesses for the new velocities for the entire mesh from equation (2.5) and (2.6). Second, modifying and adjusting these velocities iteratively to satisfy the continuity equation (equ. 2.4) by making appropriate change in the cell pressure.

Third, when convergence has been achieved, the velocity and pressure are used as initial values for the next cycle.

2.2.3 Initial and boundary conditions

The present study introduces the initial conditions as:

$$\begin{aligned} \text{At } t = 0 \\ U(x,y,t) = 0 \\ V(x,y,t) = 0 \end{aligned} \tag{2.12}$$

For the boundary conditions, the upper wall and the endwall opposite to the flow direction (left wall in Figure 2.2) are no-slip type. The inlet condition is fixed as constant (uniform flow as in Figure 2.3). The outlet condition is defined so that the V-velocity gradients with respect to y are zero. The angled upper wall is handled based on the technique of Hirt et al. (1975). A combination of the vertical and horizontal boundary condition has been performed on one cell as follows: The bottom face of the angled wall boundary cell in the present study was handled as the horizontal upper boundary of Hirt et al. (1975). The left face of the angled wall boundary cell was handled as the vertical right boundary (refer to Figure 2.5 below).

In the expression of nodal variables, the boundary conditions can be written as the following:

Inlet B.C. (left):

$$\begin{aligned} U_{1,j} = \text{constant (as specify in Figure 2.3)} \\ V_{1,j} = 0 \end{aligned} \tag{2.13}$$

Outlet B.C. (bottom):

$$\begin{aligned} U_{i,1} = U_{i,2} \\ V_{i,1} = V_{i,2} \end{aligned} \tag{2.14}$$

Upper wall (no-slip) (horizontal before the angled wall):

$$\begin{aligned}
 V_{i,jm1} &= 0, V_{i,jmax} = 0 \\
 U_{i,jmax} &= -U_{i,jm1}
 \end{aligned}
 \tag{2.15 a}$$

Where $im1$ and $jm1$ are $imax - 1$ and $jmax - 1$, respectively.

Angled wall B.C.:

$$\begin{aligned}
 U^* &= 0 \\
 V^* &= 0
 \end{aligned}
 \tag{2.15 b}$$

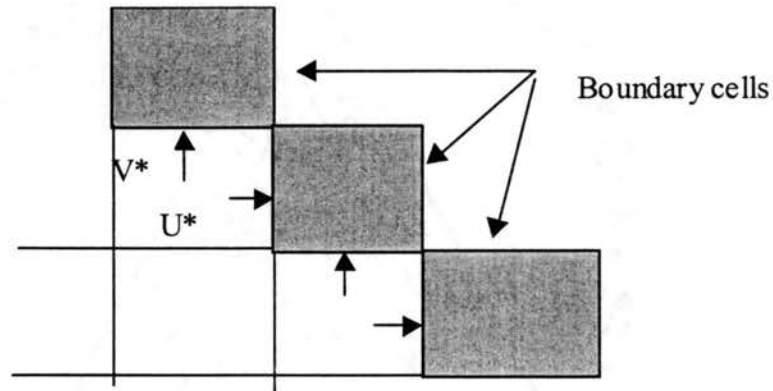


Figure 2.5: Boundary conditions on the boundary cells of the angled wall

2.2.4 Solution procedure

Because of the nonlinear nature of the equations governing the fluid flow inside the housing, the solution procedure must be iterative. Velocities are solved first by equations (2.5) and (2.6) and then pressures are obtained. However, the iteration cannot bring the velocities to satisfy the continuity equation unless the pressure cell has been adjusted. The adjustment of the pressure cell has been used in the SOLA algorithm (Hirt et al. 1975) to obtain better-estimated velocities. In this method the dilatation D is expressed as:

$$D = \frac{u_{i,j}^{n+1} - u_{i-1,j}^{n+1}}{\Delta x} + \frac{v_{i,j}^{n+1} - v_{i,j-1}^{n+1}}{\Delta y} \quad (2.16)$$

The basic idea of this technique is that the pressure gradient between a cell and its ambient cells determines the net inflow or outflow for a cell. If the dilatation D in equation (2.16) is negative, the net mass flow is into the cell and increasing pressure is needed to eliminate the inflow. On the other hand, when D is positive, decreasing pressure compensates the net mass outflow. The one pressure variable in each cell allows the dilatation D to be driven to an acceptable small value. Since the adjustment of the cell will affect its neighbor cell values, the iteration of the pressure adjustment must be performed throughout the whole flow domain. The dilatation D is calculated by using the most recent updated velocity values. When a cell pressure changes from P to $P + \Delta P$, the velocity components on the four faces of that cell change as:

$$u_{i,j}^{n+1} = u_{i,j}^n + \frac{\Delta t \cdot \Delta p}{\Delta x} \quad (2.17)$$

$$u_{i-1,j}^{n+1} = u_{i-1,j}^n - \frac{\Delta t \cdot \Delta p}{\Delta x} \quad (2.18)$$

$$v_{i,j}^{n+1} = v_{i,j}^n + \frac{\Delta t \cdot \Delta p}{\Delta x} \quad (2.19)$$

$$v_{i,j-1}^{n+1} = v_{i,j-1}^n - \frac{\Delta t \cdot \Delta p}{\Delta x} \quad (2.20)$$

Substituting these equations into the continuity equation will yield the required difference pressure form:

$$\Delta p = -\omega \cdot D / \left\{ 2\Delta t \left(\frac{1}{\Delta x^2} + \frac{1}{\Delta y^2} \right) \right\} \quad (2.21)$$

Where ω is an over-relaxation factor introduced to accelerate the iteration convergence. The value of ω is chosen as 1.7 in this work. It should be noted that the ΔP is just the net pressure difference between the concerned cell and its ambient cells, assuming that the pressures are the same for the ambient cells. In the pressure iteration, the dilatation, D , is evaluated first, then ΔP and finally velocities are updated as in equations (2.17) to (2.20). Considering these equations carefully, we will find that they are new forms of the momentum equations with neglect of convection and diffusion terms ($\partial u / \partial t = \pm \partial p / \partial x$ and $\partial v / \partial t = \pm \partial p / \partial y$). However the velocity calculation is an iterative process.

2.2.5 Numerical stability considerations

The choice of grid size Δx and Δy , time increment Δt , and upstream difference parameter α will affect both the numerical solution and the stability. The grid size should be sufficiently small in order to yield accurate results. However, the exact value of the grid size depends on the dimensions of the computational domain, if the computational domain is large and the flow is slow, a relatively large grid size can be utilized. Once the mesh space is determined, the choice of the time increment must be satisfy the following two conditions (Hirt et al., (1975): first, fluid can not move more than one cell size for the given time step. This leads to the inequality:

$$\Delta t < \min \left(\frac{\Delta x}{|u|}, \frac{\Delta y}{|v|} \right) \quad (2.22)$$

Second, the non-zero value of kinematic viscosity requires that the momentum diffusion can not be over one cell size in the given time step. Then the following condition must be satisfied:

$$v \cdot \Delta t < \left(\frac{1}{2} \frac{\Delta x^2 \Delta y^2}{\Delta x^2 + \Delta y^2} \right) \quad (2.23)$$

Note that the dimension of the kinematic viscosity is m^2/s . therefore, the left and right hand sides of the inequality (2.23) have the same dimensions.

The Δt should be the minimum of the two numbers from eq. (2.22) and (2.23). However in the present study Δt was obtained by trial and error and it was much less than the numbers resulting from equations (2.22) and (2.23).

The upstream difference coefficient α applied to the convection terms of the momentum equation also has to satisfy the condition:

$$1 \geq \alpha \geq \max \left(\left| \frac{u \cdot \Delta t}{\Delta x} \right|, \left| \frac{v \cdot \Delta t}{\Delta y} \right| \right) \quad (2.24)$$

The value of α should be in the range 0 to 1. The case of α equal to 0 is equivalent to the central difference and 1 refers to the fully upwind difference. In the present study α equal to 0.12 showed good results consequently it has been used. The convergence was tested by displaying the flow rate at different sections along the housing and by comparing the difference in the velocities at all grid points from cycle to cycle. For every

two consecutive cycles the difference of the mean velocities is less than very small number (10^{-3}), more details about the convergence criteria will be discussed in section 2.4.

2.3 OPTIMIZATION ROUTINE

2.3.1 A nonlinear least square problem

A nonlinear least square problem also called “nonlinear regression” in statistics, is to solve a set of nonlinear simultaneous equations. Let a set of equations be given as

$$F_j(x_1, x_2, x_3, \dots, x_m) = y_j \quad j = 1, 2, \dots, n$$

Such that y_j are a constant. The problem can be reformulated so that a best solution is defined as follows:

Define a function $OF(x)$, (Optimized Function) as:

$$OF(\bar{X}) = \sum_{j=1}^n [F_j(\bar{x}) - Y_j]^2 \quad (2.25)$$

The nonlinear least square problem is to find a vector \bar{x} that minimizes the $OF(\bar{x})$.

A problem frequently facing engineers is the one of fitting a mathematical model to a set of experimental data. Let $f_j = f(\bar{x}, \bar{t}_j)$ be the value of the mathematical model evaluated at (\bar{x}, \bar{t}_j) where $\bar{x} = (x_1, x_2, \dots, x_m)$ is a vector of parameters and $\bar{t}_j = (t_1, t_2, \dots, t_k)$ is the i^{th} data vector of independent variables. Then let $\bar{y} = (y_1, y_2, \dots, y_n)$ be the vector of n dependent experimental data. It is assumed that the errors in y_i are uncorrelated. Let σ_i be the standard error associated with the observation of y_i . If the least square fitting strategy is employed to solve the problem of fitting the functional model to the

experimental data set (resulting from n observations of the physical process to be modeled) the problem now is to minimize the following function

$$OF(\bar{x}) = \sum_{j=1}^n \frac{(F_j - Y_j)^2}{\sigma_j^2} \quad (2.26)$$

When F is linear with respect to the parameters, \bar{x} , this is a “linear least square problem”. Here F_j is non-linear with respect to parameters \bar{x} . The \bar{x} are the parameters which are to be adjusted to make the modeling function (F_j) fit the data (Y_j) as well as possible, e.g. to make $OF(\bar{x})$ as small as possible. It could be proved that when F_j is linear in the parameters, \bar{x} , the contour surface of $OF(\bar{x})$ (surfaces on which the value of $OF(\bar{x})$ remain constant) are ellipsoids, but if F_j is nonlinear in the parameters then contour surfaces may be distorted. More details are provided by Marquardt (1963).

2.3.2 Numerical methods and subroutines

Marquardt’s method is one of the numerical methods widely used to fit a set of data. In the present work Marquardt’s method will be implemented as a numerical method for the minimization process. Jackson (1978) and Chandler et al. (1972) presented the basic idea of the code. The present numerical code consists of two main subroutines, each of them contains several functions and subroutines and one main driving program which calls the two main routines. All files and subroutines are inserted in Fortran power station software using Fortran77-programming language. The skeleton of the whole code is based on subroutines, which makes it very powerful from a sense that the user can exchange any routine without any problem. For example, the CFD code is for laminar flow. If the user has a turbulent code and wants to use it the only thing required to be

changed is one COMMON statement. Also the code has the capability to use different methods of optimization. In this section subroutine named MARQ will be explained and the related input file since MARQ subroutine is the one, which does the optimization process.

MARQ performs nonlinear least square fitting; that is it finds a local minimum of a function which can be expressed as a sum of squares of functions which may depend nonlinearly on the parameters. As a special case, it can solve a system of simultaneous nonlinear equations. In MARQ the nonlinear least square problem may be expressed as:

$$\text{Minimize} \quad PHI = \sum_{J=1}^{NPTS} \frac{[FIT(J) - Y(J)]^2}{[YSIG(J)]^2} \quad (2.27)$$

Where PHI is the function to be minimized. FIT(J) is the fitted model, which is the calculated pressure from the CFD code at a certain profile of the wall (also called $Y_c(J)$ in the code), a function which may be nonlinear with respect to some of the parameters X(k) or the parameters of the equation of the wall's profile. Y(J) is the optimum data point to be matched which in our case is the optimum pressure that matches the exit pressure distribution of the housing. YSIG(J) is the standard error associated with the ordinate Y(J). Y(J) itself could be used for YSIG(J) for the purpose of minimization of PHI in equation 2.27. It is a matter of normalizing or weighting the difference in the numerator of equation 2.27. In the present case Y(J) itself has been used for YSIG(J). In MARQ independent weighting can be used for the data observations. There is a useful property in the present technique, which is that it allows the user to "mask" certain parameters. Masking a certain parameter means allowing the user to fix a parameter at its input value. A parameter that has been masked will not vary during the computational process.

The user also may want to constrain the parameters in some manner, for example, to limit the parameters to a domain in which the fitting function is continuously differentiable or to a region in which the evaluation of the fitting function yields a real valued result. In MARQ, XMAX(I) and XMIN(I) specify the maximum and minimum values for the i^{th} parameter respectively. The initial parameter values may default to zero. The maximum and minimum constraints for each parameter default to a very large positive and very large negative numbers respectively. An MARQ convergence criterion is an absolute test upon the parameters. More details will be in the next section. This method requires that the magnitude of the change in each parameter be less than some constant.

2.3.3 Solution procedure

The solution procedure of the optimization routine and the way of communication with the other routines are presented in this section. First, the pressure distribution in the inlet plenum will be provided by the CFD routine for an initial assumed inlet roof profile. Second, comparison of the pressure distribution upstream and downstream of the filter is performed by the optimization routine. Third, the optimization routine iteratively changes the profile until the pressure distributions in the inlet plenum and exit plenum reach an acceptable match. The matched pressures imply the desired velocity distributions (the uniform distribution). The flow chart of the optimization program is shown in Figure 2.6.

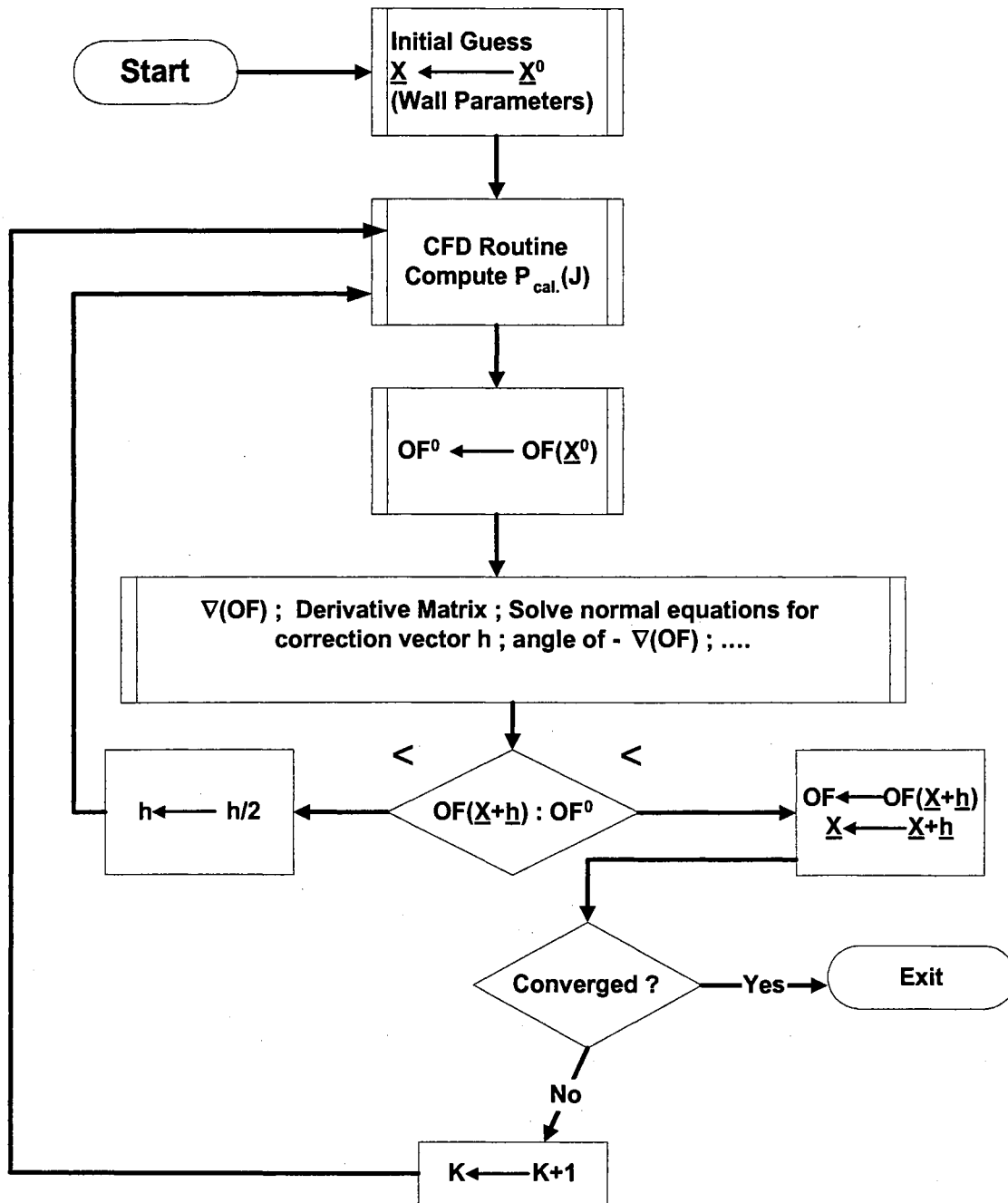


Figure 2.6: Optimization program flow chart

The user must decide the way of changing the profile, whether it is a high order polynomial or exponential or any other function containing up to 20 constants. In the

present work several shapes have been tested to find the best profiles. The linear profile showed a minimum optimized function (PHI in equation 2.27) representing a better pressure match than the other cases. Other shapes showed convergence toward the linear profile. The author decided to constrain the searching to the best linear profile that gives minimum error and best pressure match. Examples of results for other geometries are presented in Appendix G.

Later in Chapter 5, the numerical output of the optimization routine will be illustrated. In the following section some of the statistical terms used to judge how good the fitted model is will be explained:

1. The deviation of the fitted model from the optimum data point will be expressed as DEV Such that:

$$DEV(J) = Y(J) - FIT(J) \quad (2.28)$$

2. The deviation of the fitted data will be weighted by YSIG, and expressed as WDEV Such that:

$$WDEV(J) = \frac{Y(J) - FIT(J)}{Y(J)} = \frac{DEV(J)}{Y(J)} \quad (2.29)$$

3. The percentage of the weighted deviation will be noted as PDEV Such that:

$$PDEV(J) = 100 \cdot \frac{DEV(J)}{Y(J)} \quad (2.30)$$

4. The root mean square of the deviations will be RMSE Such that:

$$RMSE = \sqrt{\frac{\sum_{J=1}^{NPTS} DEV(J)^2}{NPTS}} \quad (2.31)$$

5. The average of the absolute values of the percentage of deviations will be expressed as AAPD

Such that:

$$AAPD = \frac{\sum_{J=1}^{NPTS} |PDEV(J)|}{NPTS} \quad (2.32)$$

6. The square root of the average of the absolute values of the percentage of deviations will be WRMS.

Such that:

$$WRMS = \sqrt{\frac{\sum_{J=1}^{NPTS} |PDEV(J)|}{NPTS}} \quad (2.33)$$

2.4 CONVERGENCE CRITERIA

First: CFD Routine

The convergence of the numerical solutions is controlled by two criteria. The first is the dilatation factor, D, which ensures the continuity will be satisfied always. In the CFD code, it is noticed that the maximum D is less than 10^{-4} when the iteration of every cycle is about 500 times. Therefore the number of iterations is set to be 700 to maintain the accuracy of the solution and to be on the safe side. The second criterion is the absolute difference of the mean velocity (u and v) between two successive cycles. At every cycle the difference between the new u (and v) velocity and the old u (and v) velocity at all

points was checked and printed to a file. It is found in the present study that the maximum difference (to reach the steady state) is less than 10^{-3} (m/sec) which is less than 1% of the maximum velocity when the time step Δt is 100 times less than the stability criteria mentioned in equations 2.23 and 2.24. The smaller the time step the more stable the code behaved. It is observed that an increase of the time step can cause inaccuracy of the solution and a Δt of 10^{-4} second is 200 times smaller than the stability criteria, seems to be appropriate. Liu (1994) noticed the same conclusion in his CFD predictions of flow distribution through air filters. Liu (1994) based his code on the same technique of Hirt et al. (1975) as in the present work except that in the present work a non-dimensional form of Navier-Stokes was used. In his work a uniform grid size of 10 mm, 42 and 20 cells in x- and y-direction, were used to solve a turbulent flow. In the present work a non-uniform grid size (5 mm by 1.78 mm), 42 and 30 cells in x- and y-direction was used to solve a laminar flow. In summary, at each time step, 700 iterations were performed to ensure the convergence at all grid points. The time was then stepped forward by Δt . The process was continued until a steady state was achieved at about 500 time steps. This represents a total elapsed time of about 1 second.

Second: Optimization Routine

The convergence criterion used in this routine is a test on the sum of squares. The primary interest is in finding the optimal parameter values, which will minimize the sum of squares (as defined in equation 2.27). In the present case in the final iteration PHI in equation 2.27 was 0.021. Another convergence criterion is an absolute test on the parameters. The requirement of this criterion is that the magnitude of the change in each

parameter be less than some small number ε (10^{-3}). In the present case the difference in the parameter in the final iteration was 0.0004. In the present case the optimization routine called the CFD routine 16 times to get the best shape.

So far the numerical calculations of the pressure distributions by the CFD routine and the housing profile by the optimization routine have been discussed. After finding the optimized shape of the housing geometry, the need for a filtration model to calculate the efficiency of the filter comes next. The efficiency of the filter inside the new housing has been predicted and compared with all other housings. In the next section the filtration model used in this work will be discussed and the approach and assumptions of the filtration efficiency calculations will be summarized.

2.5 FILTRATION MODEL

The velocity distributions measured in the various housings were used to calculate predictions of the distribution of filter efficiency over the face of the filter. The calculations were based upon the combination of semi-empirical and empirical equations for the performance of clean fibrous filters. More details can be found in Al-Sarkhi et al. (1999). The numerical code was based on that of Duran (1995) with some modifications.

The main modifications on the mentioned code were as follows. First the number of the elemental areas was increased. The filter was divided into small elemental areas with the velocity considered uniform on each area element. The number of elemental areas in the present work was 225 elements compared to 66 elements in Duran (1995). Secondly in Duran's code the normal velocities at all elemental areas were considered to be positive

or going into the filter and it did not have any velocity going out of the filter. In the present work some of the normal velocities have a negative sign or the particles are going away from the filter in some regions of the housing above the filter. In the present work zero efficiency was considered for those particles having a negative velocity sign (the particles traveling off the filter). So the velocity was set to zero for the particles having negative normal velocity (note: a negative normal velocity means that the velocity is going away from the filter, upward, and a positive sign means the velocity is going into the filter, downward).

2.5.1 Combined particle collision efficiencies

The overall particle collision efficiency, η_{coll} , (neglecting consideration of adhesion) for a fiber cylinder commonly is obtained by analyzing the mechanisms of particle collision separately and then combining the individual efficiencies, as presented by Flagan and Seinfeld (1988). For independent mechanisms of particle capture, the probability that a particle will escape capture by mechanism “i”, is: $(1 - \eta_i)$. The probability that a particle will escape capture by either of two *independent* mechanisms then is the product of the two probabilities: $(1 - \eta_1)(1 - \eta_2)$. Thus, the probability that a particle will be captured by mechanism 1 and 2 is:

$$\eta_{coll} = 1 - (1 - \eta_1)(1 - \eta_2) \quad (2.34)$$

Equation 2.34 may be expressed as $\eta_{coll} = \eta_1 + \eta_2 - \eta_1\eta_2$. Frequently one mechanism may dominate in a particular range of particle sizes and the third term, $\eta_1\eta_2$, will

approach some small value compared to the other terms. This combined efficiency assumes that the mechanisms of particle capture are independent. Although combining collection by interception and inertial impaction as independent is not thoroughly rigorous, it is a very good approximation that has been demonstrated by Newman (1994) to agree well with other efficiency models developed from empirical data. These filtration mechanisms are approximated as independent in the efficiency calculations presented here.

2.5.2 Interception model

To predict particle capture due to interception, Lee and Liu's (1982) equation has been used. This equation approximates the single fiber collection efficiency, η_R , for the Kuwabara (1959) flow field as:

$$\eta_R = \frac{1 - c}{Ku} \frac{I_p^2}{1 + I_p} \quad (2.35)$$

where Ku is the Kuwabara hydrodynamic factor

$$Ku = c - \frac{3}{4} - \frac{c^2}{4} - \frac{1}{2} \ln c \quad (2.36)$$

I_p is the interception parameter, the ratio of particle to fiber diameter or radius, and c is the packing density.

$$I_p = \frac{D_p}{D_f} = \frac{R_p}{R_f} \quad (2.37)$$

Lee and Liu's approximation is based on a small value of I_p . The Kuwabara flow field is a Stokes flow solution, that is, one based on fiber Reynolds number much less than 1.

2.5.3 Inertial impactation model

To predict particle capture due to inertial impactation, we have used Jaroszczyk and Wake's (1991) version of Landahl and Herrmann's (1949) equation for the efficiency of an isolated fiber. This equation was corrected to the case of a single fiber within an array of fibers using the "solidity factor" of Ptak and Jaroszczyk (1990). The resulting inertial impact efficiency equation is:

$$\eta_I = \frac{SF \cdot St_c^3}{St_c^3 + 0.77St_c^2 + 0.22} \quad (2.38)$$

St_c is the Stokes number corrected for slip,

$$St_c = C_c St = \frac{C_c R_p^2 \rho_p u_\infty}{9\mu R_f} \quad (2.39)$$

with C_c the Cunningham correction factor for slip,

$$C_c = 1 + 1.257Kn \quad (2.40)$$

Kn is the Knudsen number, the ratio of molecular mean free path to particle radius,

$$Kn = \frac{\lambda}{R_p} \quad (2.41)$$

and SF is the solidity factor,

$$SF = \frac{0.9}{c^{0.3}} \quad (2.42)$$

Suneja and Lee (1974) indicate that the Landahl and Herrmann equation is based upon calculations at a fiber Reynolds number of 10. Ptak and Jaroszczyk evaluated the solidity factor equation based upon experimental results for packing density, c , in the range from 0.015 to 0.06.

2.5.4 Combined interception and inertial impaction model

Then, combining the models of interception and inertial impaction and approximating them as independent, the collision efficiency equation becomes:

$$\eta_{IR} = 1 - \left(1 - \frac{1-c}{Ku} \frac{I_p^2}{1+I_p} \right) \left(1 - \frac{SF \cdot St_c^3}{St_c^3 + 0.77St_c^2 + 0.22} \right) \quad (2.43)$$

This equation provides the efficiency for collision and would represent the particle capture efficiency if all particles that came into contact with the filter fibers remained attached to the fibers, that is, if there were perfect adhesion. In reality, not all particles that contact the fibers remain attached, for some bounce off.

2.5.5 Adhesion model

Ptak and Jaroszczyk (1990) recognized the importance of distinguishing the difference between collection efficiency and collision efficiency. The difference is associated with the momentum of the solid dust particles and their adhesion to the fiber surface. Collection efficiency refers to the amount of particles collected, adhered, and retained by the fibers, whereas, collision efficiency refers to the amount of particles merely making contact with fiber. Ptak and Jaroszczyk refer to η_{adh} as the adhesive probability factor or adhesion efficiency and present the collection efficiency, η_s , as the product of the collision efficiency and the adhesion efficiency:

$$\eta_s = \eta_{IR} \cdot \eta_{adh} \quad (2.44)$$

Ptak and Jaroszczyk present the following model for the adhesion efficiency:

$$\eta_{adh} = \frac{190}{(\text{Re}_p \cdot St_c)^{0.68} + 190} \quad (2.45)$$

They indicate that the equation was accurate over a range of Stokes numbers from 1 to 120 and fiber Reynolds numbers from 0.4 to 5.75 for the experiments used to determine its empirical constants. Note that particle Re_p is calculating using the particle density and diameter. Efficiency calculations were performed for both cases, imperfect adhesion and assuming perfect adhesion, $\eta_{adh} = 1$.

2.5.6 Application of the efficiency model

The velocities measured with the LDA upstream of the filter were used to calculate aerosol velocities through the filter media. The measured velocities were assumed locally uniform in a small area surrounding each measurement point. This velocity was converted to the much lower (1:19.2) filter face velocity assuming locally uniform flow over the entire unfolded area of the filter pleats. The face velocity then was converted to the velocity through the filter media using the packing density to account for the solid volume fraction of the filter. Based upon information provided by the filter media producer, the filter was modeled using a packing density, $c = 0.23$, and a single weighted average fiber diameter of $38 \mu\text{m}$. These values were chosen based upon the media producer's description, but other means could be used to infer different parameters that might be more representative of the performance of the filter. See Duran (1995) for a discussion of other approaches to choosing filter parameters for this model. Nevertheless, these parameters are believed to yield a good representation to the overall performance of the filter.

The single fiber efficiency, η_s , that results from the model is integrated across the thickness of the filter, h , using the standard approach, as described by Crawford (1976). The integration yields the following equation for what we have termed the elemental efficiency, η_e , that represents the filtration efficiency of the small area element of the filter centered on one of the measured velocities:

$$\eta_e = 1 - \exp\left(-\frac{2c\eta_s h}{\pi(1-c)R_f}\right) \quad (2.44)$$

The Stokes number dependence of the efficiencies predicted by these equations for perfect and imperfect adhesion is illustrated in Figure 2.6. This figure was calculated for the condition used in the model, for the case of a $3.8 \mu\text{m}$ diameter particle. The particle density is 2723 kg/m^3 for all calculations presented here. The figure illustrates the rapid increase in efficiency as the Stokes numbers increase from 0.1 to 1.0. The decrease in efficiency due to imperfect adhesion is noticed at Stokes numbers greater than 1. Note that if diffusive filtration were accounted for, an efficiency increase would appear at the lowest Stokes numbers. Diffusive filtration is not considered significant for the conditions of this study.

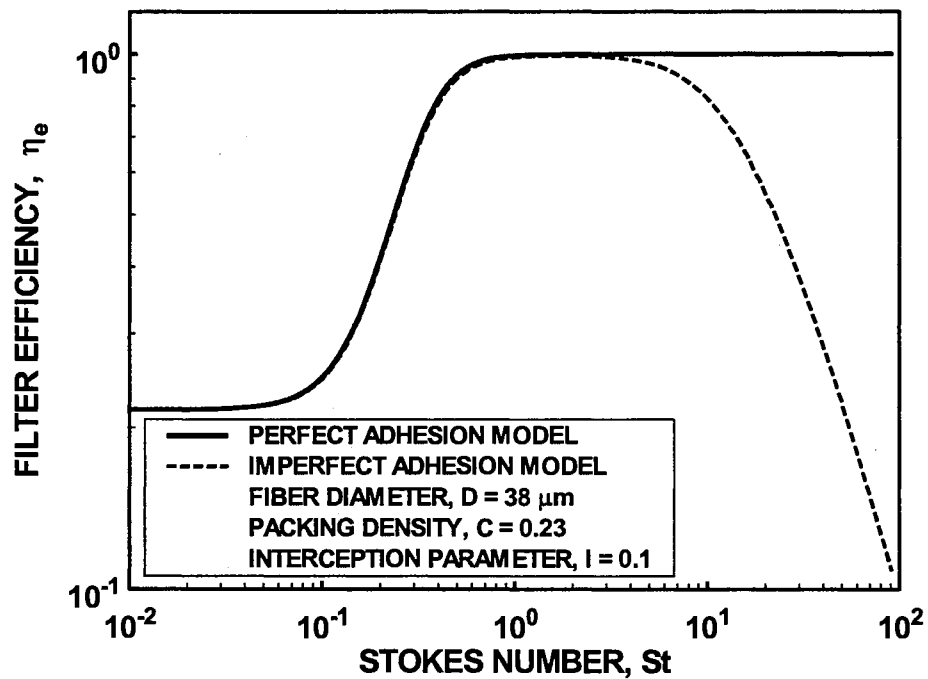


Figure 2.7 Stokes number dependence of filter efficiency estimated with model of interception and inertial impaction filtration for typical filter parameters

The elemental efficiencies of the small areas centered on the velocity measurement grid points may be combined to give an overall efficiency for the filter. For this calculation, a

uniform particle concentration per unit volume is assumed to hold across the entire cross section of the filter. The resulting equation for the overall efficiency, η_f , is:

$$\eta_f = 1 - \frac{\sum_{i=1}^n [P_e a_e u_\infty]_i}{\sum_{i=1}^n [a_e u_\infty]_i} \quad (2.45)$$

where P_e is the elemental penetration, $(1-\eta_e)$

a_e is the area of the element

u_∞ is the measured velocity upstream of the element

Note that a uniform particle concentration does not imply a uniform volumetric flow rate of particles.

2.5.7 Summary of filtration efficiency calculation approach and assumptions

In summary, the calculated estimates of filtration efficiency are based upon the following approaches and assumptions:

- a) fibrous filtration
- b) filtration by interception and inertial impaction,
- c) negligible filtration due to diffusion or gravitational settling,
- d) perfect or imperfect adhesion,
- e) the filter media has a uniform fiber radius, R_f , throughout the filter with the value a weighted mean of the distribution of fiber radii in the actual filter media,
- f) the packing density of the filter media, c , is uniform throughout the filter,
- g) the aerosol particles are monodisperse for each efficiency calculation,

- h) the aerosol particles all have the same density,
- i) the velocity distribution within the pleats is uniform,
- j) the calculated efficiencies represent the initial efficiencies of the clean filter with no added filtration by deposited particles, and
- k) the concentration of the aerosol particles per unit volume at the inlet to the filter is uniform for calculation of overall filter efficiency.

CHAPTER 3

EXPERIMENTAL APPROACH

The experimental approach in this research first was aimed to determine the improvements that simple changes in filter housing geometry can make in the flow distribution to a panel filter in order to estimate the resulting changes in filtration efficiency for a clean filter. The goal was to evaluate these changes while keeping the housing entrance flow and filter characteristics the same. The experiments were planned to limit the number of independent variables influencing the results by performing all measurements for a single model production engine panel air filter. Five different housings were built sharing a common fundamental geometry and experiments were performed at a single volumetric flow rate. The first stage results have shown that a small change in the housing configuration may change the flow distribution and filtration efficiency as well. The idea of designing an optimum model using an inverse theoretical technique to reduce the number of required experiments and the number of tested configurations came next. The theoretical calculations were performed and the resulting optimum model was built and tested experimentally to compare with the previous models. Pressure measurements were performed along and across the filter.

3.1 FLOW FIELD

A blower supplied the required airflow. The flow was seeded with $0.966 \mu\text{m}$ diameter polystyrene latex particles by a TSI model 9306 six jet atomizer, atomizing a 0.1% concentration solution of particles in water. These particles, which are available in the form of a 10% concentrated solution by volume, were diluted by using distilled water as follows: 10 ml of the particle solution (10% particle concentration) were added to 1000 ml of water. The housing was installed on the suction side of the blower as shown in Figure 3.1.

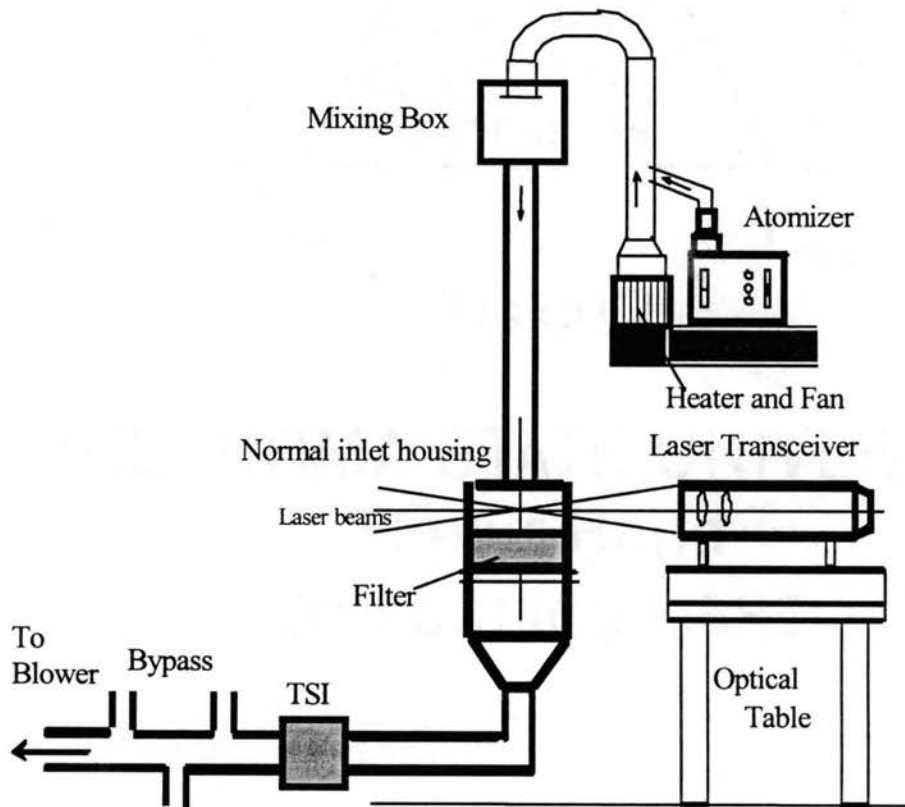


Figure 3.1: Flow field setup for Normal entry housing

The flow rate was controlled by a pneumatic flow control system. The inlet air was heated slightly by a heater to insure that the water droplets evaporated before reaching the filter housing. For the purpose of this research, it is estimated that less than 0.1 gram of seed particles was presented to a filter during a measurement run. This amount is expected to have a negligible effect on the filter resistance and the flow distribution. Compressed air at pressure of 276 KPa (40 psig) was supplied to the atomizer. The air actually used in the atomizer was at a pressure of 248 KPa (36 psig). The solution was atomized by passing it through the jet nozzles. Before the actual atomization process, it is possible to mix the solution with air and then atomize the mixture. This control in the atomizer also can be used to control the rate at which the particles were seeded into the system. The solution then passed through a mixer chamber before the 125-cm long duct, which provides a developed flow for the housings.

The seed particles were used only for velocity measurements and were not used to measure filter efficiency. Different flow rates were used in the pressure measurements part for the purpose of seeing the effect of filter resistance. Only two flow rates were used for the velocity measurements. 14 m³/hr (8.1 scfm via TSI flow meter), which makes Re (based on the hydraulic diameter of the entrance) equal to 2,000 (Laminar flow), and 212 m³/hr (125 scfm), which is the design condition of the automotive air filter.

The experiments were carried out in two stages. The first stage used five different housings. A common inlet flow duct and inlet velocity profile and a common exit duct were used. Velocity distribution measurements upstream of the filter were performed with a two component Laser Doppler Anemometer (LDA). Important features of the test configurations and experimental measurements will be discussed in the next section. The

second stage was performed after the results of the first stage had become clear and theoretical calculations were finished. The second stage consists of pressure and velocity measurements of the optimum model (the output of the theoretical calculations), providing a test of the theoretical calculations.

3.2 FILTER and FILTER HOUSINGS

3.2.1 Stage 1: Five different housing configurations

All experiments were conducted using a single standard production engine panel air filter constructed from resin-impregnated cellulose fiber. The specifications of the filter are listed in Table 3.1.

Table 3.1. Filter Specifications

DESCRIPTION	FILTER
	AI3192*
Length of filter, L (mm)	193
Width of filter, W (mm)	121
Height of filter pleat (mm)	30
Pitch of pleat (mm)	3.125
Design flow rate (m ³ /hr)	212
Design uniform velocity outside pleat (m/s)	2.53

*Model designation of manufacturer, Purolator Products, Inc.

The geometry of this filter was used as the primary parameter in the design of the filter housings used in the measurements. These housings, and the coordinate system used in the measurements, are illustrated in schematic form in Figure 3.2. The detail drawing showing the dimensions is presented in Figure 3.3. The entrance duct and all the housings had the same width as the filter. The entrance duct had cross-sectional dimensions of 121 mm by 50 mm. This duct was 1.25 m long (24 duct heights) to insure that the flow entering the filter housing had a fully developed velocity profile that was consistent for

all of the test cases. Velocity profile measurements confirmed that the flow was fully developed. The flow passing through the filter exited in a constant area duct with the same cross-sectional dimensions as the filter. Room air was drawn through the duct, housing and filter by a downstream-mounted centrifugal fan as explained in the previous section.

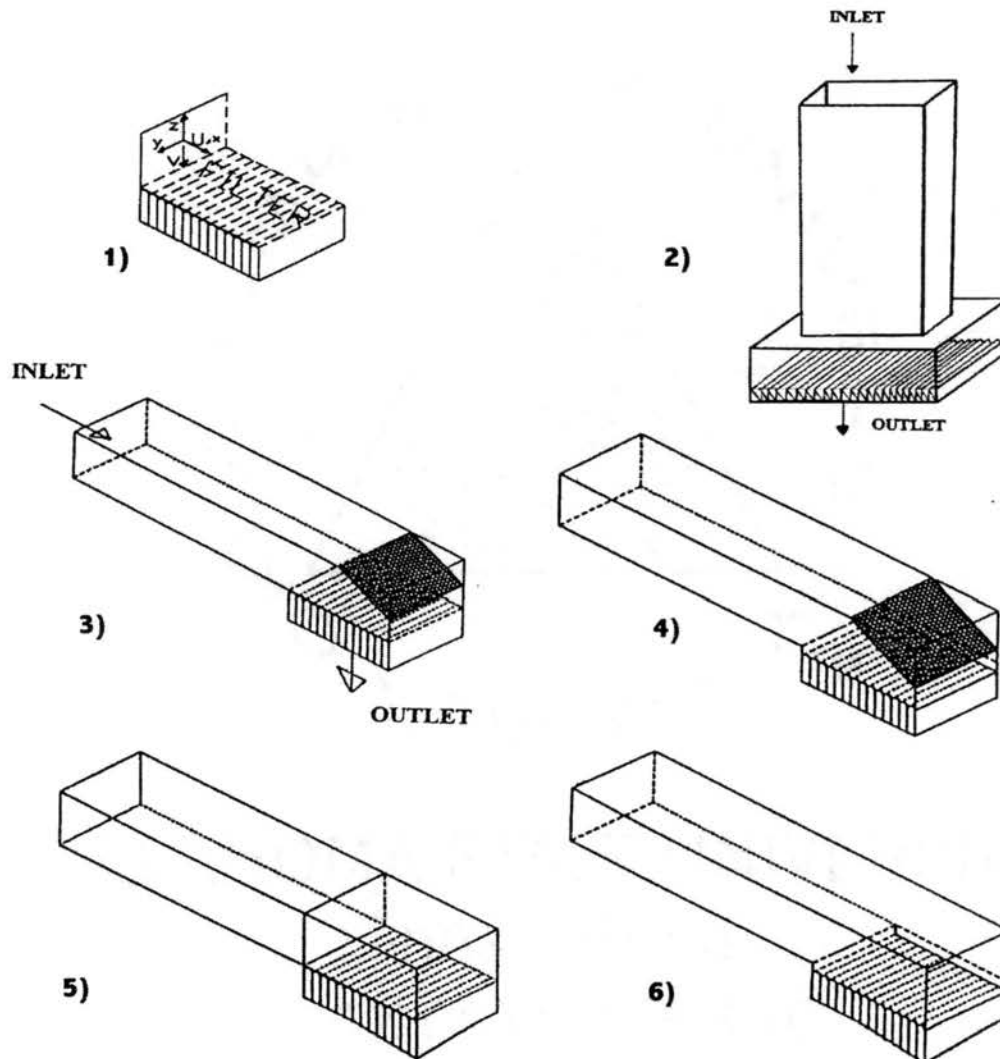


Figure 3.2: Coordinate system and filter housing configurations. 1) Coordinate system; 2) Normal inlet; 3) Tangential inlet with angle; 4) Tangential inlet with angle and step; 5) Tangential inlet; 6) Tangential inlet with step.

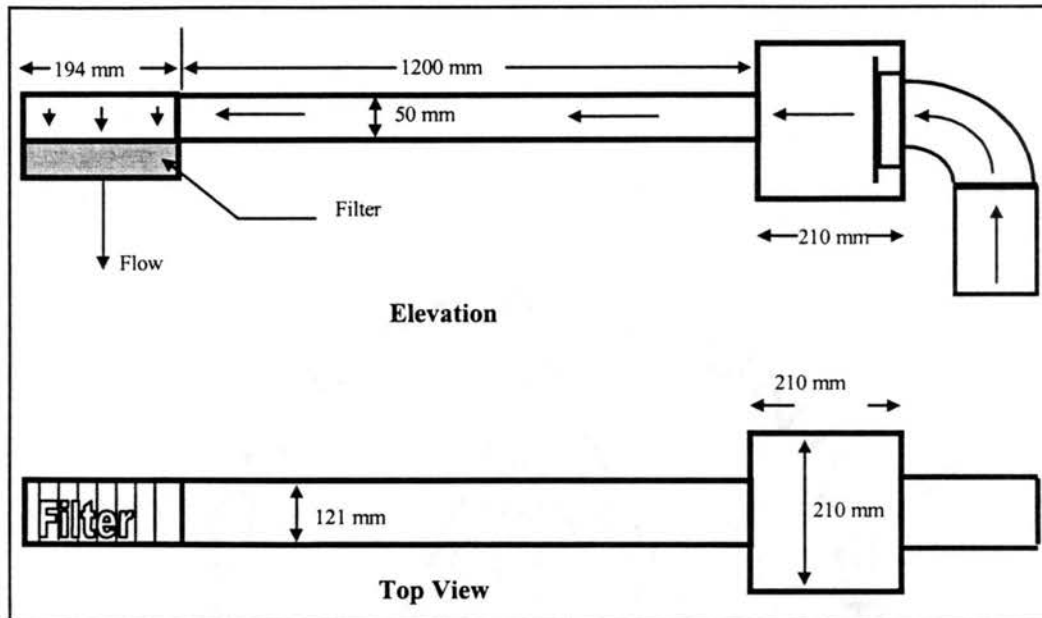


Figure 3.3: Tangential entry model; Mixing box, entrance duct, and housing

The study focused on the effects of the housing configuration on the flow distribution just upstream of the filter. One family of configurations employed an inlet flow entering the housing directed parallel to the inlet plane of the filter. These housings will be termed “tangential inlet housings.” This family includes housings with and without a 10 mm step down from the inlet duct to the inlet face of the filter (see figure 3.2), and with and without a 20 degree angled wall opposite the filter. The 20-degree wall began at a distance of 83 mm from the entrance to the housing. For comparison, experiments also were performed with one housing with the inlet duct directed normal to the inlet plane of the filter, ending 50 mm from the filter surface, centered on the upper plane of the housing. All housings were constructed of transparent acrylic and glass to provide optical access for LDA measurements of the velocity fields. All tests were performed at the design volumetric flow rate of the filter, $212 \text{ m}^3/\text{hr}$ ($125 \text{ ft}^3/\text{min}$), as measured with a TSI Model 2010 Mass Flowmeter mounted downstream of the test housing, ahead of the exhauster. The optimum housing was tested on a wide range of flow rate including the design volumetric flow rate of the filter ($212 \text{ m}^3/\text{hr}$).

3.2.2 Stage 2: Housing configuration of the optimized model

Stage 2 was a test for the optimized shape from the theoretical approach. The details of the dimension of the output shape are illustrated in Figure 3.4.

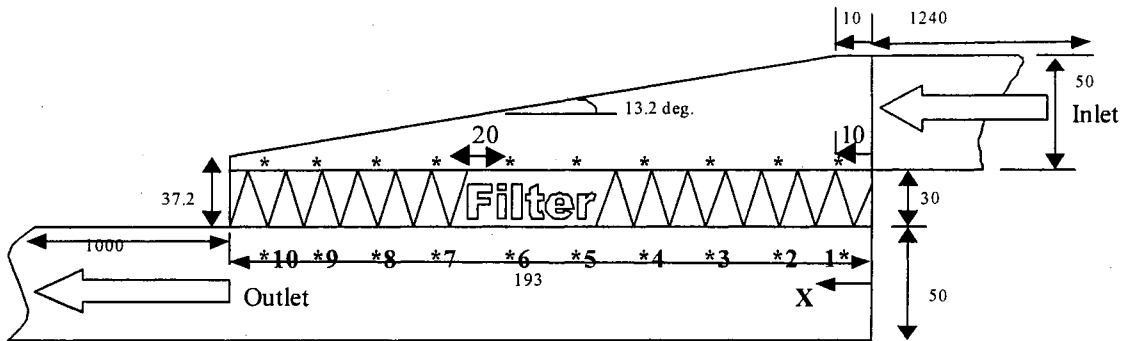


Figure 3.4: Detail dimensions of the optimized model (dimensions in mm)

This housing has ten static pressure taps 6 mm above the filter. Pressure taps on the side wall of the housing. Also this housing has ten taps 6 mm below the filter (on side wall of the housing) at the same X-position in order to measure the pressure difference across the filter. The first pressure tap starts at 10 mm from the inlet and the second one 10 mm from the first one. The rest have 20-mm spacing in-between. The last hole is 9.3 mm from the end of the filter. Detail drawing is shown in Figure 3.5.

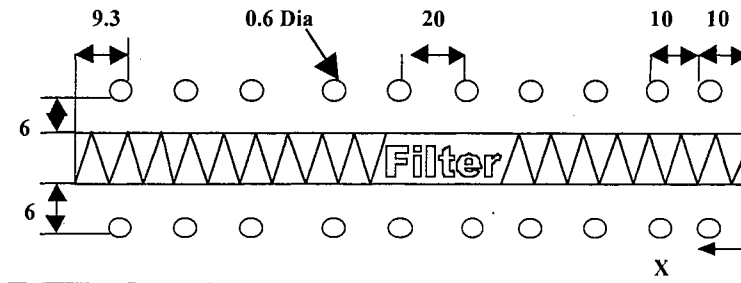


Figure 3.5: Pressure tap spacing details in the side wall (dimensions are in mm)

The details of the pressure taps on the housing are illustrated in Figure 3.6.

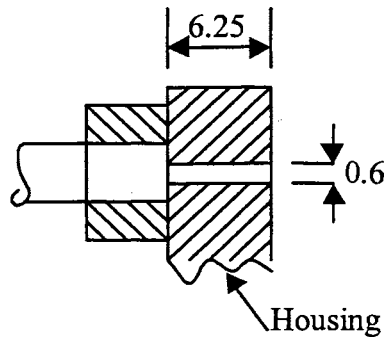


Figure 3.6: Pressure hole details in side wall of the housing (dimensions are in mm)

3.2.3 Coordinate system and experimental grid points

Fine grids for velocity measurements were established as shown in Figure 3.7. The measurements were performed over one half the filter width, assuming symmetry over the second half. Eight lines in the y-direction times 25 points in x-direction on each line with a total of 225 measurements points were taken over half of the filter. Measurements start at 19 mm (0.75 in) from the inlet and a 6.35 mm (0.25 in) as a measurement grid increment along each line.

All measurements were performed in the plane approximately 13 mm (0.5 in) above the filter pleat peaks. For one of the stepped housing cases, measurements also were performed in the plane 22 mm above the filter, the same plane relative to the entrance duct used for the non-stepped housing, (10 mm step plus 13 mm above the lower edge of the entrance duct). This was done to have a measurement at the same plane as if there is no step.

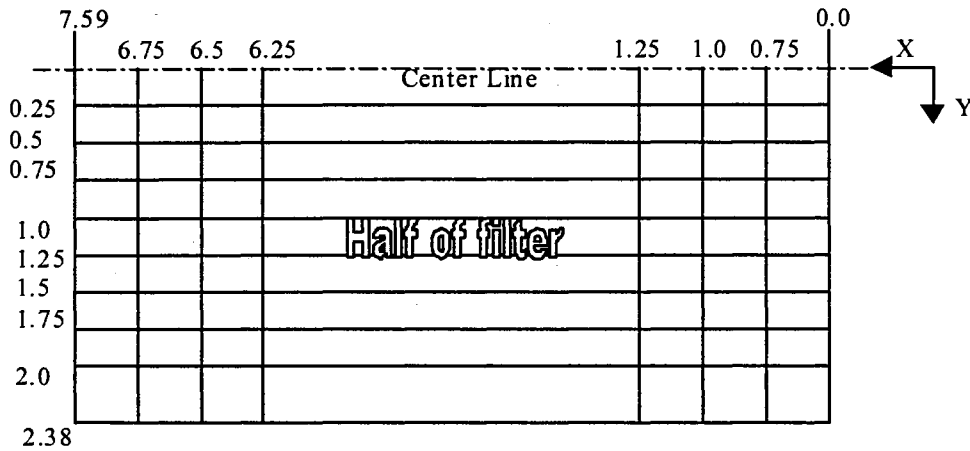


Figure 3.7: Grid points and Coordinate system
(Dimensions are in inches; not all of the vertical lines are shown in this figure)

For the final model (output of the theoretical calculations), measurements were taken 8 mm (0.3 in) above filter to enable LDA measurements at the lowest height above the filter. This height was dictated by the necessity for the lowest of the crossed laser beams to clear the edge of the filter and housing wall on its way from the transceiver to the focal point.

3.3 LDA SETUP FOR VELOCITY MEASUREMENTS

Velocity measurements upstream of the filter were performed with an Aerometrics, Inc. two-component, fiber-optic Laser Doppler Anemometer (LDA) system utilizing a 4 watt argon ion laser. The system's probe volume is $737 \mu\text{m}$ long and $66 \mu\text{m}$ in diameter. As illustrated in Figure 3.8, the beam from the laser is guided via two steering mirrors into the fiber drives. A Bragg cell provided frequency shifting to enable determination of flow direction in reversed flow regions. A dispersion prism in the fiber drive splits the single laser beam (blue) into two beams (blue and green). These two beams are further split by a

Bragg cell into two beams having the same color and 40 MHz frequency shift (called shifted and unshifted beams or 1st and zero order beams). The four beams are directed into the optical couplers by means of mirrors. In the couplers, the beams are focused into the fiber optical cables of 4 μm diameter with the help of focusing lenses housed in the couplers. The beams travel through the fiber optic cables to the transceiver head. The transceiver head is so named since it serves both as a transmitter of the four beams and also as a receiver of the scattered signals generated by the particles.

The LDA system operated in the fringe mode. When the two beams having the same color meet at the measurement point, they cause an optical interference causing the generation of alternate bright and dark fringes. When a particle crosses the probe volume, it scatters the light in the form of bright and dark intensities. These intensities are superimposed on a low frequency high amplitude pedestal modulating it. This pedestal represents the Gaussian light intensity in the probe volume.

The fiber-optic transceiver operates in the back-scatter mode, collecting light reflected from seed particles passing through the probe volume and transmitting it through a fiber-optic cable to two photomultipliers. The reflected light signals, the Doppler bursts, are processed in the frequency domain using Fast Fourier Transforms to find the Doppler frequencies and the two components of the flow velocity.

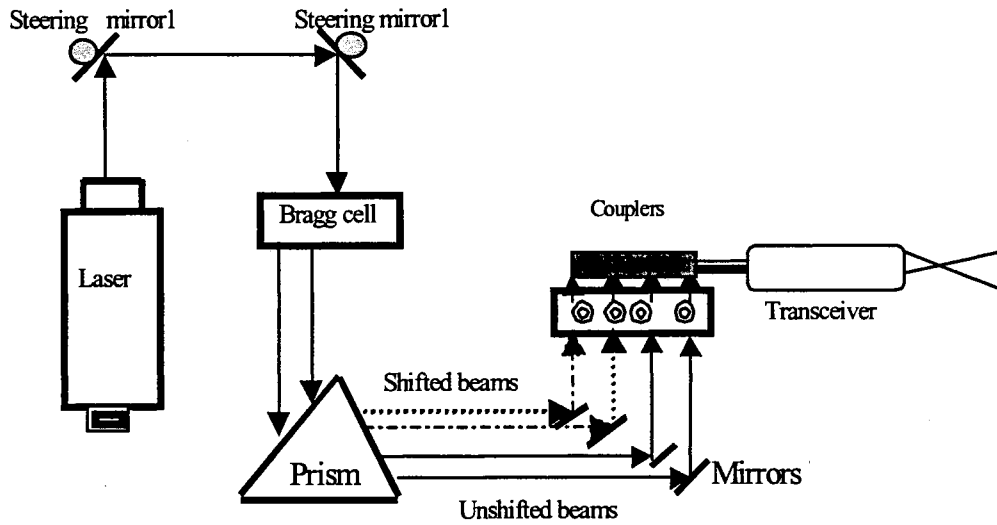


Figure 3.8: Fiber Drive Schematic Diagram

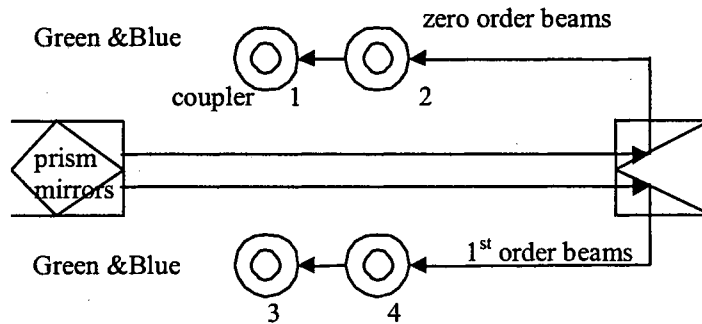


Figure 3.9 Schematic diagram of coupler arrangement

3.3.1 Data and LDA signal processing parameters

The non-uniform filter housing flows, with varying velocities, flow directions and seed particle concentrations, required the LDA signal processing parameters to be adjusted as measurements were performed at different points in the flow field. Data rates and validation rates varied across the flow field. All measurements reported here result from 500 validated samples. The sampling time was from 15 seconds to 60 seconds. Previous

tests with this system have shown that measurements with 500 or more validated samples result in mean velocity uncertainties of less than 2% (Newman (1994), Duran (1995)). The velocity measurement uncertainties for the present experiments were evaluated with similar results. As described in detail in section 5.3, the uncertainty of the mean velocity was less than 1.9 %. This uncertainty includes measurement accuracy and repeatability. No corrections were applied for the various biases that may enter into the LDA measurements in the varied flow regions.

3.3.2 Set up for pressure measurements

Pressure measurements were performed using a Validyne Model DP215 differential pressure transducer. The pressure transducer has a range of 140 mm of H₂O and a maximum output voltage of 10 volts. The pressure transducer was connected to a Scanivalve (Scanivalve type S5-24), which is connected to different taps along the housing (10 ports in the inlet part of the housing and 10 ports in the exit part of the housing). The Scanivalve was connected to a stepper motor, which is controlled by a controller switch. The output signal of the pressure transducer was passed to a demodulator then to a computer through a 12 bit, high-speed data acquisition board. The schematic drawing of the setup is illustrated in Figure 3.10

The pressure distribution measurements have been done in two stages:

First stage: Measurement of the pressure distribution along the inlet part of the housing.

In this stage the pressure transducer negative side was connected to port 1 at the inlet plenum of the housing and the Scanivalve was connected to the positive side of the pressure transducer.

Second stage: Measurements of the pressure distribution along the exit plenum of the housing.

In this case the positive side of the pressure transducer was connected to port 1 of the inlet plenum of the housing and the negative side to the Scanivalve.

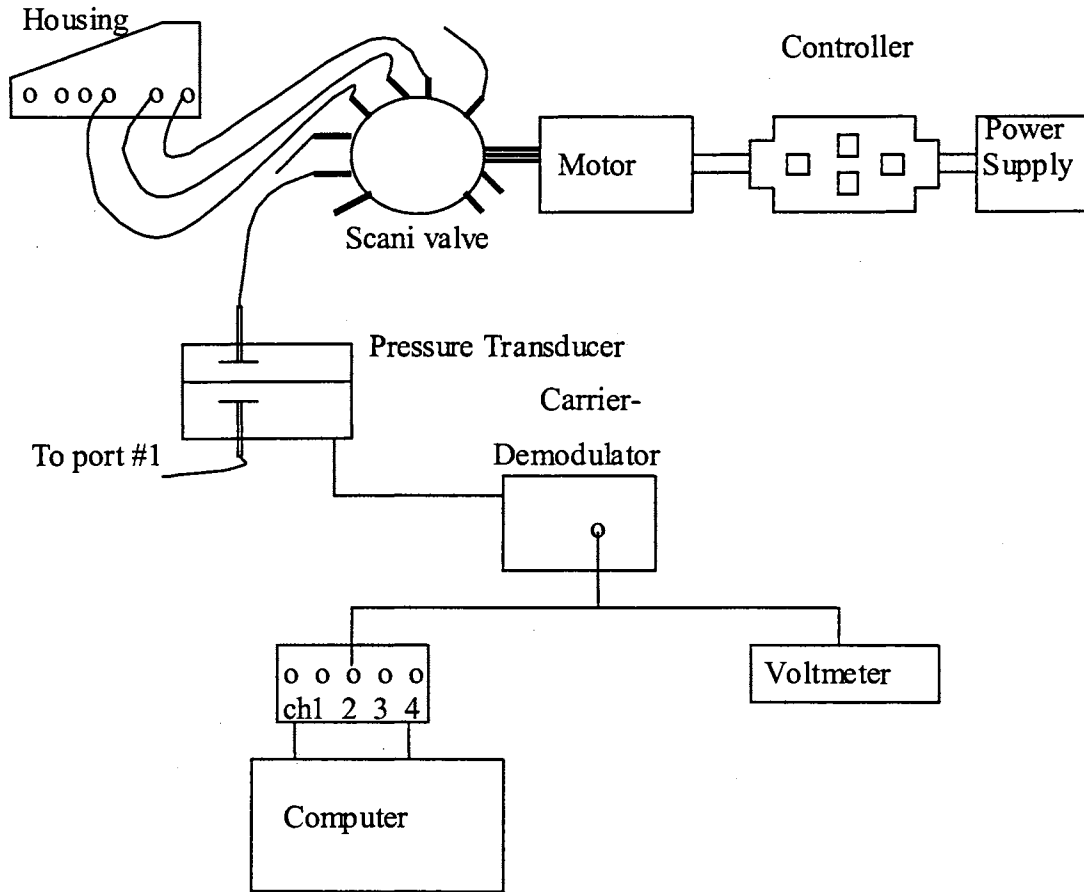


Figure 3.10: Schematic of pressure transducer setup

3.3.3 Procedure for taking pressure measurement data

First: calibration of the pressure transducer.

A calibration of the differential pressure transducer was performed before taking any data. The calibration was done against the inclined manometer on range of 76 mm of

H₂O. The upstream air temperature was measured with a thermocouple and a digital temperature read-out. The barometer reading was taken to determine local atmospheric pressure after applying appropriate temperature and gravitational corrections. The air temperature and atmospheric pressure were used to calculate the air properties.

Second, switching the Scanivalve to the desired port number and taking the data points. 1000 samples were taken at 200 samples per second, which makes the sampling time 5 seconds. Measurements indicated that this was an adequate record length.

CHAPTER 4

RESULTS AND DISCUSSION

The present research has been performed in several stages. In this chapter the results will be discussed in three stages. The experiments limited the number of independent variables by performing all measurements for a single model production engine panel air filter (Purolator A13192). All velocity measurements have been performed at a single volumetric flow rate ($212 \text{ m}^3/\text{hr}$) in filter housings sharing a common fundamental geometry, a common inlet flow duct and inlet velocity profile. The first stage focused on taking LDA measurements using different housing configurations. In this chapter the housing configurations will be given an index code, this code will be used to describe the housing configuration throughout the chapter. The housing configurations, which are going to be discussed in the first stage, are:

1. Tangential inlet housing. In this configuration the inlet flow entering the housing is directed parallel to the inlet panel of the filter as illustrated in Figure 4.1.

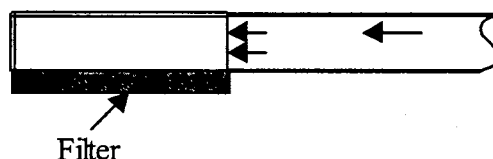


Figure 4.1: Tangential inlet housing (Code TIH)

2. Tangential inlet with step. The housing is similar to the first one but in addition, it has a 10 mm step down from the inlet duct to the inlet face of the filter as illustrated in Figure 4.2 below.

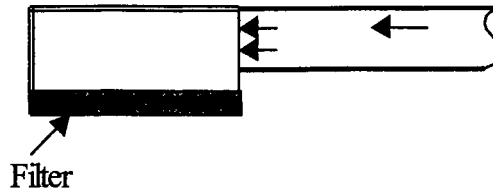


Figure 4.2: Tangential inlet housing with step (Code TISH)

3. Tangential inlet with angle. This geometry has the same inlet as number 1 but in addition it has a 20 degree angled wall opposite the filter. The 20 degree angled wall began at a distance of 83 mm from the entrance to the housing as in Figure 4.3.

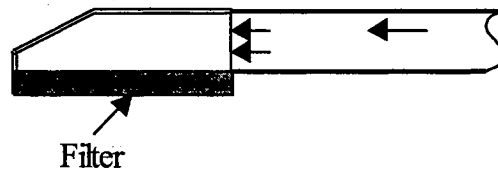


Figure 4.3: Tangential inlet housing with angled wall (Code TIAH)

4. Tangential inlet with angle and step. This model is similar to the previous one (number 3) but in addition to that it has a 10 mm step at the entrance of the housing as shown in Figure 4.4.

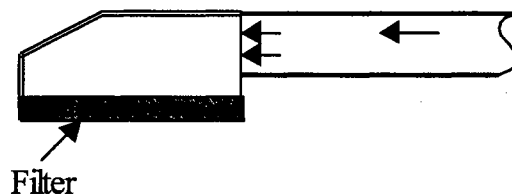


Figure 4.4: Tangential inlet housing with step and angled wall (Code TLASH)

5. Vertical model housing. This housing has the same basic dimensions but the inlet duct is directed normal to the inlet plane of the filter as illustrated in Figure 4.5.

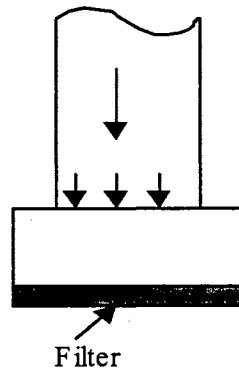


Figure 4.5: Normal inlet housing (Code NIH)

The second stage focused on the development and application of an optimization technique to find better housing configurations. Following the computations, an experimental verification was performed. The optimized housing geometry is shown in Figure 4.6. Pressure measurement along the filter was done in this stage. The pressure difference across the filter also will be discussed for both cases filter alone and filter and sheet of the same filtration material on top of it as illustrated in Figure 4.7

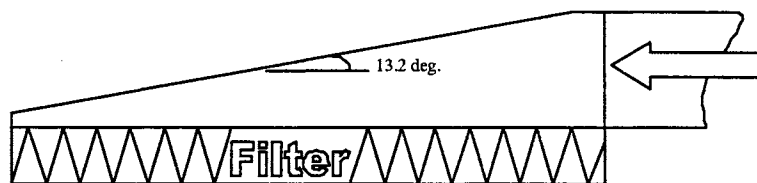


Figure 4.6: Optimized housing geometry (Code OTIH)



Figure 4.7: (1) Filter only and (2) filter with an additional sheet arrangement

The third stage was focused on the filtration efficiencies of the different housing configurations discussed in the first and second stages. The experimental velocity results were substituted into a filtration model, and this filtration model produces efficiencies that will be discussed in this section.

The present work results will be discussed in the following nine sections. The mean velocity distributions will be presented first and then the root mean square velocity fluctuations. The effect of filter resistance will be discussed next. The optimized program results and the pressure distributions above, across and below the filter will be presented next. The filtration efficiencies will be discussed last. Representative figures will be presented and the rest of the results will be found in the appendices. Appendix A has the results of the axial velocity distributions in different housing configurations, and Appendix B has the RMS velocity fluctuation distributions. Appendix C has the laminar flow results of the optimized model, and the optimization program results. Appendix D has the pressure distribution results. Appendix E has the mean velocity distributions at the centerline of the filter on different heights. Appendix G has the flow chart of the optimization routine. All results were taken in terms of flow rate, which can be transferred into Reynolds number in Table 4.1 below. Reynolds number is defined based on the hydraulic diameter of the entrance rectangular duct as:

$$Re = \frac{UD_h}{\nu}$$

where: U is the duct average velocity

D_h is the duct hydraulic diameter = 7.076 cm

ν is the kinematic viscosity

Table 4.1 Reynolds numbers- Flow rate conversions

Flow Rate (m ³ /hr)	Reynolds Number
14	2,000
34	4,900
65	9,500
85	12,000
103	15,000
120	17,500
137	20,000
153	22,000
212	31,000

4.1 MEAN VELOCITY DISTRIBUTIONS

The velocity measurement results are presented first in terms of the mean velocity distributions for individual cases, and then as comparisons of the mean velocity distributions along the axial centerline of the filter. The coordinates in the plots are scaled with the axial length of the filter and housing, L , and one half the width of the filter and housing, $W/2$. Thus the back plane of each plot, $Y = 0$, represents the axial centerline of

the filter. Recall all measurement data (225 points) were taken on one half of the filter assuming a symmetric behavior for the other half of the filter.

4.1.1 Axial velocities

The axial mean velocity distribution in the plane 13 mm above the filter for tangential inlet housing, code TIH, is shown in Figure 4.8. Figure 4.9 shows the axial velocity distribution results in the normal inlet-housing model. This figure shows negative and positive velocities at both ends of the housing which reveals very large circulation zones at both ends with opposite circulation direction. The normal axis in this figure is different from the others since the flow in this model is quite different. The position X/L equal to 0.5 is the center of the inlet duct. The negative and positive axial velocities mean that the flow is going in two different directions in the regions close to the side walls of the housing (negative means flow going to the right and positive means flow going to the left). At the central region of the filter ($X/L=0.5$) all the flow is going into the filter (normal velocity is very high) so the axial velocity parallel to the surface of the filter is very small (impinging jet-like flow). At the right region of the filter (from $X/L= 0.2 -0.5$) the flow is going to the right (negative sign). At the left region of the filter (From $X/L=0.5 - 0.8$) the flow is going to the left (positive sign)

The rest of the axial mean velocity distributions for different housing configurations are shown in appendix A. The addition of the angled upper wall and the step did not produce dramatic changes in these profiles for any of the tangential entry housings. They all exhibited the same general trend of a streamwise decrease in axial velocity as the endwall is approached.

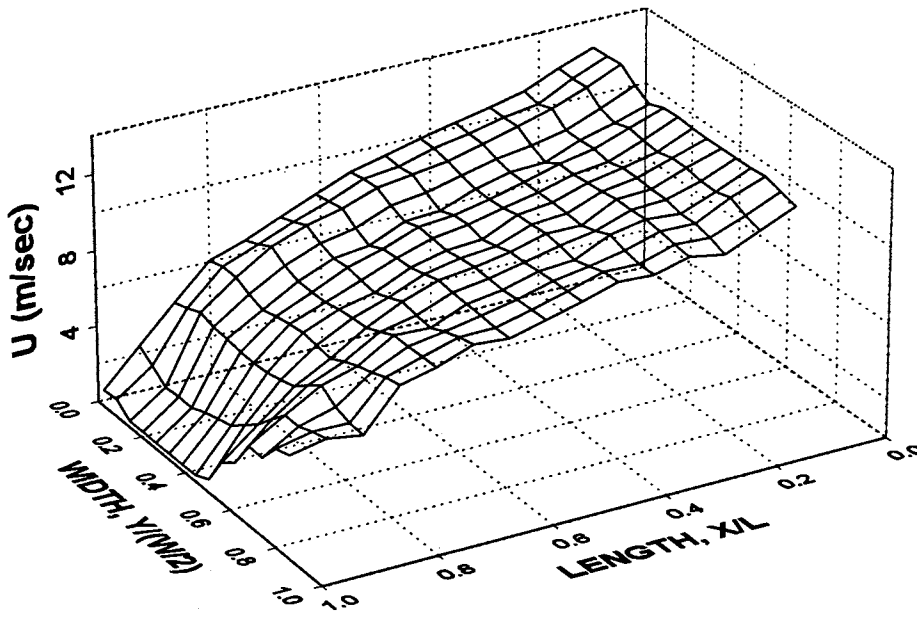


Figure 4.8: Axial velocity distributions in TIH model 13 mm above filter

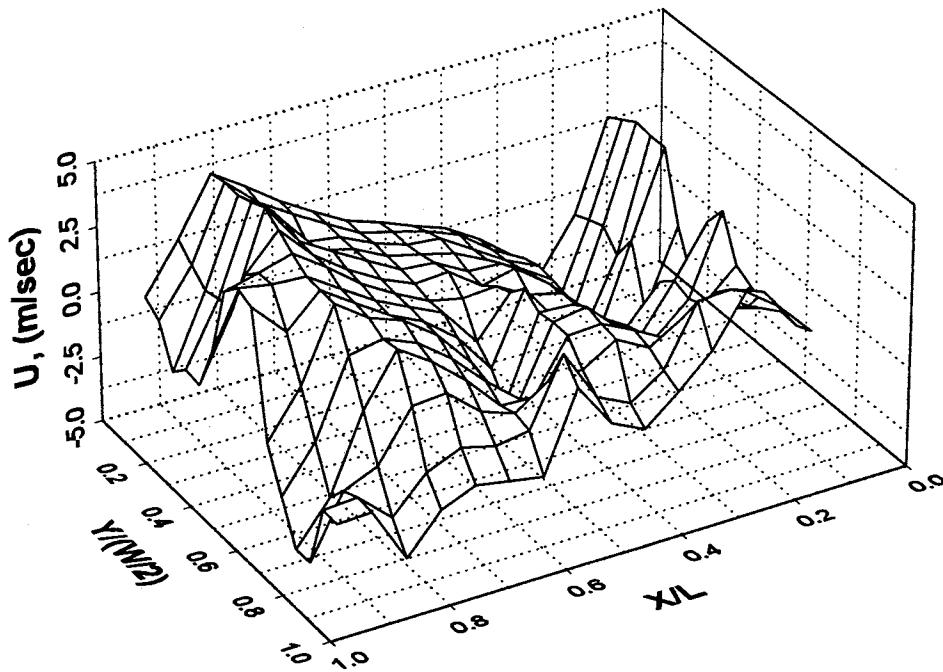


Figure 4.9: Axial velocity distributions in NIH model 13 mm above filter

4.1.2 Normal velocities

The normal mean velocity distributions are the most important for analyzing the effects of the different housings on the filter performance. The normal velocity is the component directed through the filter carrying the dust through the filter. The normal mean velocity distributions in the plane 13 mm above the filter for model TIH are shown in Figure 4.10. Figure 4.11 shows the results of the optimized model, OTIH, at 8 mm above filter. The OTIH model measurements were performed at 8 mm rather than the rest, which were at 13 mm to enable LDA measurements at the lowest possible height above the filter. Because of the shape of the upper wall of the optimized model, the measurements could not be performed in the plane 13 mm above filter. When the measurements were performed at 13 mm above the filter, the laser beam went out of the housing at about $2/3$ of the axial length of the filter. The author believes the comparison could be done between these two different planes and the difference is insignificant. (as shown in Appendix E, see figures E.1 and E.2). Figure 4.12 shows that the normal entry housing produces an impinging jet-like flow, with very high velocities in line with the inlet flow at the center of the filter and low velocity, recirculating flow at the sides. Figure 4.13 shows the results of the model TISH at 22 mm above filter. Figure 4.14 shows the results of the same model but at 13 mm above filter. Figures 4.15 and 4.16 show the results of model TIAH and TIASH respectively.

It may be observed in Figure 4.10 that for the tangential inlet housing, the normal velocity directed toward the filter is low at the entrance to the housing, increases at the center, and decreases to negative values at the end. The negative values, velocities away from the filter, indicate endwall separation and recirculation. From Figures 4.14 and 4.15,

one may see that the addition of a step increases the initial velocity toward the filter, but the velocity decreases continually approaching the end wall.

Figure 4.16 shows that the addition of the angled wall to the tangential entrance housing produces more uniform flow toward the filter with substantially increased positive velocities near the endwall. Figure 4.11 shows that the optimized model designed with the optimization program, produces the most uniform flow among all of them. It increases the normal velocity toward the filter near the end wall of the housing, providing an evidence of a suppression of separation and recirculation near the endwall. Further evidence will be seen later in the RMS velocity fluctuation figures. Figure 4.17 shows the result for the same model as in 4.11 (model OTIH) but in addition to the filter there was a sheet of filter paper on the surface of the filter itself. The velocity distribution seems to be a little more uniform than in the case of the filter only.

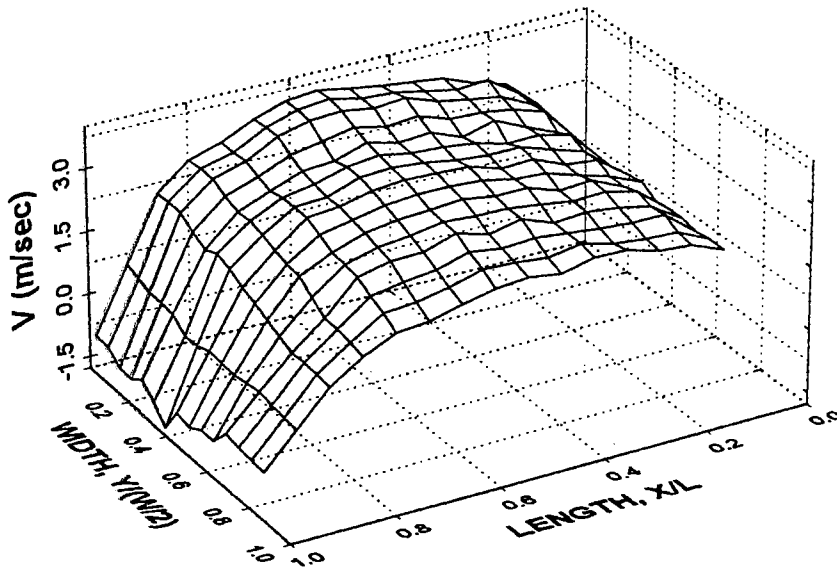


Figure 4.10: Figure Normal velocity distributions in TIH model 13 mm above filter

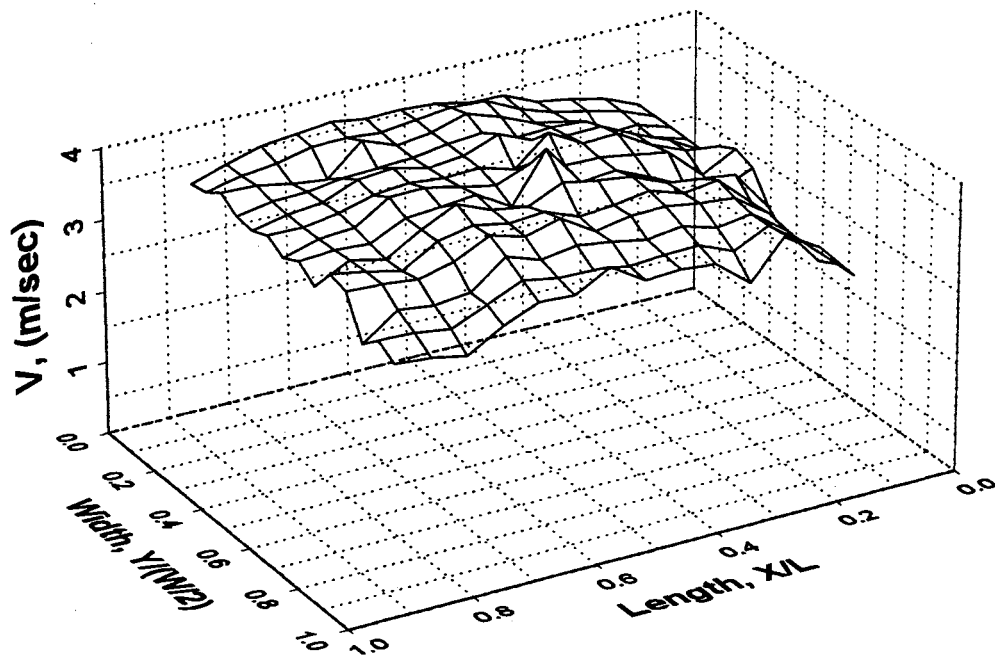


Figure 4.11: Normal velocity distributions in OTIH model 8 mm above filter (Filter only)

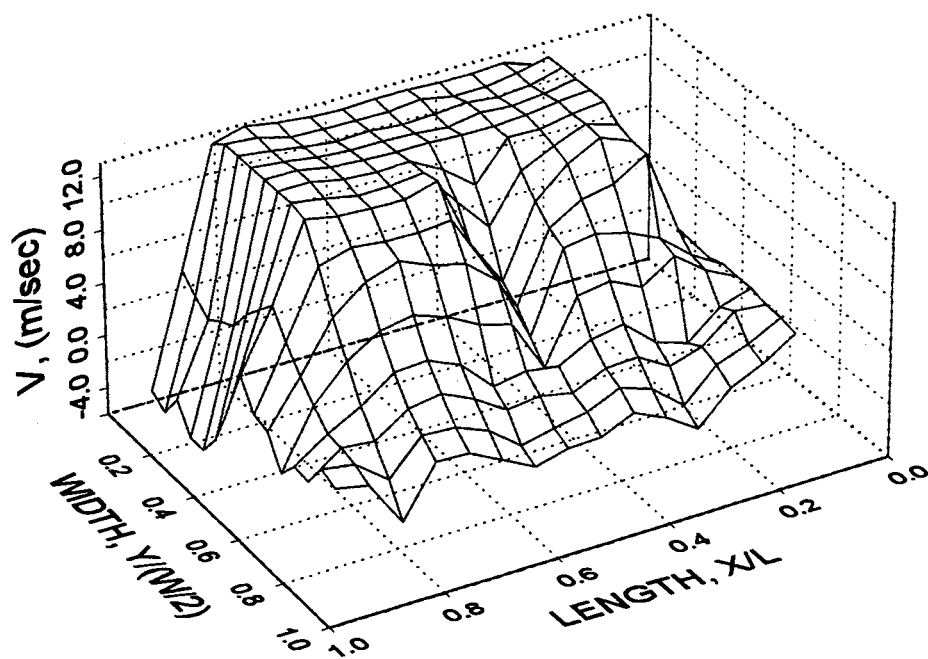


Figure 4.12: Normal velocity distributions in NIH model 13 mm above filter

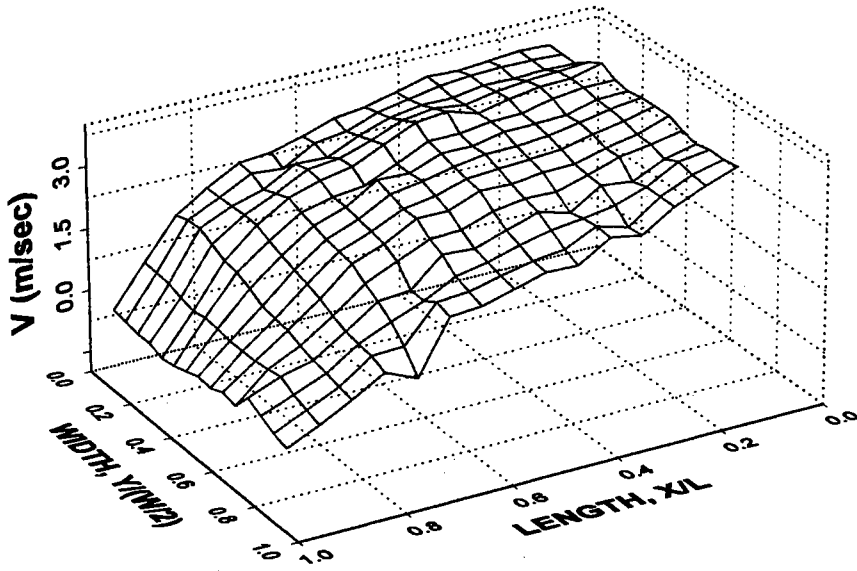


Figure 4.13: Normal velocity distribution in TISH model, 22 mm above filter

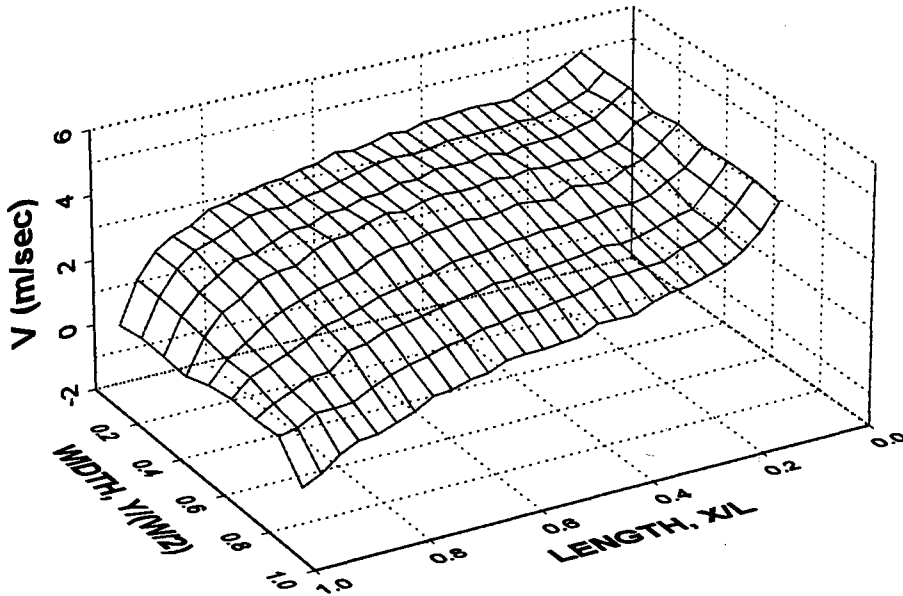


Figure 4.14: Normal velocity distribution in TISH model with step, 13 mm above filter

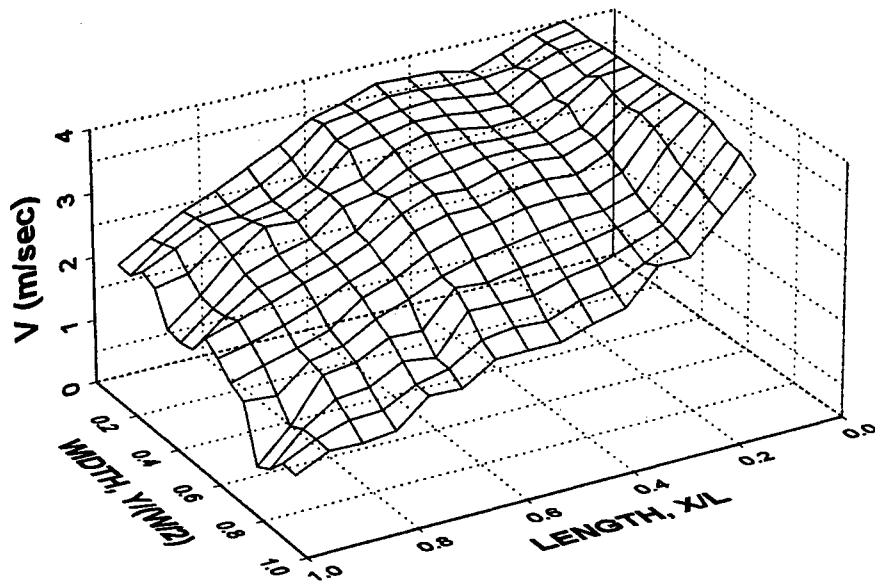


Figure 4.15: Normal velocity distribution in TIASH model 13 mm above filter

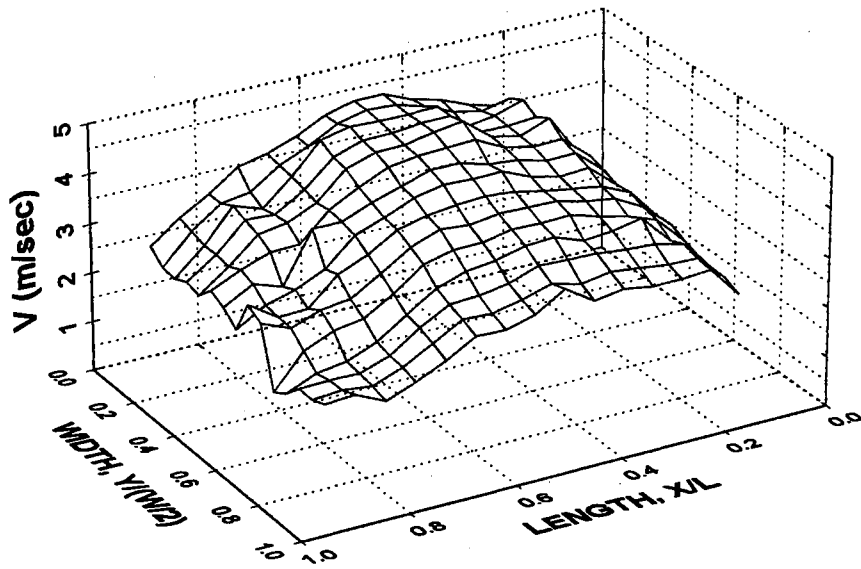


Figure 4.16: Normal velocity distributions in TIAH model 13 mm above filter

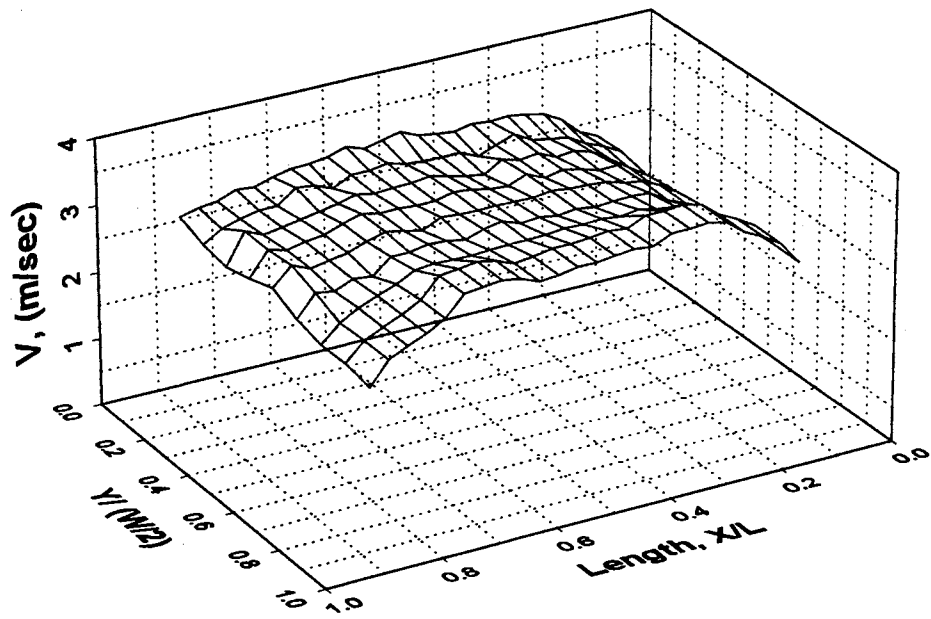


Figure 4.17: Normal velocity distribution in OTIH model, 8 mm filter (filter with an additional sheet)

4.2 RMS VELOCITY FLUCTUATION DISTRIBUTIONS

The measurements of the rms fluctuations of velocity provide further evidence to support the interpretations of the differing normal velocity distributions presented in the previous section. Figure 4.18 shows normal velocity fluctuations in TIH model. Figure 4.19 shows the normal velocity fluctuation in OTIH model. The rest of the rms velocity results for the housing configurations are shown in appendix B.

Figure 4.18 revealed very large normal velocity fluctuations at the endwall of the tangential inlet housing, (TIH) model. Figure 4.19 shows the least amount of fluctuations in the normal velocity among all the other housings, which supports the argument of having the least recirculation zone near the endwall. Again like the normal velocity, the fluctuations in the case of the filter with an additional sheet are smoother than without the sheet which might be interpreted as the result of the measurement being close to the plane surface of the filter.

Measurements of the rms velocity fluctuation distributions showed that they were reduced by the addition of the angled wall and optimizing the shape by using the output of the optimization program, providing evidence of a suppression of separation and recirculation near the endwall.

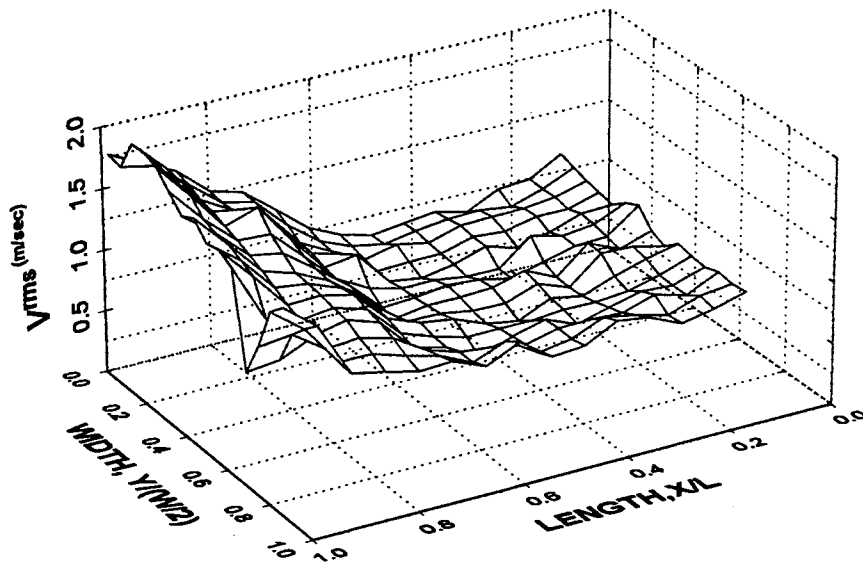


Figure 4.18: Normal velocity fluctuations in TIH model, 13 mm above filter

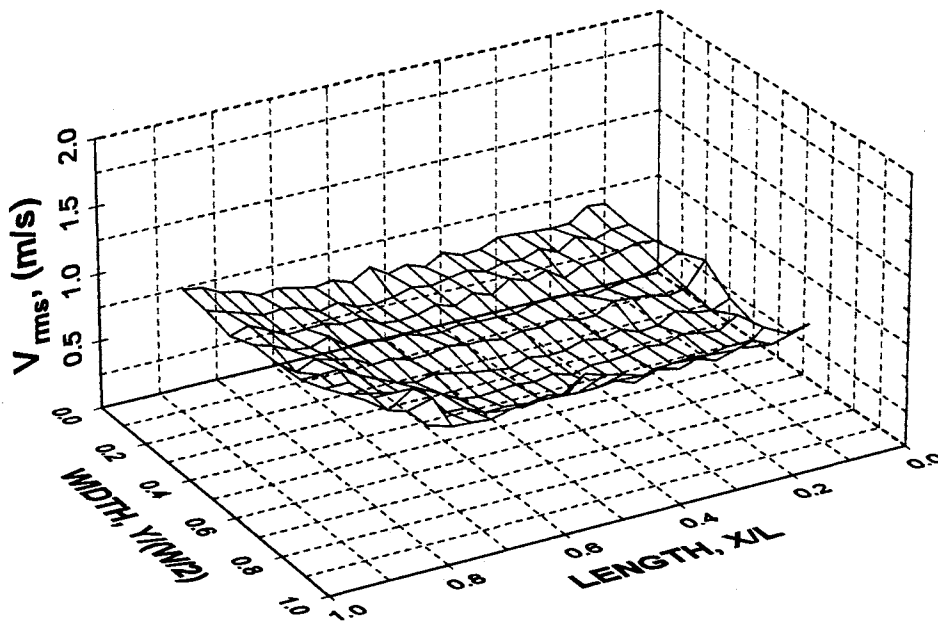


Figure 4.19: Normal velocity fluctuations in OTIH model, 8 mm above filter (filter with an additional sheet)

4.3 EFFECT OF FILTER RESISTANCE ON VELOCITY DISTRIBUTION

The effect of the filter resistance on the flow field may be seen in Figures 4.20 and 4.21. The measurements were obtained at the same plane as if the filter was mounted in the model TIAH, 13 mm above the filter location. It may be observed that the normal velocities reach peak magnitudes much closer to the endwall without the filter present to provide resistance to the flow. The filter provides sufficient resistance to the flow to alter the velocity distribution substantially, but insufficient resistance to make the flow uniform. The axial velocity distribution of the case without filter (Figure 4.20) exhibits the same trend as with the filter mounted. Figure 4.16 shows the normal velocity distribution in the same housing (TIAH) but with the filter mounted. Comparing Figure 4.21 with Figure 4.16 shows clearly that the filter resistance makes the normal velocity distributions more uniform. Figure 4.16 with filter mounted shows higher normal velocity distribution at the first and end regions on the surface of the filter. At the central area of the filter (X/L about 0.5) both cases (without and with filter) have about the same normal velocity. The effect of filter resistance can be seen more clearly in Figure 4.21 than in Figures 4.11 and 4.17 (filter only–filter with an additional sheet cases). The filter with an additional sheet exhibits normal mean velocity and velocity fluctuations that are a little bit more uniform than the case of the filter alone. The axial velocity distribution for all cases (without filter, filter only and filter with an additional sheet) had the same trend (maximum velocity at the inlet and then the velocity decreases with the axial coordinate toward the end wall). The filter resistance effect appears clearly on the normal velocity distribution in the case of no filter. The normal velocity distribution in the case of no

filter is not uniform. It starts very low at the beginning of the filter position and then reaches the maximum at about half the length of the filter and then decreases toward the end of the filter. The effect of the filter resistance in terms of pressure drop will be discussed later. The more resistance we have the more uniformity of the normal velocity we get. The least uniformity is the one without resistance; the no-filter case. The best uniformity is the one with maximum resistance; filter with an additional sheet case.

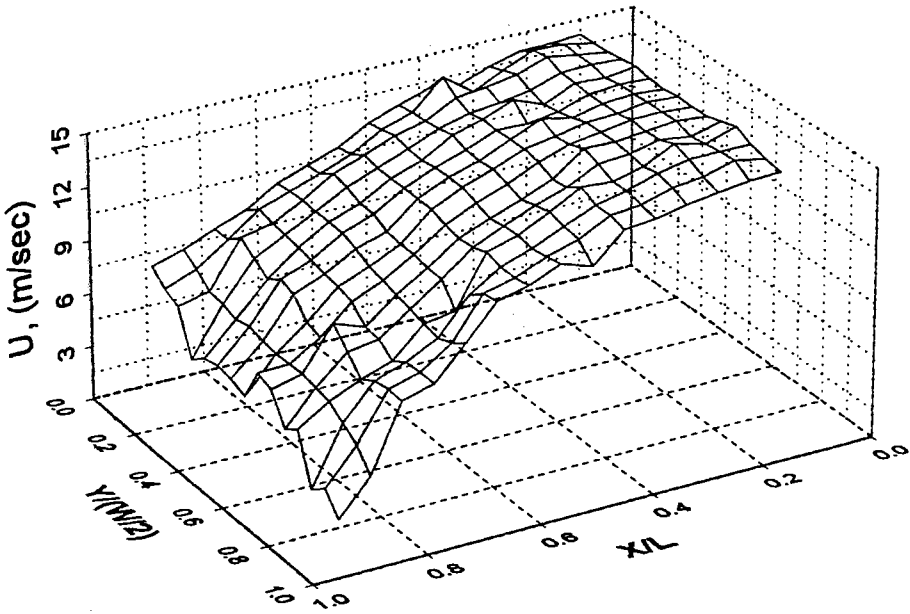


Figure 4.20: Axial velocity distribution in model TIAH without filter (at the same plane of measurements as if there is a filter, 13 mm above filter surface location)

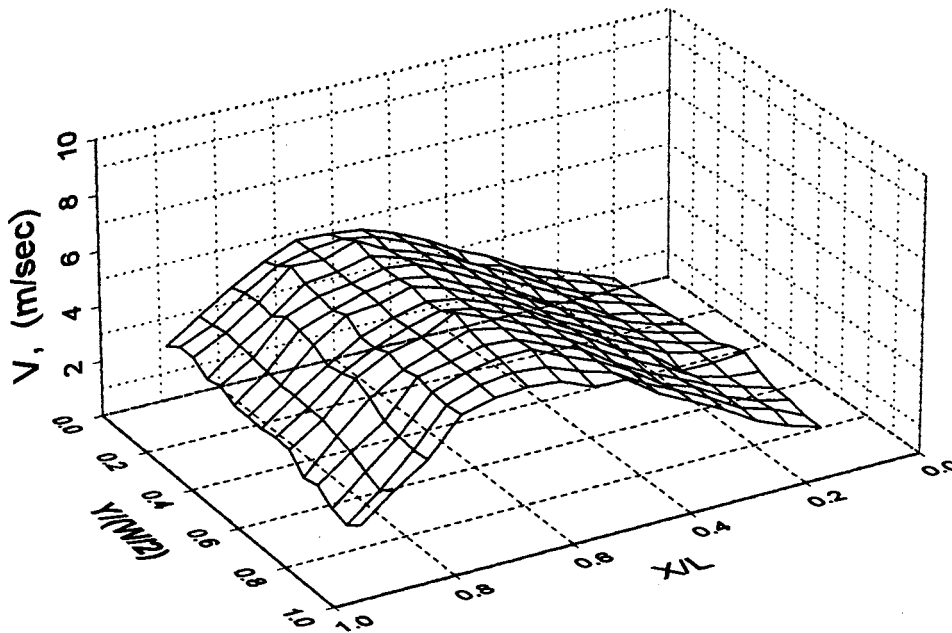


Figure 4.21: Normal velocity distribution in model TIAH without filter (at the same plane of measurements as if there is a filter, 13 mm above filter surface location)

4.4 COMPARISONS OF MEAN VELOCITY DISTRIBUTIONS ALONG HOUSING AXIAL CENTERLINE

The mean axial and normal velocity distributions along the axial centerline of the housing are compared for the different housing geometries in Figures 4.22 and 4.23. It may be observed in Figure 4.22 that the axial mean velocity along the centerline decreases for all cases, with the four tangential inlet cases having the lowest velocities near the endwall. As noted earlier, the angled wall has a relatively small effect on the axial velocity distribution. Also adding resistance to the filter with a sheet on the top of the filter does not have any significant effect on the axial velocity profile.

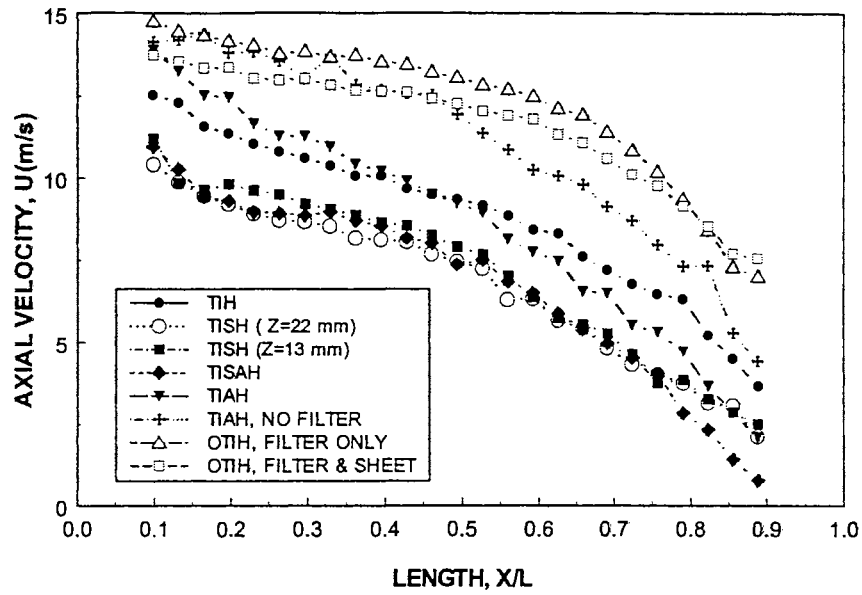


Figure 4.22: Axial velocity distribution at centerline of filter

The normal velocity distributions in Figure 4.23 reveal negative velocities near the endwall for the tangential inlet and step inlet cases. These negative velocities are indicative of flow moving away from the filter, and suggest that the downstream end of the filter is not contributing a proportional share to the filter's performance. The two cases with the angled upper wall maintain positive normal velocities near the endwall, suggesting more effective filter performance. The two cases of the optimized model show the most uniform graph among all other models and highest normal velocity nears the end wall. This figure shows clearly that the optimized model has the best normal velocity distribution.

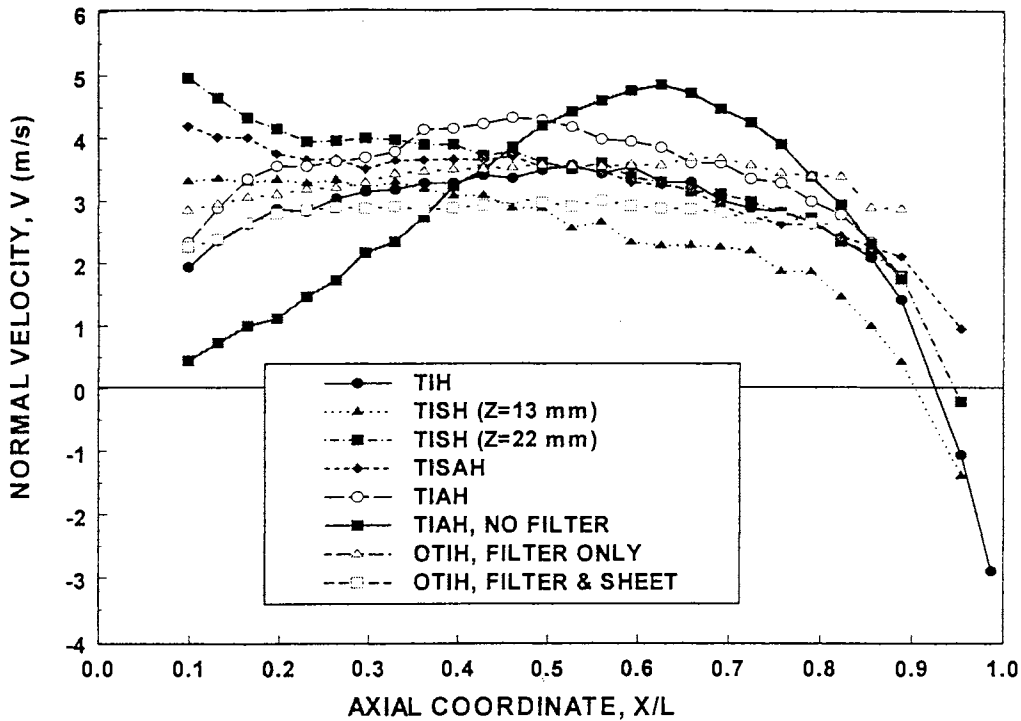


Figure 4.23: Normal velocity distribution at centerline of filter

It should be remembered that these velocity measurements were performed in the plane 13 mm upstream of the filter except for the case of the optimized model at 8 mm and thus are not absolutely representative of the flow as it reaches the tips of the pleats. In its final travel to the filter, the flow could adjust further; changing the velocity distributions from those measured. However, such changes are believed to be small, as shown in the velocity distributions measured at different heights provided in appendix F. Additionally, note that experiments were conducted for a single production engine air filter with certain design and performance characteristics. Other filters, constructed with different media and having different performance characteristics, would produce somewhat different results if subjected to the same tests. Nevertheless, the observed results may be expected to apply qualitatively to other filters. A comparison of results for the filter only and filter with the additional resistance of a sheet of filter media support this argument.

4.5 OPTIMIZED MODEL RESULTS FOR THE CASE OF LAMINAR FLOW

All the results discussed so far were for the case of $212 \text{ m}^3/\text{hr}$ flow rate (which is the design condition of the actual filter) or $Re = 31,000$ at the inlet of the housing which is the duct exit Reynolds number based on the duct hydraulic diameter. In this section the discussion will be focused on the laminar flow or $Re = 2000$ at the housing inlet. Note that the theoretical (optimization) calculations were done for laminar flow at a Reynolds number equal to 2,000.

4.5.1 Optimization program results

Figure 4.24 shows the output of the optimization program. The optimization results have produced a pressure distribution that is very close to the specified uniform distribution, the maximum deviation of the optimized pressure distribution from the optimum are at the beginning and at the end wall. Table C.1 shows the output of the program with all statistical parameters at every point along the axial coordinate.

A detail statistical analysis of table C.1 data will be studied in chapter 5.

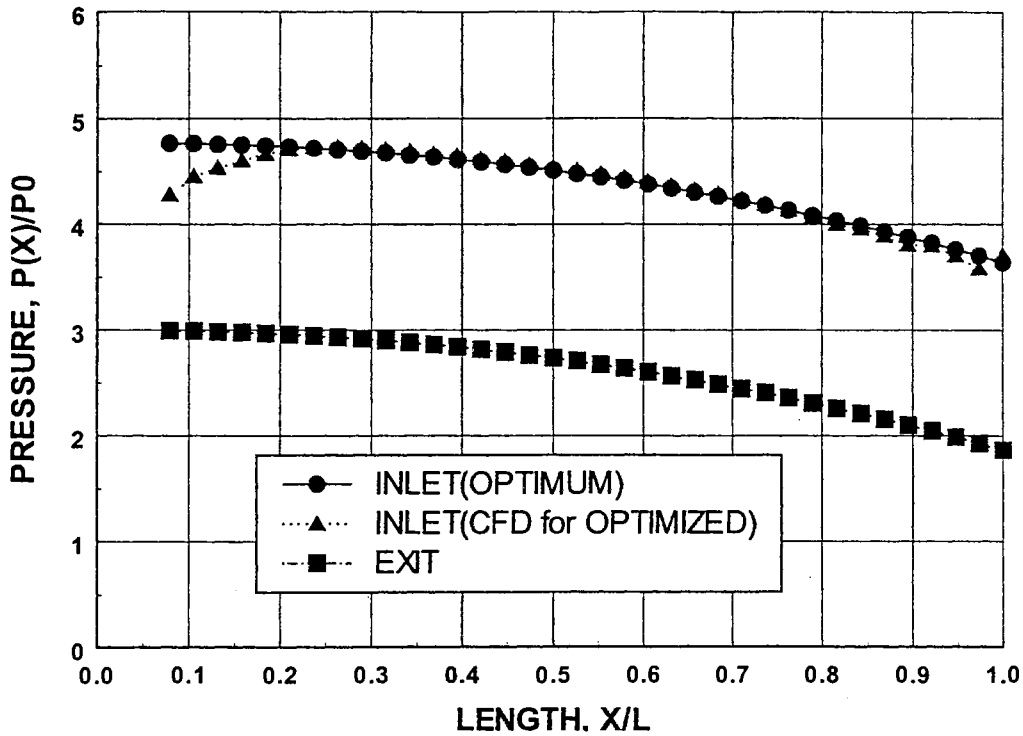


Figure 4.24: Computed pressure distribution resulting from housing design optimization program

4.5.2 Laminar flow velocity distribution results

Axial Velocities

The measured mean velocity distributions in the plane 8 mm above the filter for the case of laminar flow ($Re=2,000$) are shown in Figures 4.25 and 4.26. Figure 4.25 shows the axial mean velocity distributions. Figure 4.26 shows the same component of the velocity but in the case of the filter with a sheet added on the top of it. Both cases (filter only and filter with an additional sheet) have the same trend, velocity decreases toward the endwall of the housing. A comparison between the experimental axial velocity along the centerline of the filter and the CFD result is illustrated in Figure 4.27. Figure 4.28 shows the velocity

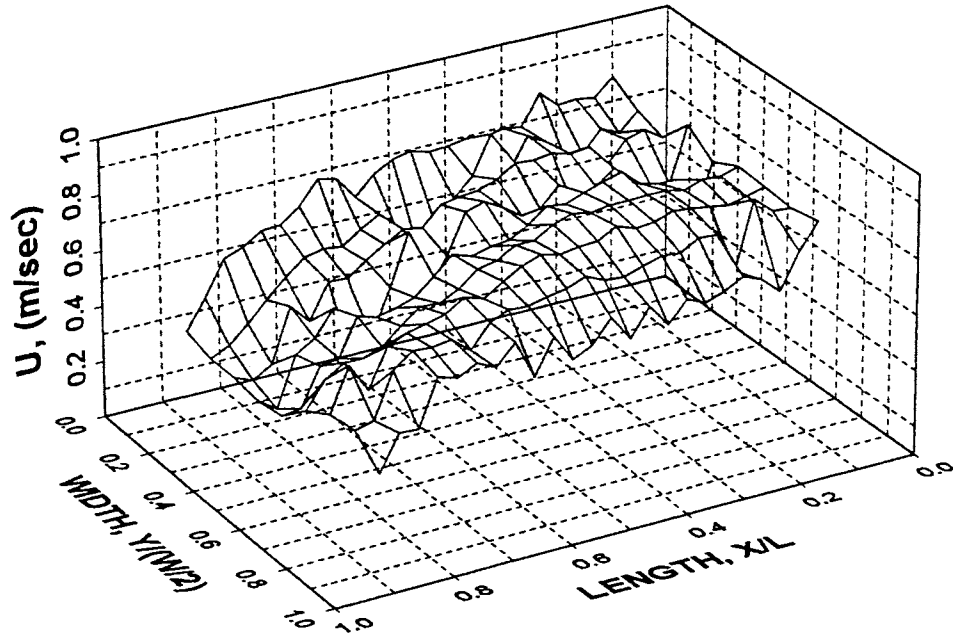


Figure 4.25: Axial velocity distribution 8 mm above filter (Laminar flow, Filter only)

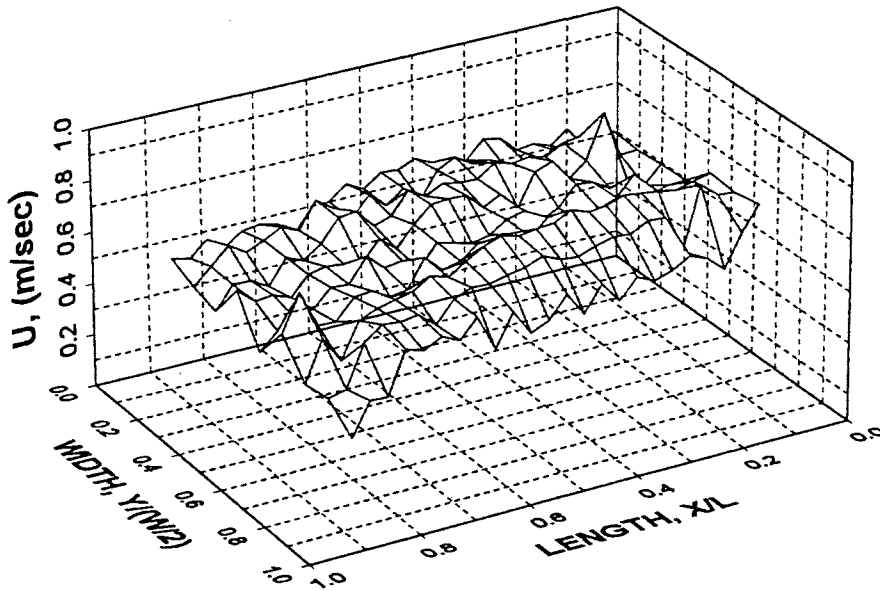


Figure 4.26: Axial velocity distribution 8 mm above filter with an additional sheet (Laminar flow)

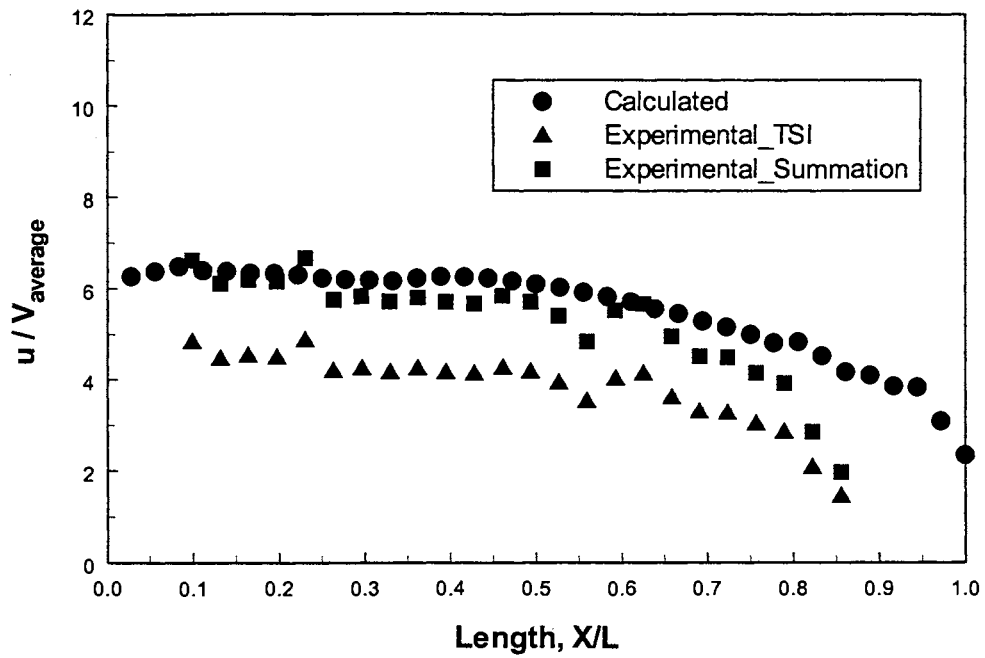


Figure 4.27: Normalized axial velocity distributions: Calculated-Experimental

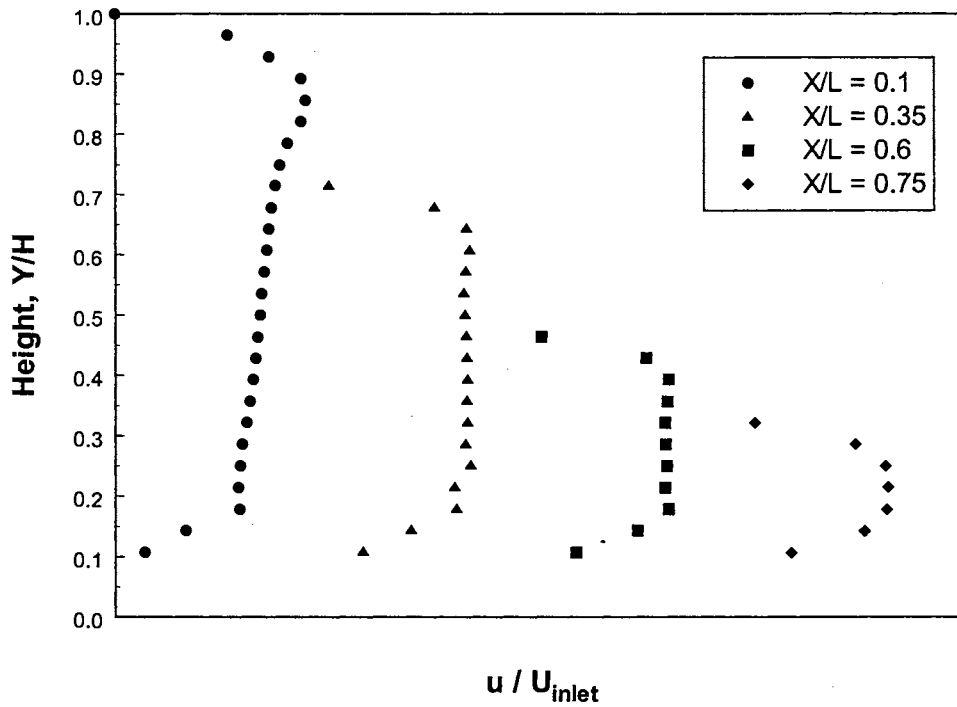


Figure 4.28: Normalized velocity profiles along the housing axial position

profiles along the axial position of the filter resulted from the CFD calculations. Careful attention should be paid to Figure 4.27. Figure 4.27 is normalized based on two different normal average velocities. The first average velocity is based on the flow rate, $14 \text{ m}^3/\text{hr}$, indicated by the TSI Flowmeter for the laminar case ($Re = 2,000$). This flow rate used in the legends named Calculated and Experimental_TSI in Figure 4.27. The second average velocity is based on the flow rate calculated by integration of the normal velocity (experimental results) above the filter. This technique was used due to the following reasons:

First: Figure 4.27 and 4.31 (the axial and normal velocity) showed that the calculated and experimental results have the same trend but the calculated was higher than the experimental.

Second: this was the last measurement performed in the present research and the recent TSI Flowmeter calibration test showed a significant difference between the reading and the actual flow rate.

The average of the absolute values of the percentage of deviations (AAPD as defined in equation 2.32) is 8.9 %. Recall the experimental measurements were performed at the lowest flow rate tested ($14 \text{ m}^3/\text{hr}$). The lowest velocity distributions are very sensitive to the fluctuations of the supplied flow rate. The manual way of controlling the blower flow rate seems to be inconvenient especially at low flow rates. The fluctuations of the supplied flow rate are about 6% of the lowest flow rate itself. Taking the fluctuations of the flow rate into consideration, Figure 4.27 shows a good agreement between the experimental data and the calculated data except at the far end of the housing.

Figure 4.28 shows the axial velocity profiles at different axial positions normalized by the inlet velocity at the duct entrance. The profiles have a very low axial velocity at the surface of the filter and zero velocity at the upper wall (no-slip condition).

Normal Velocities

The mean normal velocity distributions for the case of laminar flow are shown in Figures 4.29 and 4.30 below for cases of the filter only and the filter with an additional sheet respectively. The sheet does not change the profile of the normal velocity significantly even if it seems a little bit more uniform than the case of filter only. Both cases were almost uniform. From these two figures one can say the two dimensional assumption was not a bad assumption.

A comparison between the experimental and calculated velocity distribution at the centerline of the filter is illustrated in Figure 4.31. The average of the absolute values of the percentage of deviations (AAPD as defined in equation 2.32) is 7.5 %. Recall the experimental measurements were performed at the lowest flow rate tested ($14 \text{ m}^3/\text{hr}$). The fluctuations of the supplied flow rate are about 6% of the lowest flow rate itself. Taking the fluctuations of the flow rate into consideration, The normal velocity distributions measured at the centerline of the filter are in good agreement with that calculated by the CFD.

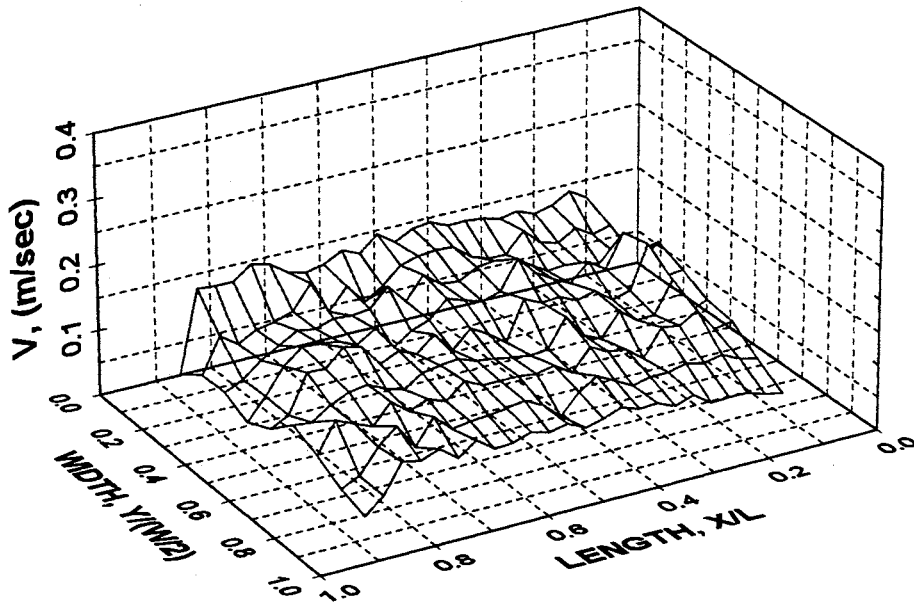


Figure 4.29: Normal velocity distribution 8 mm above filter (Laminar flow, Filter only)

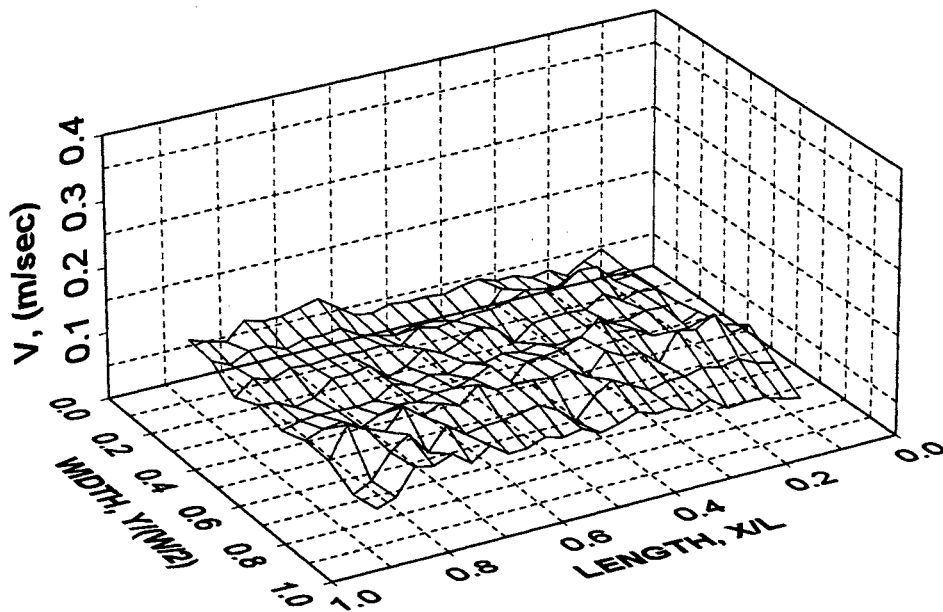


Figure 4.30: Normal velocity distribution 8 mm above filter with an additional sheet (Laminar flow)

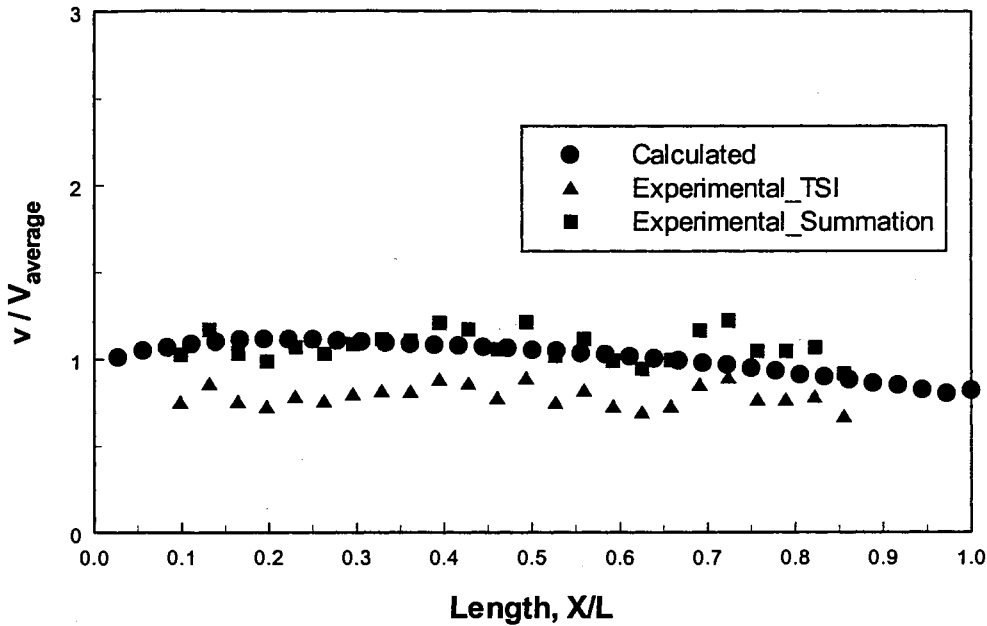


Figure 4.31: Normalized normal velocity distributions: Calculated-Experimental

4.6 OPTIMIZED MODEL PRESSURE MEASUREMENT RESULTS

In this section the pressure distributions at different flow rates will be discussed. The pressure distribution in the inlet plenum of the housing will be discussed first then the pressure in the exit plenum and finally the pressure drop across the filter from the inlet to exit plenum will be discussed. All pressure distribution results have been obtained for the optimized model at 10 positions along the filter (see Figure 3.4). The pressure measurement results will be presented in two forms, the normalized form and the dimensional form. The normalized form of the results will be seen in the coming sections. The dimensional form is in Appendix D. All the pressure measurements were measured taking $P_{i,1}$, which is the first pressure port, 1, in the inlet plenum, i, as a reference pressure in order to be able to use the available range of the pressure transducer. It should be noticed that all the measurements were done 6 mm above the surface of the filter in the inlet plenum of the housing and 6 mm below the filter in the exit plenum of housing.

The pressure exactly at the pleat surface might be different from the pressure 6 mm above or below. Some references for example London et al. (1968) measured the pressure about 12 mm above the face of the matrix stiffener. In this section the pressure tap or port number and its axial position from the housing inlet will be used alternatively. Table 4.2 shows the port number and its axial location normalized by the length of the filter.

Table 4.2: Pressure taps and axial locations

PORTS NUMBER	AXIAL LOCATION (X/L)
1	0.053
2	0.106
3	0.211
4	0.317
5	0.423
6	0.528
7	0.634
8	0.739
9	0.845
10	0.951

4.6.1 Pressure distribution in the inlet plenum of housing

Pressure drop along the inlet duct up to first pressure measurement port (filter only)

Figure 4.32 shows the pressure drop on the way from the inlet (atmosphere) passing through the elbow, mixing box, and the rectangular duct up to the first pressure measurement port (port number 1) which is at 10 mm from the end of the inlet rectangular duct (refer to Figure 3.3). The pressure drop increases with increasing the flow rate in a non-linear way up to 137 m³/hr and then it seems to be increasing linearly.

The maximum pressure drop at 212 m³/hr was about 1 kPa. This figure represents the case of the filter only. The case of filter with an additional sheet in the same way from ambient up to port 1 ($P_{i,1}$) is shown in Appendix D. The sheet does not have any effect on the down stream pressure drop.

Pressure drop as a function of flow rate (filter only)

Figures 4.33 and 4.34 show the pressure distribution at different flow rates for all pressure measurement positions or ports. Note that the port number (the legend of the figure) starts with port number 2 since the measurement has been performed with respect to port 1 so ($P_{i,j}-P_{i,1}$) means the difference in pressure between port j (j goes from 2 to 10) and port 1 in the inlet, i, plenum. Every graph represents one position or port.

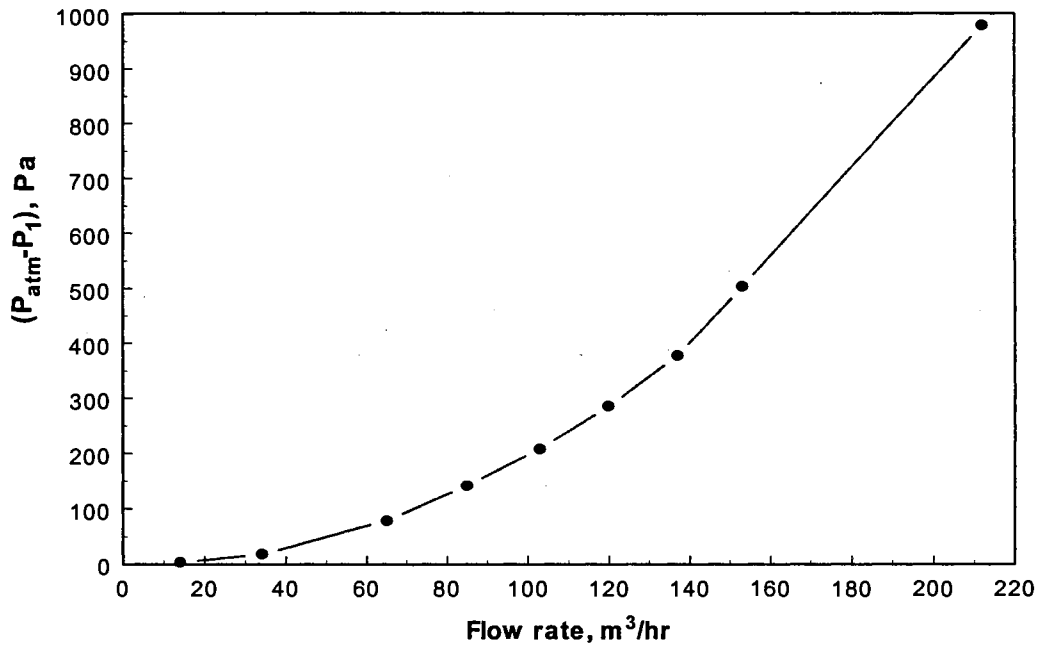


Figure 4.32: Pressure drop: ambient to port 1 (inlet plenum, filter only)

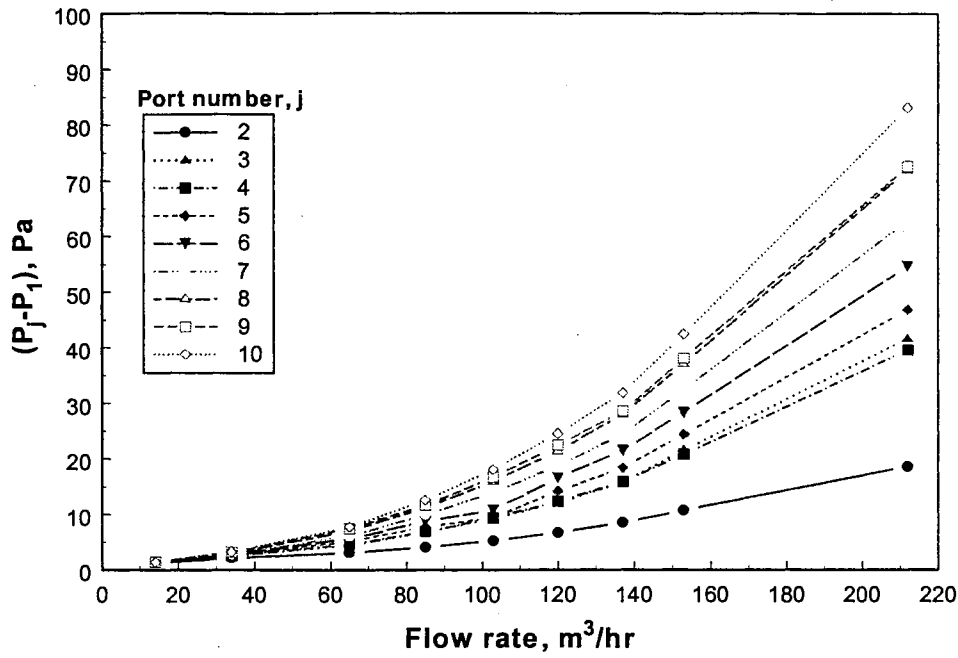


Figure 4.33: Pressure distributions in inlet plenum (filter only)

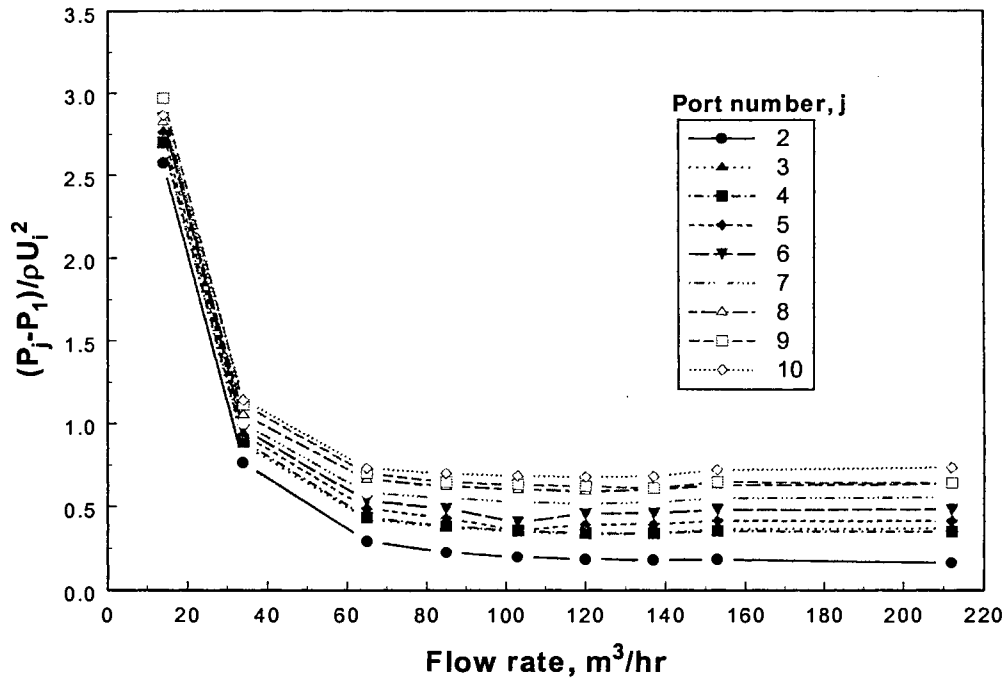


Figure 4.34: Normalized pressure distribution in inlet plenum (filter only)

As the flow rate increases, the pressure increases. All the pressure ports have the same trend. Figure 4.34 is the dimensionless form of Figure 4.33. Figure 4.34 reveals that the dimensionless pressure difference decreases very fast at low flow rate and then stays constant at high flow rate. Port 10 dimensionless pressure number is the largest and then port 9 and so on up to port 2. At the first point of the flow rate ($14 \text{ m}^3/\text{hr}$) the flow was laminar, at the second, the flow might be in the transition region and at high flow rate the flow is turbulent. The graphs exhibit the same trend (constant value) at high flow rate. The previous trend will be noticed clearly later when the graphs show the port numbers as a dependent variable (abscissa) at a certain Reynolds number or flow rate.

Pressure drop distribution along the filter (filter only)

In this section the Reynolds numbers (flow rate) will be constant and the axial coordinate will be the dependent variable (abscissa). The pressure drop along the filter increases from port 1 to 10. The maximum pressure was at $212 \text{ m}^3/\text{hr}$ and the minimum was at $14 \text{ m}^3/\text{hr}$ (refer to Figure D.2 in appendix D). Figure 4.35 shows the non-dimensional pressure distribution along the filter. The dimensionless pressure number slightly increases in moving from port 1 ($X/L = 0.053$) to 10 ($X/L = 0.95$). The most interesting behavior in this figure is the self-similar behavior of the graphs. The upper graph is at $14 \text{ m}^3/\text{hr}$ or $Re = 2,000$ which is the laminar case and it has a dimensionless pressure number almost 2.5 times the next one, at $34 \text{ m}^3/\text{hr}$, corresponding to $Re = 4,900$. The rest of the graphs have self similar behavior at about 0.5 dimensionless pressure number and flow rates from 65 to $212 \text{ m}^3/\text{hr}$ which corresponds to Re from $12,000$ to $31,000$ which is pure

turbulent flow. One may classify the flow as laminar at 2.5 non-dimension pressure number and transition at about 1 and turbulent at about 0.5.

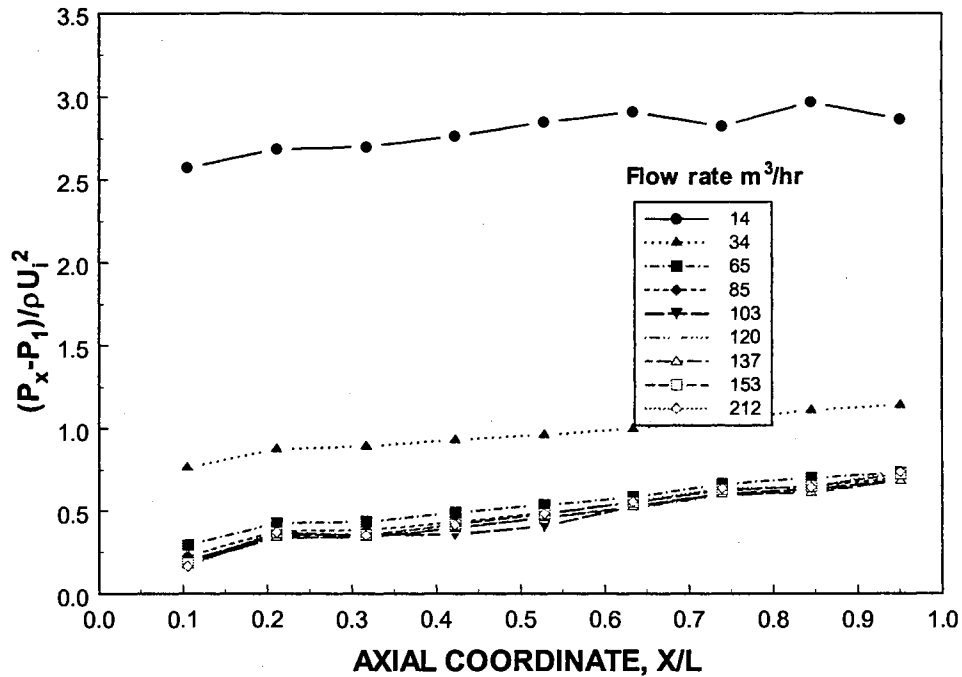


Figure 4.35: Normalized pressure distribution in inlet plenum at different ports (filter only)

Pressure drop as a function of flow rate (filter with an additional sheet)

The pressure drop in the inlet plenum of the housing in the case of the filter and an additional sheet is shown Appendix D. The pressure increases with increasing the flow rate and the highest pressure occurs at port number 10 while the minimum pressure at port number 2. The graphs in this case have the same trend as in the case of filter only. Figure 4.36 shows the normalized pressure drop distributions in the inlet plenum of the housing and it behaves the same way as in the case of the filter only. The distributions become straight lines at high flow rate.

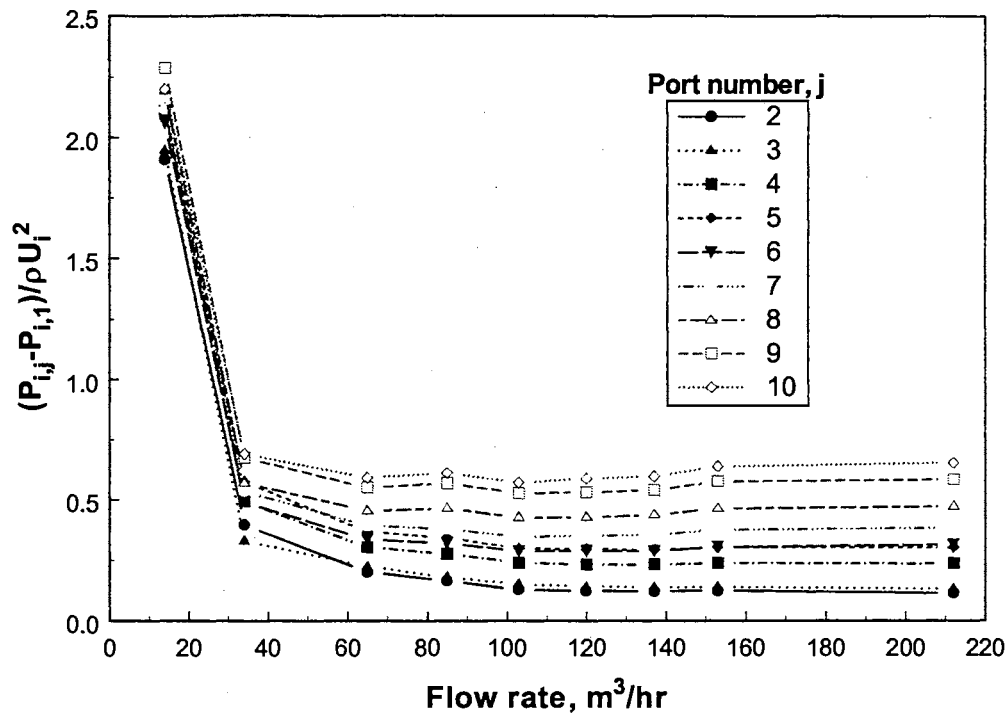


Figure 4.36: Normalized pressure distributions in inlet plenum (filter with an additional sheet)

Pressure drop as a function of port number (filter with an additional sheet)

The pressure distribution in the inlet plenum of the housing for the case of filter and sheet is presented in Appendix D (Figure D.6). The case of filter and sheet seems to have the same trend as the case of filter only in the inlet plenum measurements of the housing. Figure 4.37 shows the normalized form of the pressure distributions in case of filter and sheet, and once again the self-similar behavior appears in the case of filter and sheet the same way as in the case of filter only. The low flow rate (laminar) has a plot away from the high flow rate (turbulent flow) which has the same self-similar behavior. At 34 m³/hr the plot again seems to be in a transition region between laminar and turbulent.

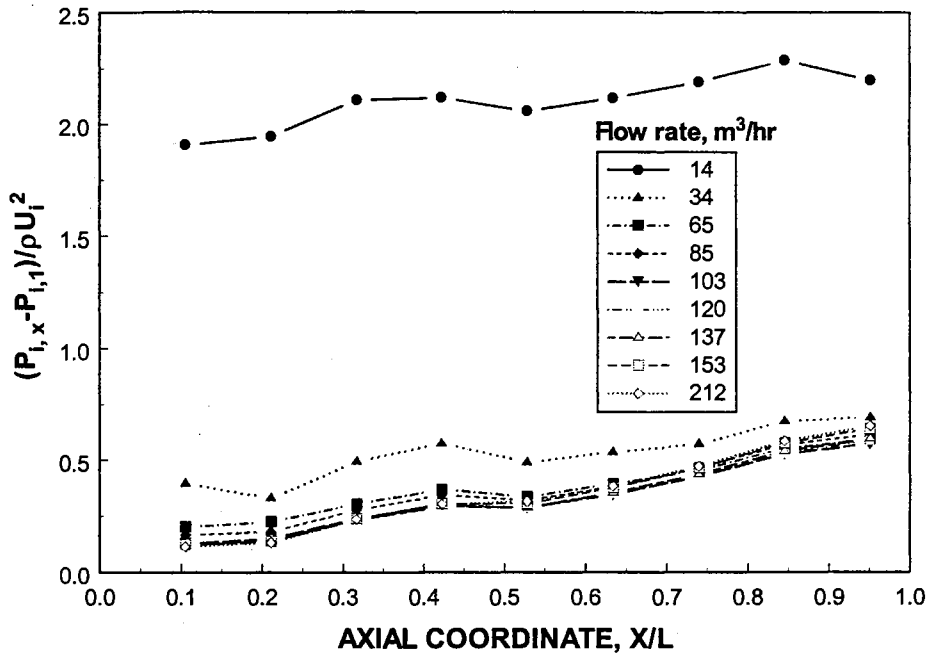


Figure 4.37: Normalized pressure distribution in inlet plenum at different ports (filter with an additional sheet)

4.6.2 Pressure distribution in the exit plenum of housing

In this section the pressure distribution in the exit plenum of the housing will be discussed from the same points of view as in the inlet part. It should be noticed that the pressure ports in this part are at the same axial distance as in the inlet part and at the same distance below the filter (6 mm) as in the inlet part (6 mm above the filter). The difference in the pressure in this section was measured with respect to the port number 1 in the inlet plenum of the housing. The pressure difference will be $(P_{i,1} - P_{e,j})$. $P_{i,1}$ means the port number 1 in the inlet part and $P_{e,j}$ means the exit port numbers (j goes from 1 to 10).

Pressure drop as a function of flow rate (filter only)

The pressure distributions in the exit plenum at different flow rate for certain port number are shown in Appendix D (Figure D.7). The pressure increases as the flow increases for all ports in the exit plenum of the housing. The maximum pressure drop occurs at port number 10 and the lowest at port number one. The same trend has been found in the inlet part except that the pressure drop in this case is much larger than in the inlet plenum. The maximum pressure drop in the exit plenum is about 500 Pa but in the inlet part it was about 80 Pa. Figure 4.38 shows the non-dimensional pressure distribution. The pressure dimensionless number drops rapidly at low flow rate (laminar flow) and stays almost constant at high flow rate (turbulent flow). This trend also was found in the inlet plenum except that here in the exit plenum the graphs are closer to each other more than in the inlet flow and the self-similar behavior is clearer.

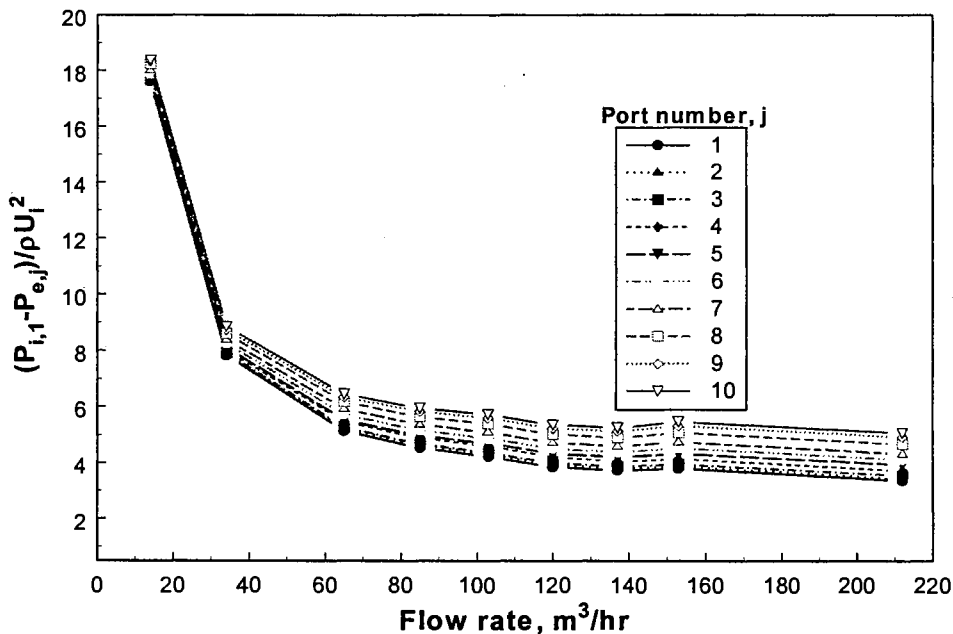


Figure 4.38: Normalized pressure distributions in exit plenum (filter only)

Pressure drop distribution along the filter (filter only)

The pressure distribution in the exit plenum for the case of filter only in a dimensional form is presented in Appendix D (Figure D.8). The pressure at port 10 was the maximum for all flow rates and at port 1 was the minimum for all flow rates. The pressure is increasing with increasing flow rate. The slope of the graphs increases as the flow rate increases. At the lowest flow rate the pressure graph has the lowest slope. Figure 4.39 shows the dimensionless form of Figure D.8. Again, as in the inlet plenum, self-similar behavior appears in the exit plenum. The laminar flow has the maximum non-dimensional pressure number, which is about 18 while in the inlet plenum it was 2.5. The high flow rate graphs (turbulent flow) have a pressure dimensionless number equal to about 4 whereas in the inlet plenum it was about 0.5.

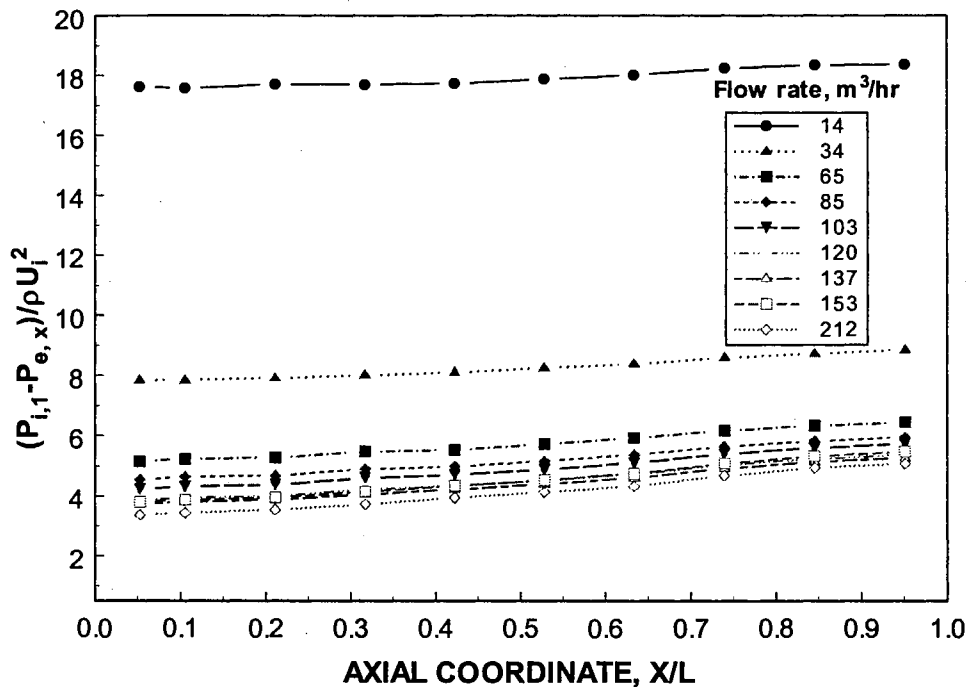


Figure 4.39: Normalized pressure distributions in exit plenum (filter only)

Pressure drop as a function of flow rate (filter with an additional sheet)

In this section the pressure distribution in the exit plenum for the case of the filter and additional sheet will be discussed. The effect of the sheet appears clearly in Figures D.9 and 4.40. The pressure distribution in the exit plenum for the case of filter and sheet has the same trend as in the filter only case but with a larger pressure drop. For the filter only case the maximum pressure drop was about 500 Pa, but in this case it is about 2,000 Pa. The most interesting thing in this case is that the sheet made all the graphs coincide. In Figure 4.40 the dimensionless number drop from about 95 at low flow rate (laminar flow) down to about 20 at the maximum flow rate whereas in the case of the filter only the maximum was about 18 and dropped down to about 4.

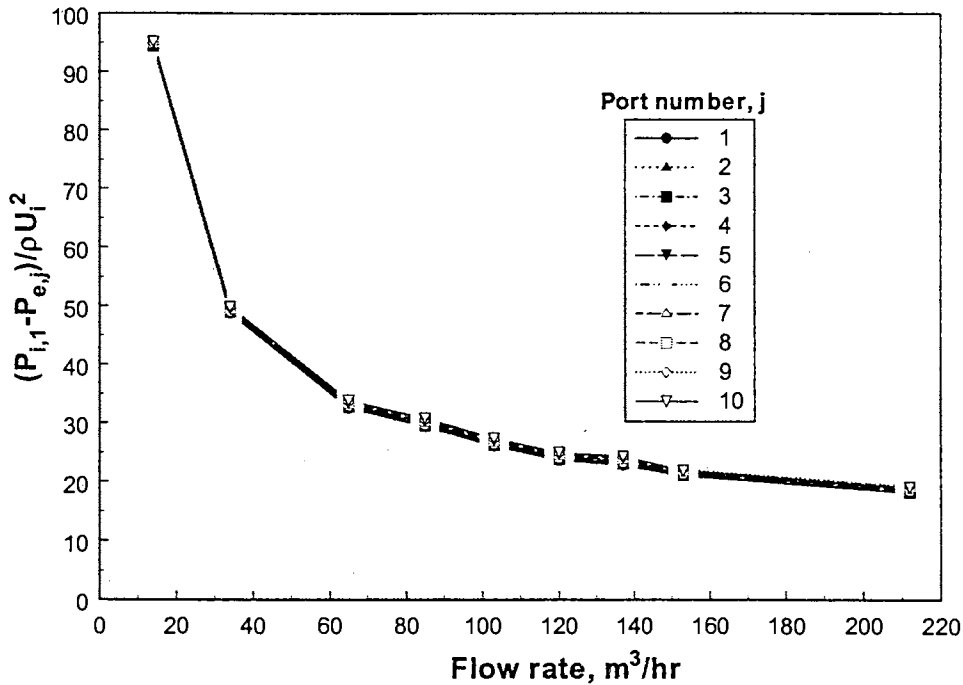


Figure 4.40: Normalized pressure distributions in exit plenum (filter with an additional sheet)

Pressure drop as a function of port number (filter with an additional sheet)

In this section the pressure distribution in the exit plenum of the housing will be discussed for the case of the filter and additional sheet. Figure D.10 shows the pressure drop in the exit plenum with respect to port 1 in the inlet plenum. The pressure drop is almost constant for all ports at the same flow rate. The pressure is higher at higher flow rate. The maximum pressure drop was at 212 m³/hr equal to 2,000 Pa compare to about 450 in case of filter only at the same flow rate. Figure 4.41 shows the dimensionless pressure coefficient. The dimensionless pressure number distributions is almost constant and much larger than in the case of the filter only. It was at 212 m³/hr equal to 95 compared to 18 in the case of the filter only at the same flow rate.

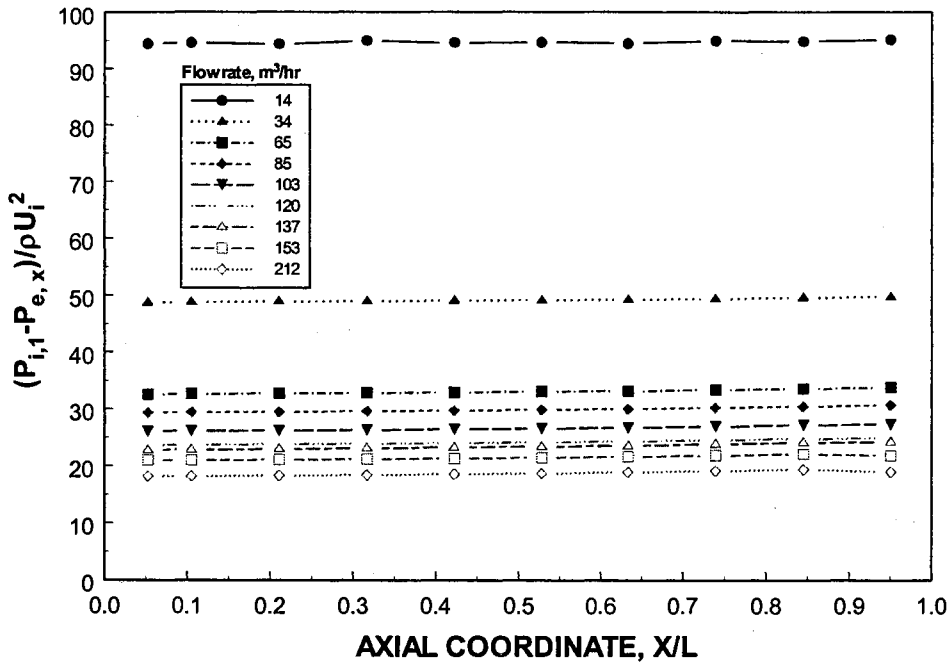


Figure 4.41: Normalized pressure distributions in exit plenum (filter with an additional sheet)

The effect of adding the sheet on the pressure drop variation with port number can be summarized as: first the sheet adds more pressure drop to the filter, second, the sheet makes the distribution of the pressure drop in the exit part about uniform at all ports.

4.6.3 Pressure drop across the filter (filter only)

In this section the pressure distribution across the filter from inlet plenum to exit plenum will be discussed. The differential pressure in all figures is the difference between every two ports at the same distance from the entrance duct position (at same x-coordinate) for example port 1 at the inlet plenum and 1 at the exit plenum and so on.

Pressure drop across the filter as a function of flow rate (filter only)

The dimensional pressure drop across the filter is illustrated in Appendix D (Figure D.11). The pressure drop increases as the flow rate increases in a non-linear way. All ports have the same trend. Port 10 has the maximum pressure drop while port 1 has the minimum. The maximum pressure drop was for port 10 at $212 \text{ m}^3/\text{hr}$ equal to 600 Pa. The normalized pressure drop across the filter is shown in Figure 4.42. For all port numbers the dimensionless pressure number drops from about 20 at low flow rate (laminar flow) down to about 5 for the high flow rates (turbulent flow). At high flow rate the variation of the pressure drop is very small compared to that at low flow rate.

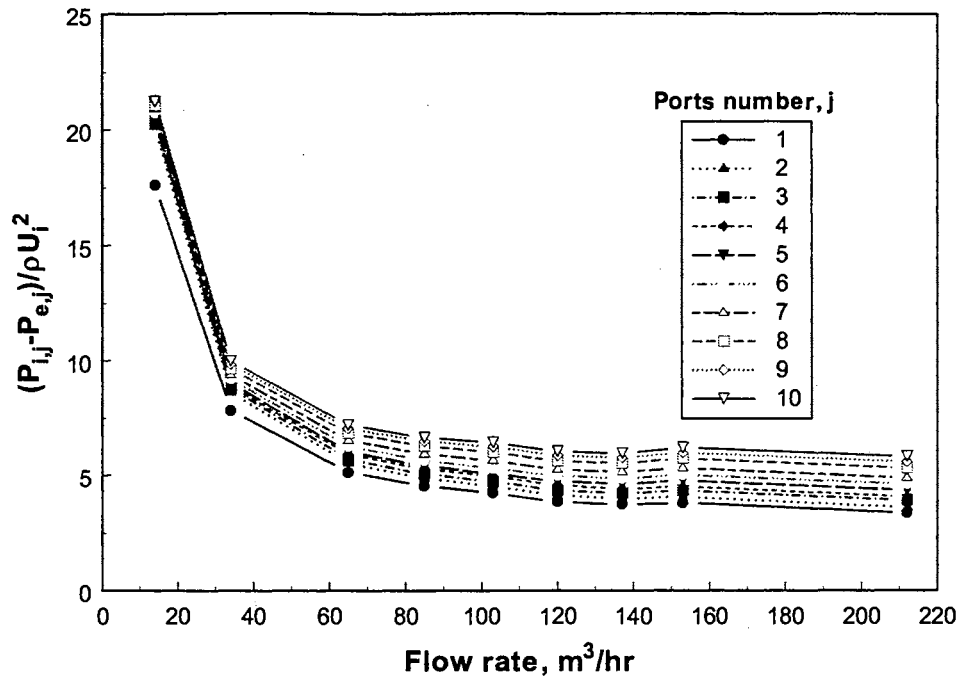


Figure 4.42: Normalized pressure drop across the filter (filter only)

Pressure drop across the filter as a function of port number (filter only)

The distribution of the pressure drop across the filter in dimensional form is presented in Appendix D (Figure D.12). The normalized pressure drop across the filter is shown in figure 4.43. The pressure drop across the filter is a function of two parameters, first the flow rates and second the port number or the axial coordinate along the filter. The pressure drop increases as the flow rate increases. The pressure drop increases with moving toward port number 10 from the entrance to the end wall. The maximum pressure drop across the filter occurs at port number 10 and 212 m³/hr near the end wall of the housing and is equal to about 650 Pa. The pressure drop across the filter was nearly uniform at 14 m³/hr (laminar flow) which is good agreement with the numerical calculation. Figure 4.43 shows the dimensionless pressure drop distributions across the

filter. In this figure the laminar flow ($14 \text{ m}^3/\text{hr}$) has a constant value except at the first point. At high flow rate (turbulent flow) the dimensionless pressure number increases as the port number increases. In this figure the self-similar behavior appears clearly: the laminar flow appears distinct from the turbulent flow.

Pressure drop across the filter as a function of flow rate (filter with an additional sheet)

For different flow rates the pressure drop across the filter is shown in figure 4.44. The dimensional form of this figure can be found in appendix D (Figure D.13). The pressure drop has the same trend as in case of the filter alone except in two things. First, the pressure drop is much larger and the port number graphs coincide. The maximum pressure drops in the case of the filter and additional sheet at $212 \text{ m}^3/\text{hr}$ was about 2,200 Pa whereas it was 600 Pa in the case of filter only, in a ratio of about 4. Figure 4.44 shows the non-dimensional pressure drop across the filter. The difference between Figure 4.42 (filter only) and Figure 4.44 is clear now. The non-dimensional pressure drops in the case of the filter and an additional sheet is about 4 times larger than in the case of the filter only. The graphs of different port number exhibit exactly the same trend, which means the sheet made the pressure drop more uniform. This behavior will be seen again when the pressure drop will be discussed in terms of port number in the next paragraph.

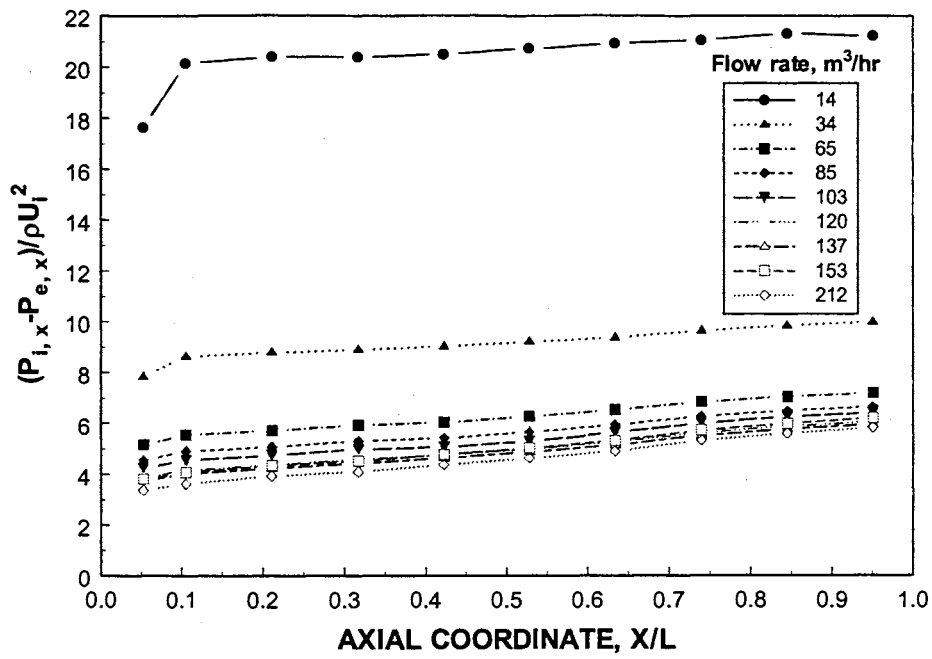


Figure 4.43: Normalized pressure distributions across the filter at different ports (filter only)

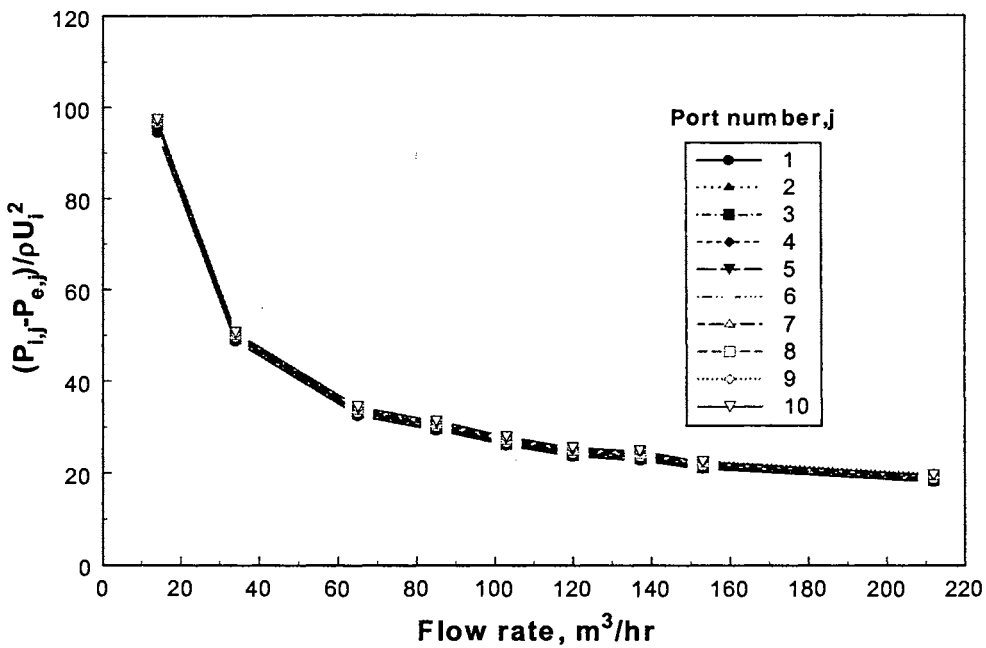


Figure 4.44: Normalized pressure distributions across the filter at different flow rate (filter with an additional sheet)

Pressure drop across the filter as a function of port number (filter with an additional sheet)

The effect of the filtration material sheet on the pressure drop across the filter with an additional sheet is discussed in this section. The dimensional form of the present result can be found in Appendix D (Figure D.14 I). The pressure drop across the filter and additional sheet at all ports is nearly uniform for all port numbers especially at lower flow rates. At high flow rate the pressure drop is higher than that at lower flow rates. The maximum pressure drop was at 212 m³/hr and equal to 2,000 Pa compared to about 500 in case of filter only.

Figure 4.45 shows the dimensionless pressure drop across the filter and additional sheet. This number is uniform for all ports at the same flow rate. The maximum number was at 212 m³/hr and equal to about 95 compared to 20 in the case of the filter only. Again the three regions (Laminar, transition and turbulent) appear in this figure.

In general, the effect of adding the sheet to the filter has two results:

- 1) The pressure drop increases up to 4 times
- 2) The pressure drop becomes more uniform

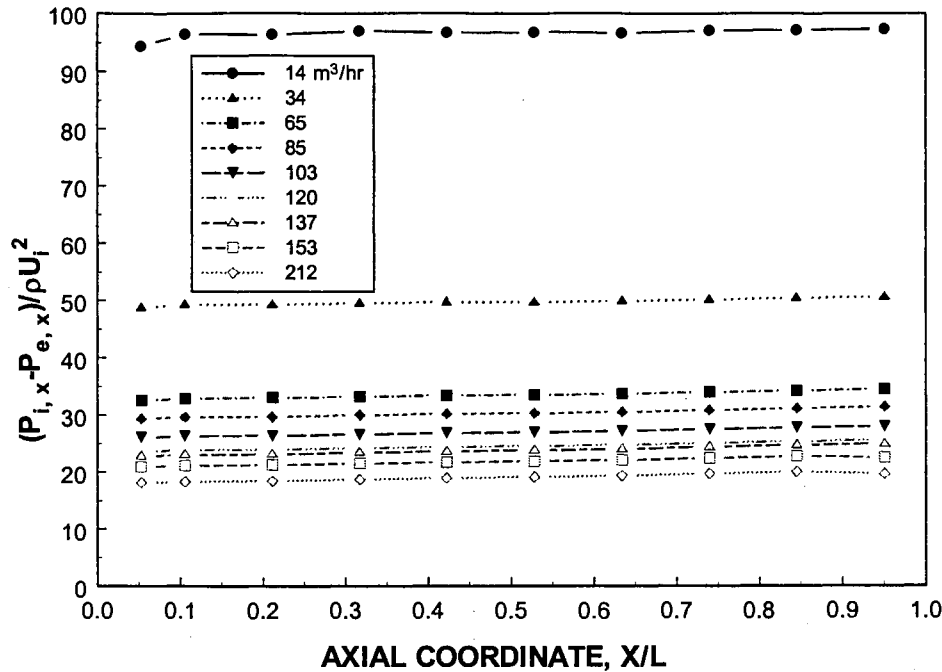


Figure 4.45: Normalized pressure distributions across the filter at different ports (filter with an additional sheet)

4.7 COMPARISON OF PRESSURE DROP ACROSS THE FILTER FOR CALCULATED AND EXPERIMENTAL MEASUREMENTS

Figures 4.46 and 4.47 show the calculated and experimental results for both cases of the filter only and the filter with an additional sheet (laminar flow). It should be noticed that the experimental measurements and the theoretical calculations were done at 2,000 Reynolds number. Figure 4.47 shows the result for the case of filter only. The calculation was obtained without the presence of the filter and the measurement was performed with the presence of the filter. The calculated result is drawn with an added constant, which should represent the resistance of the filter just to shift the graph up to compare the trend of the calculated pressure distribution profile with the trend of the experimental result profile. There is a similar uniform trend between the calculated result and the

experimental result except at the first measurement point.

Figure 4.47 shows the results of the case of the filter with an additional sheet. The case of the filter and an additional sheet had more agreement with the calculated results. Both profiles have the same trend. The sheet added more resistance and made the pressure more uniform. The dimensionless pressure number in the case of the filter only was about 20 and in the filter and an additional sheet case was about 97. The sheet added about 77 units of non-dimensional resistance to the filter (the 77 units added to compare the trend of the two profiles).

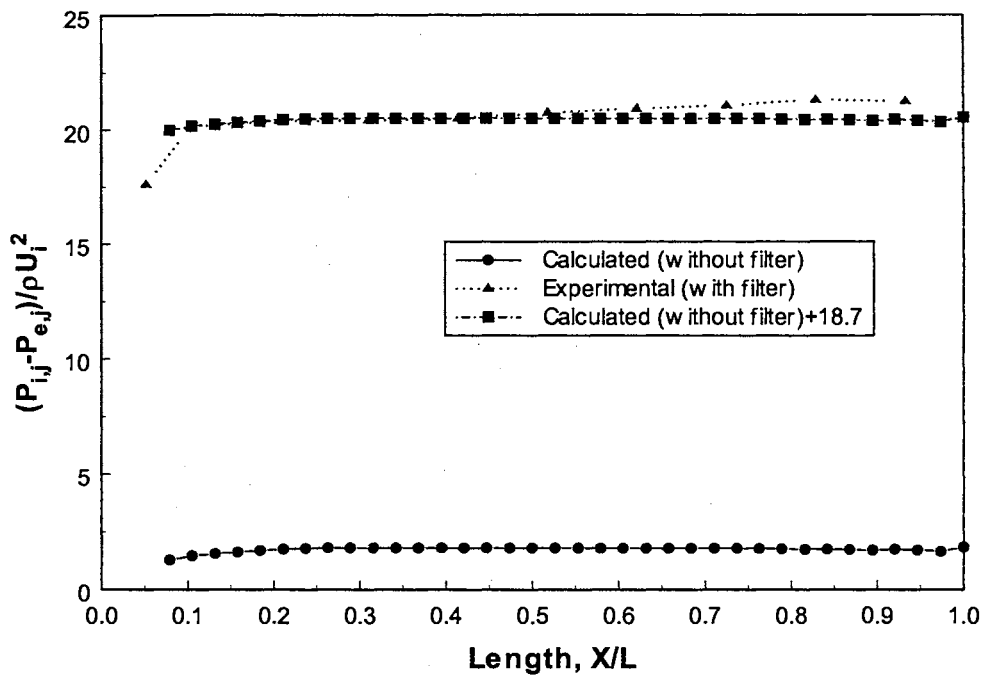


Figure 4.46: Comparison of the trend of the calculated-experimental results of pressure drop across filter (filter only, laminar flow)

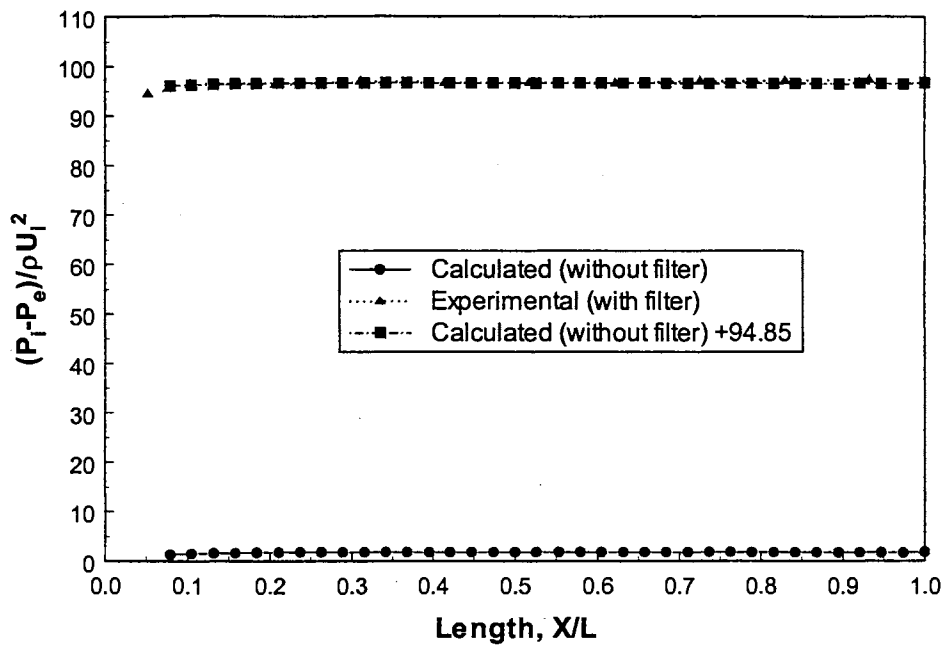


Figure 4.47: Comparison of the trend of calculated-experimental results of pressure drop across filter (filter with an additional sheet, laminar flow)

4.8 CALCULATED CLEAN FILTER EFFICIENCY DISTRIBUTIONS

Clean filter elemental filtration efficiency distributions were calculated for the measured velocity distributions using the filtration models previously described. Calculations were performed for a range of different monodisperse particle sizes. A 1 μm particle was used only as a seed for the velocity measurements. This measured velocity was used in a filtration model to calculate the different filtration efficiencies. The results will be presented using assumptions of perfect and of imperfect adhesion.

4.8.1 Tangential inlet housings

Figures 4.48 and 4.49 display the behavior of the elemental efficiencies for the tangential inlet housing (the rectangular box shape) for 1 μm diameter particles. The efficiencies are increased in regions of high local velocity near the centers of the filters.

Figures 4.50 and 4.51 represent predictions of local efficiency for 10 μm diameter particles for tangential inlet housing. These efficiencies are very high and nearly uniform. For these particles and velocities, the Stokes numbers corresponds to values greater than 1, the upper plateau illustrated in Figure 2.5.

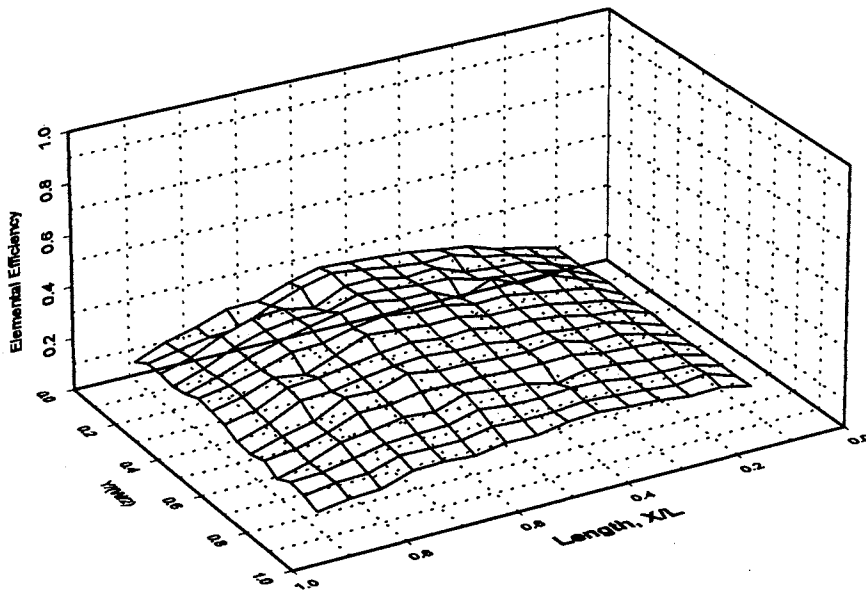


Figure 4.48: Elemental efficiency predictions for TIH model, 1 μm diameter particles (Perfect adhesion model)

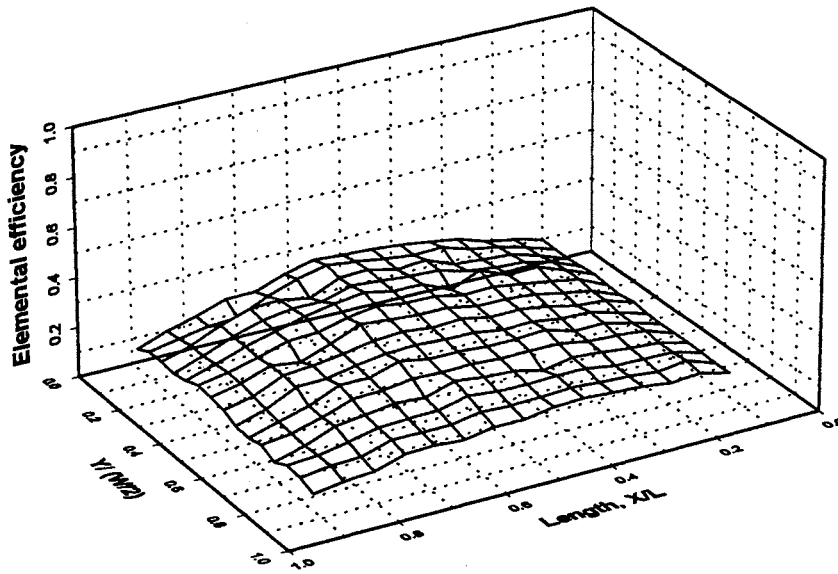


Figure 4.49: Elemental efficiency prediction for TIH model, 1 μ m diameter particles (Imperfect adhesion model)

Figures 4.52 and 4.53 show the predictions of the elemental efficiency for tangential inlet with step housing for both cases of perfect and imperfect adhesion models being applied. The efficiencies are high at the entrance (high velocity regions) and decrease toward the end wall of the housing (low velocity regions). The effect of the adhesion model appears more significant at high particle diameter than at low diameter particle.

Figures 4.54 and 4.55 show the elemental efficiency for the same housing but for 10 μ m particles instead of 1 μ m. The efficiency is high and uniform in the case of the perfect adhesion model as shown in Figure 4.54. In the case of the imperfect adhesion model it is low at the entrance (the high velocity regions) and high at the end of the housing (low velocity regions).

Figures 4.56 and 4.57 show the cases of perfect and imperfect adhesion models applied to tangential inlet with angle housing results. Figure 4.56 shows the elemental efficiency in

case of perfect adhesion and Figure 4.57 shows the imperfect adhesion case. The efficiency is high at regions of high velocity and low at the low velocity regions. The perfect adhesion assumption is not believed to be of major significance for the small particles.

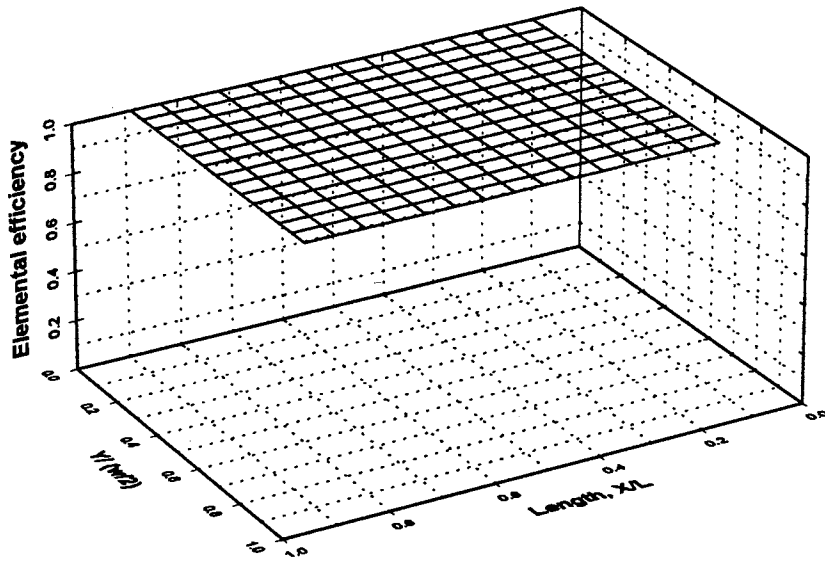


Figure 4.50: Elemental efficiency prediction for TIH model, 10 μ m diameter particles (Perfect adhesion model)

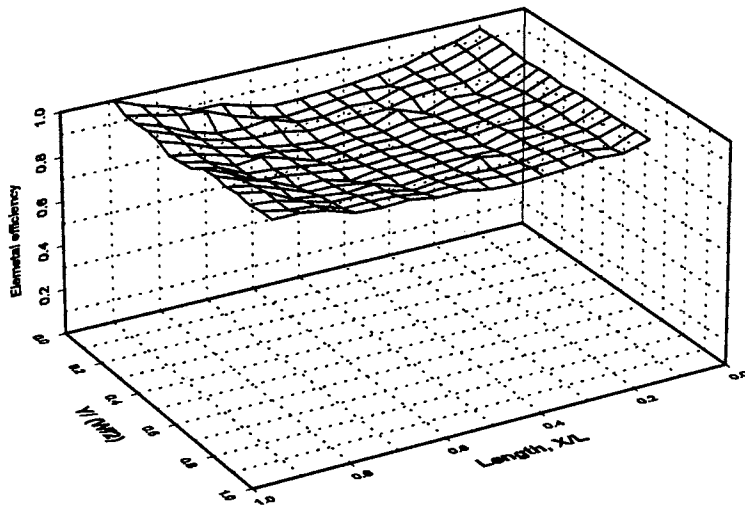


Figure 4.51: Elemental efficiency predictions for TIH model, 10 μ m diameter particles (Imperfect adhesion model)

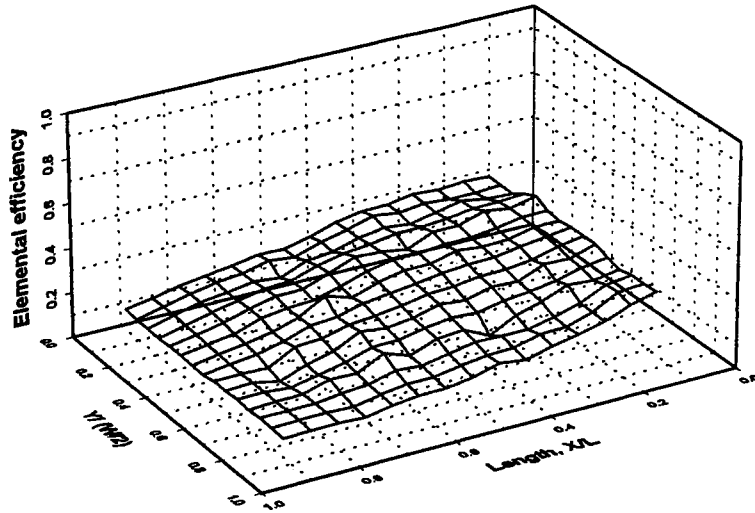


Figure 4.52: Elemental efficiency predictions for TISH model, 1 μ m diameter particles (Perfect adhesion model)

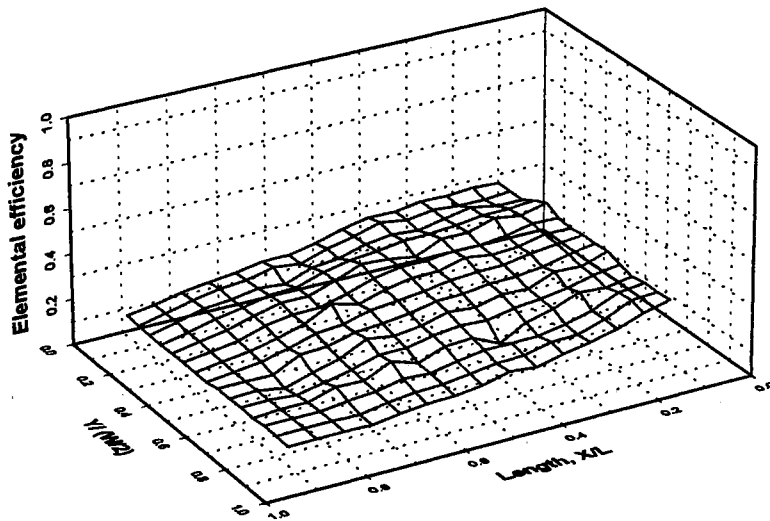


Figure 4.53: Elemental efficiency predictions for TISH model, 1 μ m diameter particles (Imperfect adhesion model)

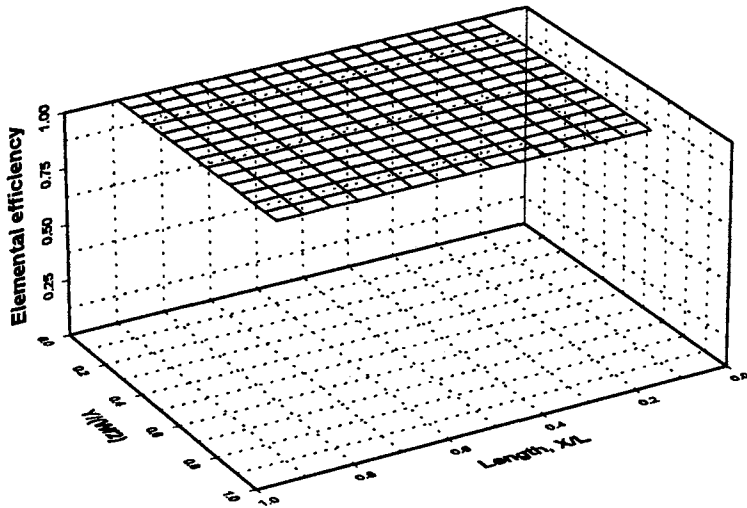


Figure 4.54: Elemental efficiency predictions for TISH model, 10 μ m diameter particles (Perfect adhesion model)

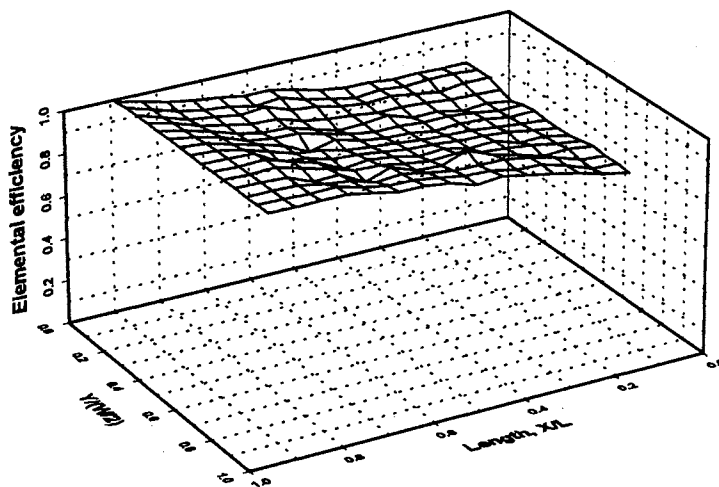


Figure 4.55: Elemental efficiency predictions for TISH model, 10 μ m diameter particles (Imperfect adhesion model)

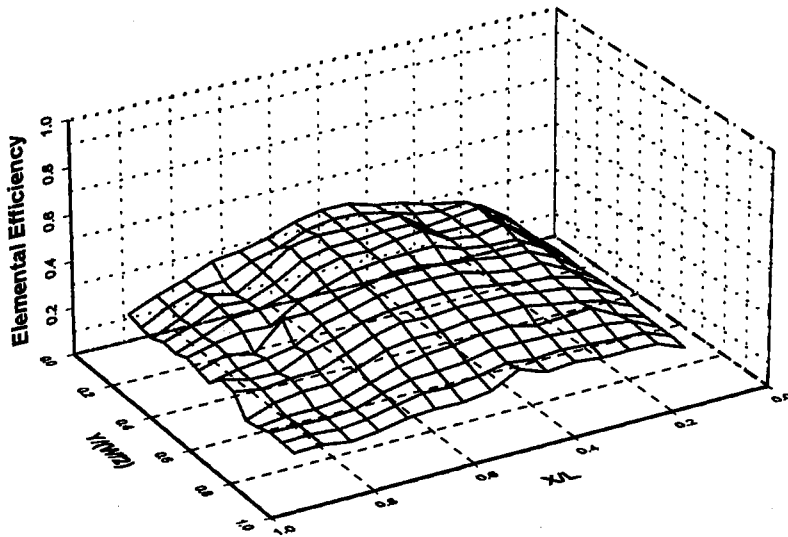


Figure 4.56: Elemental efficiency predictions for TIAH model, 1 μ m diameter particles (Perfect adhesion model)

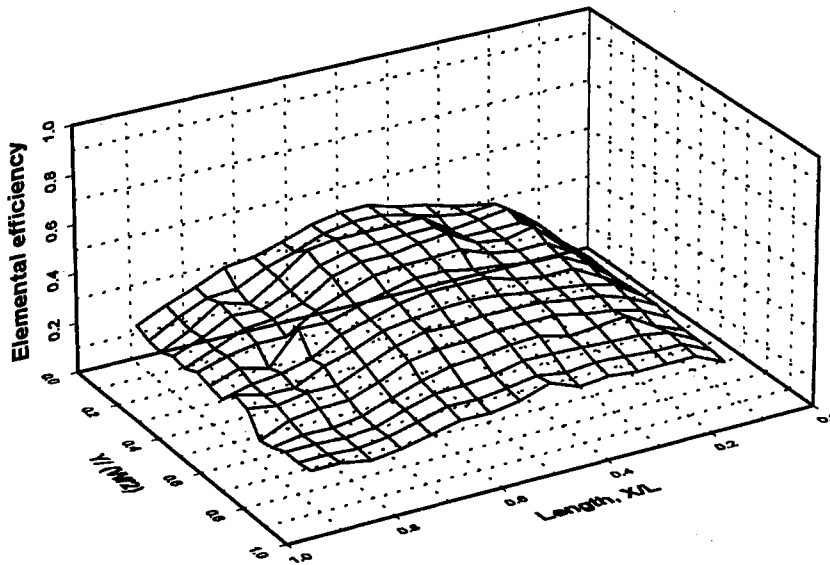


Figure 4.57: Elemental efficiency predictions for TIAH model, 1 μ m diameter particles (Imperfect adhesion model)

Figures 4.58 and 4.59 show the elemental efficiency predictions for 10 μm particle diameter for both cases of the perfect and imperfect adhesion models respectively. Figure 4.58 shows a uniform and high efficiency in the case of applying the perfect adhesion model. Figure 4.59 shows the imperfect adhesion model applied to the same housing. The efficiency is minimum at the center region of the filter, which is the high velocity region. The trend of this graph is opposite to that of the velocity distribution graph.

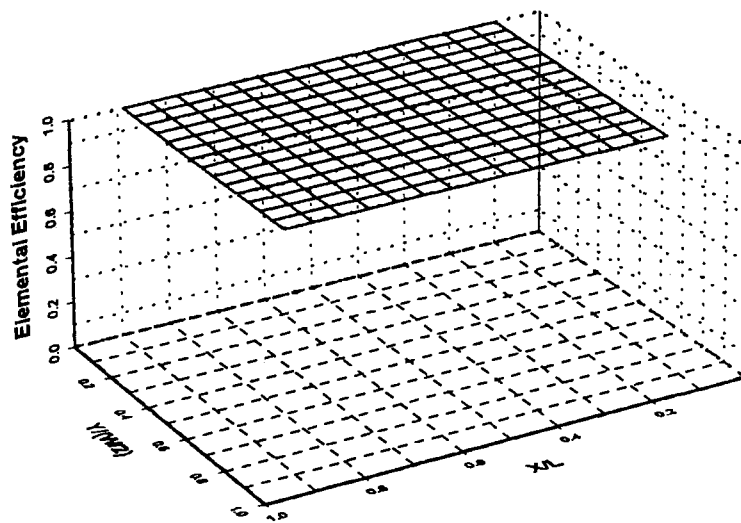


Figure 4.58: Elemental efficiency predictions for TIAH model, 10 μm diameter particles (Perfect adhesion model)

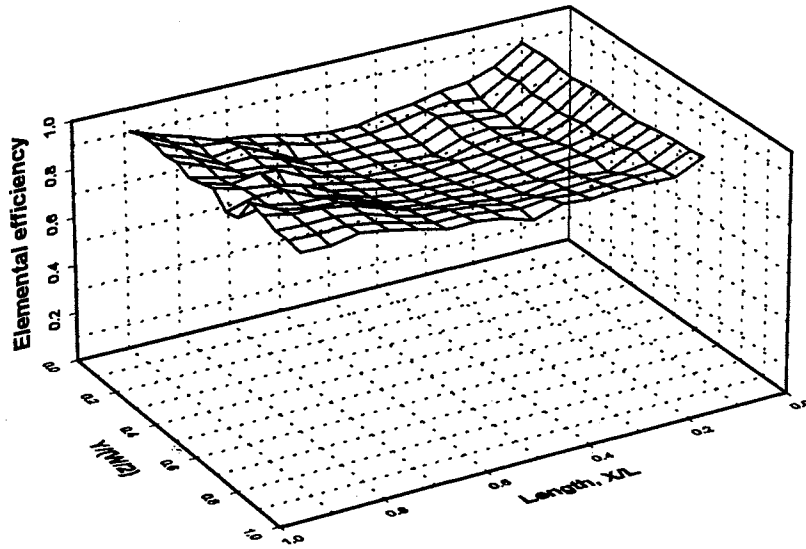


Figure 4.59: Elemental efficiency predictions for TIAH model, 10 μ m diameter particles (Imperfect adhesion model)

4.8.2 Normal inlet housing (NIH)

Figures 4.60 and 4.61 display the behavior of the elemental efficiency for 1 μ m particles for the normal inlet housing. Figure 4.60 presents the perfect adhesion assumption and 4.61 presents the imperfect adhesion. The efficiencies are increased in regions of high local velocity near the centers of the filters in the case of tangential without step and near the entrance in the case of tangential with step housing. The increase is more extreme for the normal entry housing than the tangential inlet housing, because the velocity variation is much larger. This effect results from the local Stokes number for the filtration moving up the knee of the curve shown in Figure 2.5.

Figures 4.62 and 4.63 represent predictions of local efficiency for 10 μ m diameter particles. Calculation results for these particles are presented for both perfect and

imperfect, modeled adhesion in Figures 4.62 and 4.63 respectively. Note that the axis of Figure 4.63 has been rotated so that the axial centerline of the housing is along the x-axis, rather than at the back as in Figure 4.62 and most of the previous figures. The efficiencies for perfect adhesion are very high and uniform. For these particles and velocities, the Stokes numbers correspond to values greater than 1, the upper plateau illustrated in Figure 2.5 for perfect adhesion. The imperfect adhesion or reentrainment effect for these large particles is very dramatic, particularly for the center of the normal entry housing, where velocities are very large.

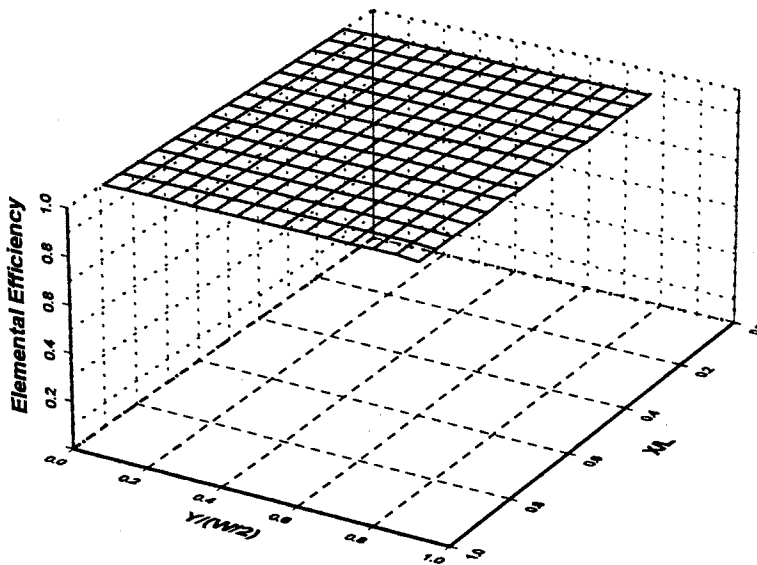


Figure 4.60: Elemental efficiency predictions for NIH model, 1 μ m diameter particles (Perfect adhesion model)

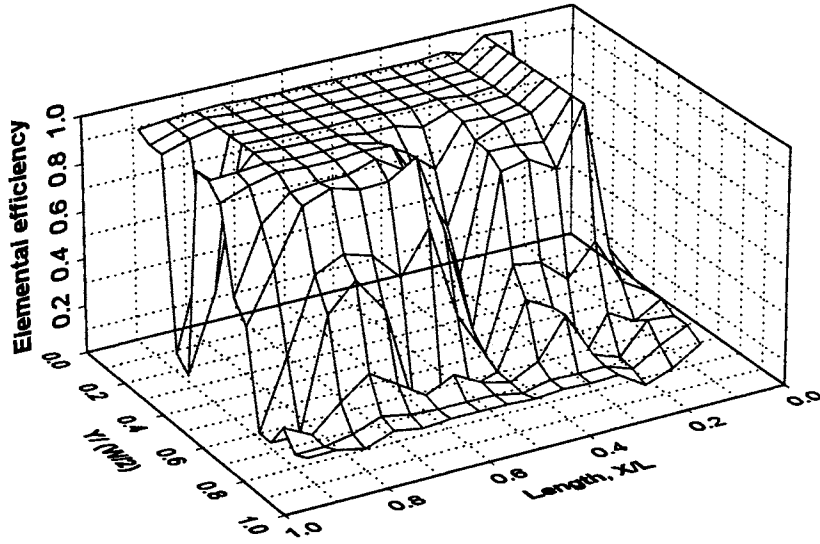


Figure 4.61: Elemental efficiency predictions for NIH model, $1 \mu\text{m}$ diameter particles (Imperfect adhesion model)

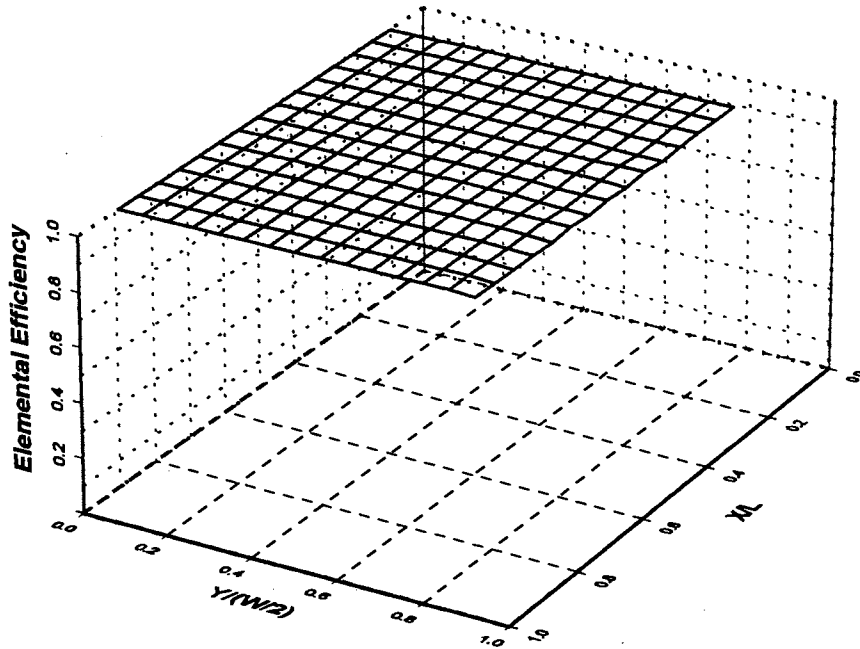


Figure 4.62: Elemental efficiency predictions for NIH model, $10 \mu\text{m}$ diameter particles (Perfect adhesion model)

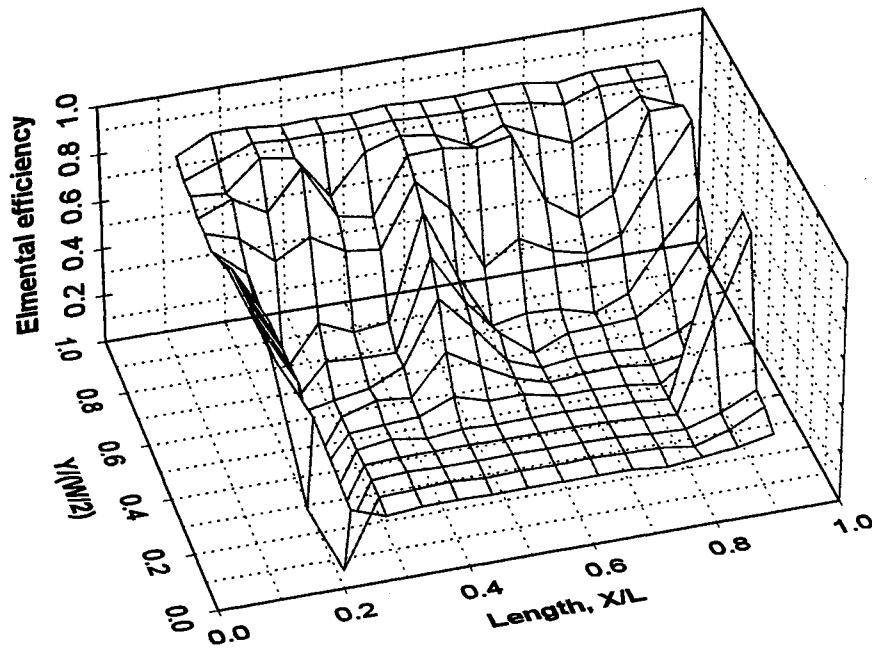


Figure 4.63: Elemental efficiency predictions for NIH model, 10 μ m diameter particles (Imperfect adhesion model)

4.8.3 Optimized tangential inlet housing (OTIH)

Figures 4.64 and 4.65 show the predictions of elemental efficiency for a small particle diameter (1 μ m). The efficiencies are nearly uniform and little higher than the other housing geometry for the same particle diameter. The effect of applying the adhesion model does not appear for small particles.

Figures 4.66 and 4.67 show the prediction of the elemental efficiency but for larger diameter particle (10 μ m). Figure 4.66 shows the perfect adhesion model. The efficiencies for perfect adhesion are very high and nearly uniform. The efficiencies for imperfect adhesion model illustrated in Figure 4.67, the efficiencies are lower than the perfect adhesion but nearly uniform.

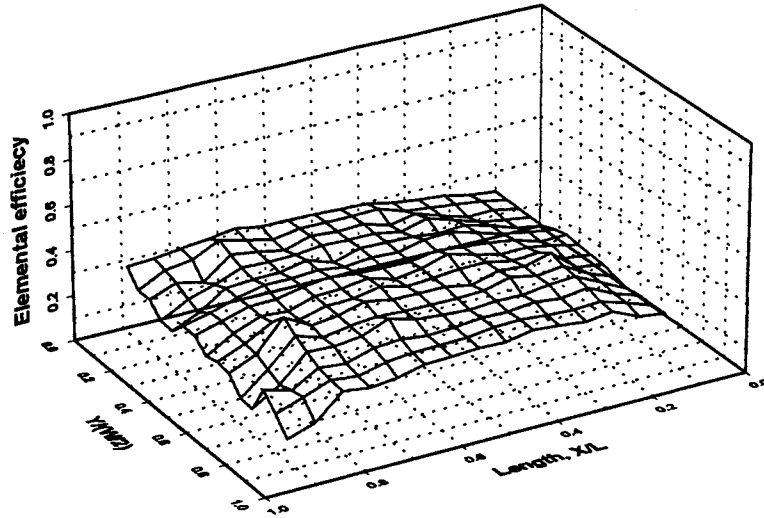


Figure 4.64: Elemental efficiency predictions for OTIH model, 1 μ m diameter particles (Perfect adhesion model)

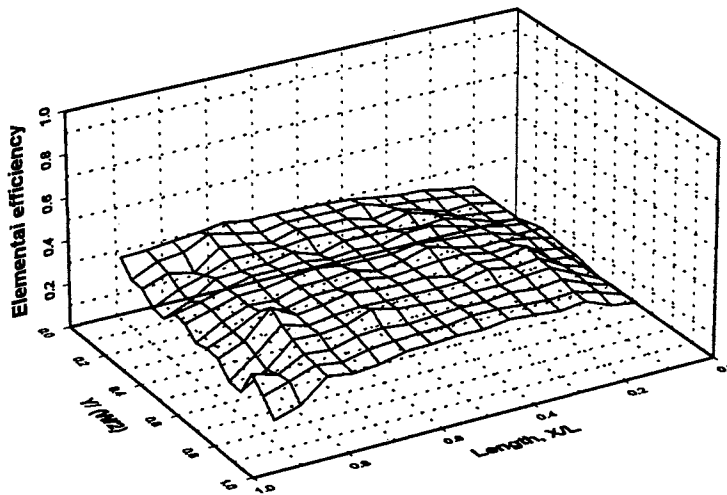


Figure 4.65: Elemental efficiency predictions for OTIH model, 1 μ m diameter particles (Imperfect adhesion model)

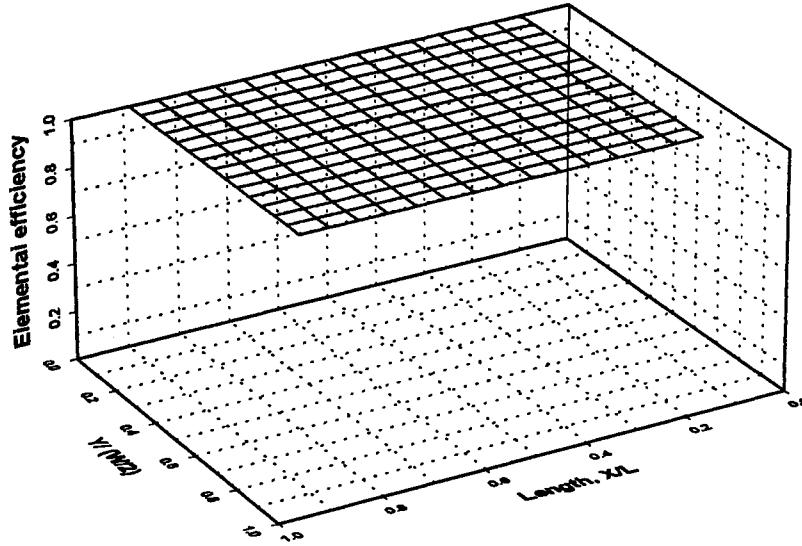


Figure 4.66: Elemental efficiency predictions for OTIH model, 10 μ m diameter particles (Perfect adhesion model)

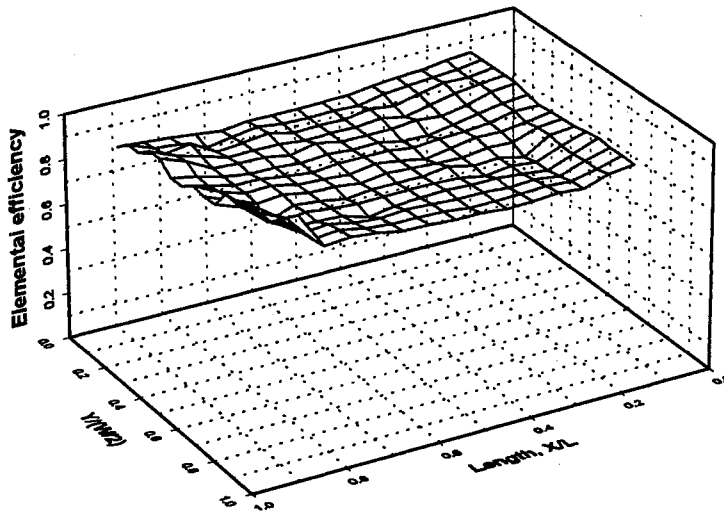


Figure 4.67: Elemental efficiency predictions for OTIH model, 10 μ m diameter particles (Imperfect adhesion model)

4.9 CALCULATED OVERALL CLEAN FILTER EFFICIENCY

The calculated filtration efficiency distributions over the projected filter surface were combined, as described previously, to provide overall efficiencies, giving an overall comparison of the effects of different test housings and velocity distributions upon filter efficiency for particular monodisperse particle diameters. Note that these calculations simply result from the application of the clean filter efficiency model using only the results of the measurements of the velocity field approaching the filter.

Recall that for these efficiency predictions we have used a single representative average fiber diameter, 38 μm , to represent the filter. Using this fiber diameter, the measured velocity upstream of the filter reduced by a 19.2:1 ratio to get the velocity inside the filter. The maximum fiber Reynolds number for the experiments is less than 2. The fiber Reynolds number is $Re_f = d_f v / \nu$, where d_f is the fiber diameter, V is the aerosol velocity, and ν is the kinematic viscosity of the air. The maximum particle Stokes number for the particle diameters considered is less than 19 for the tangential entry housing and less than 80 for the normal entry, vertical housing. These parameters are in good agreement with the limitations of the equations employed, except for the interception equation of Landahl and Herrmann (1949), which is based on a Stokes flow model of the flow field, and therefore should be limited to Reynolds numbers less than 1. The author does not believe that the somewhat higher Reynolds numbers of this study result in major errors in using this equation and believes that the trends predicted are realistic. These limitations of Reynolds number and Stokes number also are in good agreement with the Ptak and Jaroszczyk (1990) adhesion model. The results of the overall efficiency calculations for all of the cases previously discussed as well as the ideal case of perfectly uniform flow

are presented in Table 4.2. Results are presented for both perfect and imperfect adhesion. Some of these results also are shown in Figures 4.68 and 4.69 for the cases of perfect and modeled imperfect adhesion, respectively. The two sets of results for vertical, normal entry housing require explanation. The separated and recirculating flow to the sides of the entrance in this housing make efficiency predictions somewhat problematic, as some negative velocities (moving away from the filter) were measured in these regions. To provide overall efficiencies for this housing that may be compared to the efficiencies for

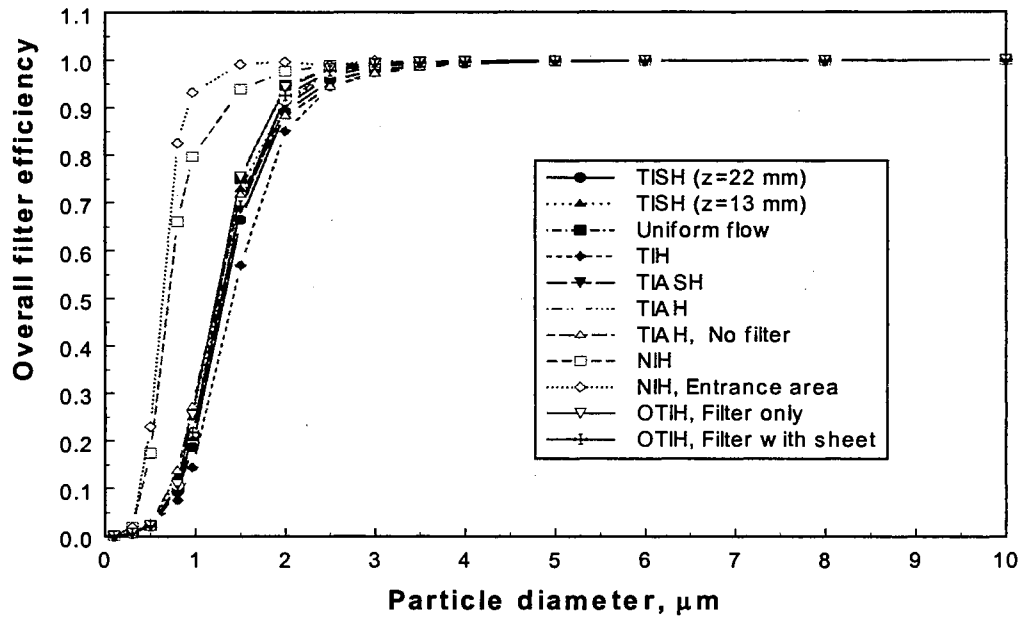


Figure 4.68: Predictions of overall filter efficiency using measured velocity distributions and perfect adhesion model

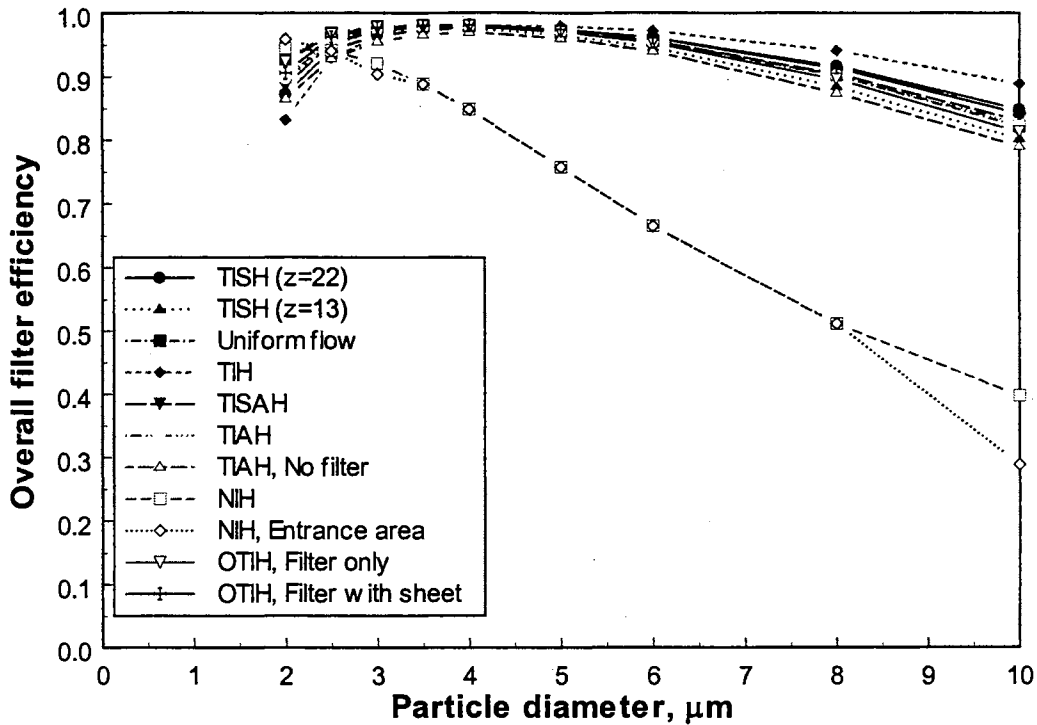


Figure 4.69: Predictions of overall filter efficiency using measured velocity distributions and imperfect adhesion model

the tangential entry housings, two approaches were taken. The first efficiency listed in the table for the vertical entry housing used the *total area* of the filter, but simply set all negative velocities to zero and assumed zero filtration efficiency at these locations. The second approach was to calculate the efficiency only for that part of the filter aligned with the entering flow, the *entrance area* approach

Note that the overall efficiencies for the larger particles all are very close to 1 with the assumption of perfect adhesion, exhibiting insignificant variations. Only the small particle efficiencies display effects of the housing geometry and flow field. With this assumption, the high centerline velocity of the normal entry housing increases the efficiencies for the small particles, for they fall on the steep slope of the Stokes number

curve of Figure 2.5. The various tangential entry housings exhibit much lower efficiencies for the small particles, as the flow is more uniform, and the peak and average velocities are not very different. Note that the nonuniform velocity distributions of the tangential entry housings can result in predicted overall efficiencies greater than those for completely uniform flows due to the difference in the velocity or the momentum of the particle. Two regions can be distinguished in the profiles modeled with perfect adhesion: First at small particle diameter the overall efficiency increases with increasing the particles momentum. Second: at large particles diameter (larger than $4 \mu\text{m}$) the efficiency stays constant as the momentum increases.

The effect of the modeled imperfect adhesion or reentrainment is visible in Figure 4.69. The effects of high momentum particle bouncing are evident for the large particles. The variation in the flow fields for the different housings produce noticeable differences in the prediction efficiencies for particles $5 \mu\text{m}$ in diameter and larger.

The much higher centerline velocities of the normal entry, vertical housing resulted in substantially reduced predictions of efficiencies for particles larger than about $3 \mu\text{m}$ with the adhesion model. The somewhat higher velocities measured in the more peaked velocity distributions for the case of the tangential inlet, angled roof housing without a filter installed also resulted in somewhat lower predicted efficiencies for the larger particles. Note that the results for particles smaller than $2 \mu\text{m}$ are not presented in the figure, for some regions of the flow result in Stokes numbers below the lower limit of the adhesion model. The modeled imperfect adhesion results included in Table 4.2 for these particles should be viewed with particular caution. In summary, three regions could be

distinguished in the graphs of imperfect adhesion (Figure 4.69) for the tangential entry housings: First, the efficiency increases as the momentum of the particle increases (appears up to 3 μm particles diameter). Second, an equilibrium region where the efficiency stays constant as the momentum of the particles increase (from 3 μm to 5 μm). Third, the efficiency decreases as the particle momentum increases and the adhesion model effect appears clearly in this region (it is the dominant part of the filtration models for the particles from 5 μm and up).

The Figures (4.68 and 4.69) suggest a tradeoff in the effect of velocity on the overall efficiency for a range of particles. It appears that with modeled imperfect adhesion, the housings with regions of higher velocity have substantially reduced efficiencies for larger particles, while efficiencies may be somewhat increased for smaller particles. These efficiency predictions make the effects of the housing geometry and velocity fields appear rather complex. The uniform velocity could be judged to be a good feature of the housing, but study of the predicted efficiencies in Table 4.2 show that this housing was not in all cases the one with the best efficiencies.

Table 4.2: Predictions of overall efficiencies for clean filter

PARTICLE DIAMETER, μm		0.5	0.8	1.0	1.5	2	3	10
CONFIGURATION	Adhesion							
TISH 13 mm	Perfect	0.025	0.124	0.250	0.730	0.914	0.986	0.999
	Imperfect	0.022	0.122	0.243	0.710	0.896	0.971	0.801
TISH 22 mm	Perfect	0.022	0.093	0.187	0.665	0.892	0.978	0.999
	Imperfect	0.022	0.092	0.183	0.646	0.873	0.965	0.849
TIH	Perfect	0.021	0.075	0.144	0.570	0.851	0.975	0.999
	Imperfect	0.020	0.074	0.142	0.555	0.833	0.963	0.889
TIASH	Perfect	0.023	0.105	0.211	0.689	0.904	0.987	0.999
	Imperfect	0.023	0.103	0.206	0.670	0.886	0.973	0.831
TIAH	Perfect	0.023	0.107	0.217	0.704	0.917	0.989	0.999
	Imperfect	0.023	0.105	0.211	0.684	0.898	0.975	0.826
TIAH (No filter)	Perfect	0.026	0.137	0.273	0.718	0.883	0.971	0.999
	Imperfect	0.026	0.134	0.265	0.699	0.866	0.955	0.789
NIH	Perfect	0.174	0.661	0.797	0.939	0.976	0.994	0.999
	Imperfect	0.168	0.632	0.769	0.914	0.945	0.921	0.398
NIH (Entrance area)	Perfect	0.230	0.815	0.932	0.991	0.996	0.998	0.999
	Imperfect	0.221	0.779	0.899	0.964	0.959	0.904	0.289
Uniform Flow	Perfect	0.022	0.102	0.211	0.751	0.947	0.992	0.999
	Imperfect	0.022	0.100	0.206	0.729	0.928	0.979	0.822
OTIH (Filter only)	Perfect	0.023	0.108	0.255	0.755	0.943	0.992	0.999
	Imperfect	0.023	0.106	0.248	0.733	0.924	0.978	0.813
OTIH (Sheet added)	Perfect	0.022	0.095	0.218	0.694	0.925	0.990	0.999
	Imperfect	0.022	0.094	0.213	0.675	0.906	0.977	0.842

CHAPTER 5

MODEL EVALUATION AND DATA VALIDATION

In this chapter different experimental verification criteria will be discussed. Statistical analysis will be performed. In this work the effort was focused on having a uniform flow above the filter so the flow uniformity criterion will be discussed first. The optimized model housing result will be used at the lowest flow rate (Laminar flow). The statistical analyses for measurement repeatability will be discussed next. The statistical analyses used in this chapter were performed at the flow rate of 212 m³/hr (125 SCFM). More details about the uncertainty in the flow rate will be discussed later.

5.1 FLOW UNIFORMITY CRITERION

The flow uniformity criterion was developed with pressure transducer pressure measurements and LDA velocity measurements. The velocity measurements were 8 mm above the surface of the filter and the pressure measurements were 6 mm above the surface of the filter. These measurements were used to represent the velocity and pressure at the surface of the filter. If the filter is modeled as a porous media one can use the Darcy's law for developing a uniformity criterion. The uniformity criterion will be studied as:

$$\frac{V}{V_{avg.}} = \frac{\Delta P_{filter} / h_i}{(\Delta P_{filter} / h_i)_{avg.}} \quad (5.1)$$

such that:

V is the normal velocity entering the filter

$V_{avg.}$ is the average of the normal velocities entering the filter

$\Delta P_{filter} / h_i$ is the normalized pressure drop across the filter

Figures 5.1 and 5.2 below show the distributions of the two sides of the flow uniformity criterion (equation 5.1). These measurements were along the centerline of the filter for cases of the filter only and the filter with an additional sheet on the top surface of the filter in the optimized housing geometry.

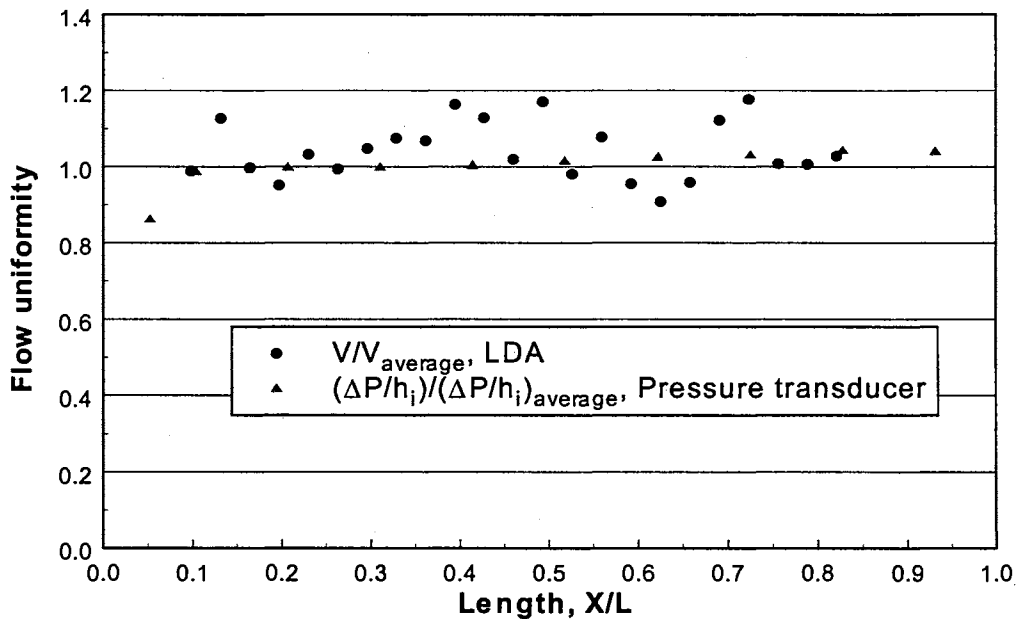


Figure 5.1: Flow uniformity criterion along the centerline of the filter
(Filter only, 14 m³/hr, Re=2,000)

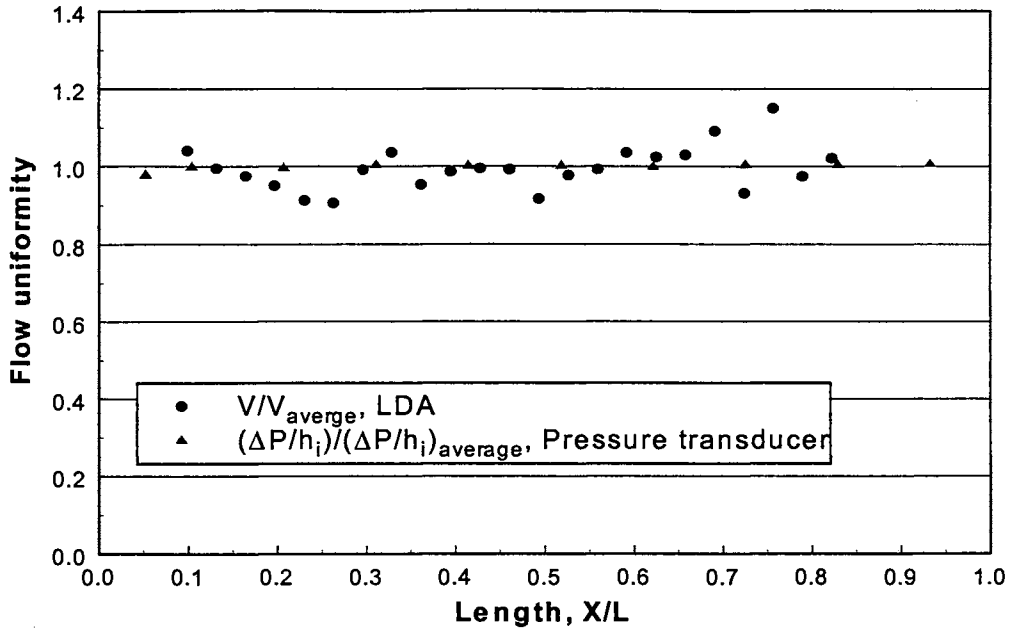


Figure 5.2: Flow uniformity criterion along the centerline of the filter
 (Filter with an additional sheet, 14 m³/hr, Re=2,000)

The deviation of $V/V_{avg.}$ from unity is the velocity deviation from the average

$$\frac{\delta V}{V_{avg.}} = \left| \frac{V}{V_{avg.}} - 1 \right| \quad (5.2)$$

The average deviation of the velocity deviations is taken as the criterion of non-uniformity

$$\text{Flow Non-Uniformity} = \left(\frac{\delta V}{V_{avg.}} \right)_{avg.} \quad (5.3)$$

Figure 5.3 below shows the distribution of the flow non-uniformity for the case of filter only along the centerline of the filter.

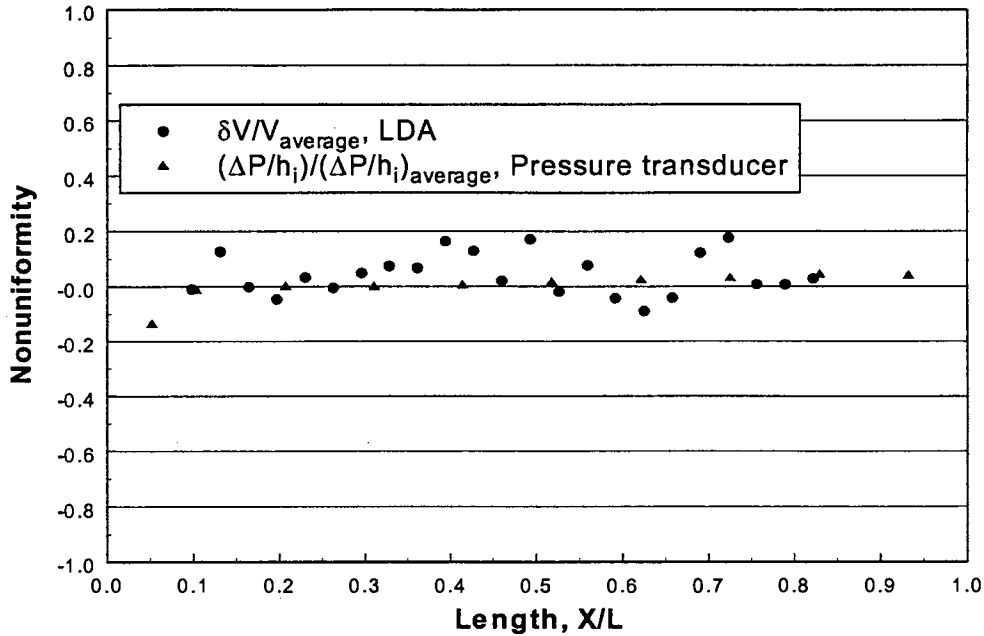


Figure 5.3: Flow non-uniformity criterion (Filter only, 14 m³/hr, Re=2,000)

For the case of filter only the flow non-uniformity was as follow:

Using equation 5.3 the flow non-uniformity = 6.5 %

But if the equivalent right hand side of equation 5.1 is used as a non-uniformity criterion the result will be as:

$$\left| \frac{\Delta P_{filter} / h_i}{(\Delta P_{filter} / h_i)_{avg}} - 1 \right|_{avg} \quad (5.4)$$

Using equation 5.4 the flow non-uniformity = 3.09 %

Figure 5.4 show the same plot as in Figure 5.3 but for the case of filter with an additional sheet.

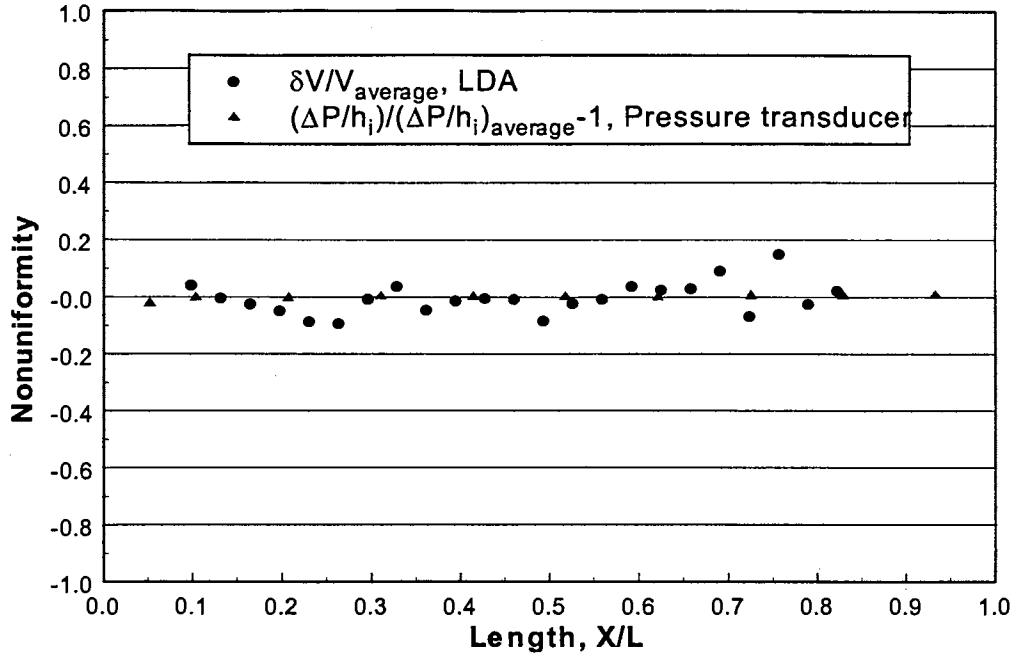


Figure 5.4: Flow non-uniformity criterion (Filter with an additional sheet, 14 m³/hr, Re=2,000)

For the case of filter with an additional sheet the flow non-uniformity was as follows:

Using equation 5.3 the flow non-uniformity = 4.249 %

Using equation 5.4 the flow non-uniformity = 0.518 %

The non-uniformity in both cases (equations 5.3 and 5.4, filter only or filter with an additional sheet) is in the range of that produced by London et al. (1968), whose results show 11.4 % of non-uniformity in a similar flow arrangement as in the present study. London's calculations was based on equation similar to equation 5.4 in the present study (the one showed smaller value of the non-uniformity based on pressure measurements) and he did not compare it with a measured velocity as in equation 5.3 in the present study (the one showed larger non-uniformity).

It seems that the flow non-uniformity is a characteristic of the housing geometry and the filter resistance itself. If the pressure drop across the filter is very large relative to the pressure changes in the housing, the influence of the flow distribution will be less than if the pressure drop across the filter is very small or in the same order of magnitude as the pressure changes in the housing. Large resistance makes the pressure distribution to be uniform, so the effect of the flow distribution will be minor. This conclusion is clear when the flow non-uniformity of the pressure transducer results are taken into consideration. Regarding the non-uniformity based on equation 5.3, which depends on the LDA velocity measurements, another factor comes to the picture is the flow rate fluctuations. The air supply we used has about $\pm 6.79 \text{ m}^3/\text{hr}$ (4 scfm) fluctuation in the flow rate at the $212 \text{ m}^3/\text{hr}$ (125 scfm). This fluctuation is about $\pm 0.32 \text{ m/s}$ in the mean inlet velocity at the housing entrance which is about 3.2% of the maximum flow rate. The lowest flow rate (laminar flow) used in the uniformity analyses has $\pm 0.85 \text{ m}^3/\text{hr}$ fluctuation. This fluctuation is about 6% of the flow rate used in this analysis. The percentage of non-uniformity with taking this fluctuation of the flow rate into account is still less than that showed by London et al. (1968).

The difference of the non-uniformity between equation 5.3 (based on LDA velocity measurements) and equation 5.4 (based on pressure measurements) might be explained due to three items.

First, the experimental uncertainty of the velocity measurements is different from that of the pressure measurements. The two measurements were not performed at the same time, so the fluctuation in the flow rate might be different in each one.

Second, the linear form of the Darcy law approximation might not be the case here. Recall that the equality of equation 5.3 and 5.4 is based on the linear form of Darcy law. The extended Darcy law with extra terms should be a better approximation of the relation between the pressure drop and the velocity in the filter.

Third, the pressure measurements were taken on the side wall of the housing (refer to Figure 3.4) at 6 mm above the surface of the filter, but the velocity measurements were taken on the centerline of the filter at about 8 mm above the surface of the filter.

Fourth, the pressure measurements duration was shorter than the velocity measurements. Pressure measurements were performed on 10 points, these might take 15 minutes to finish them. The velocity measurements were performed on 25 points, taking into consideration the time taken to fix the Digital Signal Analyzer (DSA) parameters for the LDA measurements, these might take about 50 minutes. The probability of changing the flow rate in case of the velocity measurements is much greater than that of the pressure measurements.

5.2 STATISTICAL ANALYSIS OF THE OPTIMIZATION PROGRAM RESULTS

In this section a statistical analysis will be performed on the numerical results from the optimization program. Refer to the Table D.1 in Appendix D which represents the result of the optimization technique along with some of the statistical parameters. Figure 5.5 shows the deviations of the fitted pressure distribution data from the optimum pressure distributions. The optimum pressure distribution is the pressure distribution for which the inlet plenum matches completely (100%) with the pressure distribution in the exit plenum of the model.

The magnitude of deviations of the fitted (optimized) data points from the optimum data points (both are calculated numerically by the CFD code) is shown in Figure 5.5 below. The abscissa values are the axial positions along the filter and the ordinate is the magnitude of deviations of the computed normalized pressures for the optimized housing from the ideal distributions. The beginning and the end of the filter have larger deviations than at the other points along the filter but in general the deviations of the fitted data are relatively small. The maximum percentage of deviation, about 10 % was at the beginning of the filter. The rest of the deviations are almost negligible.

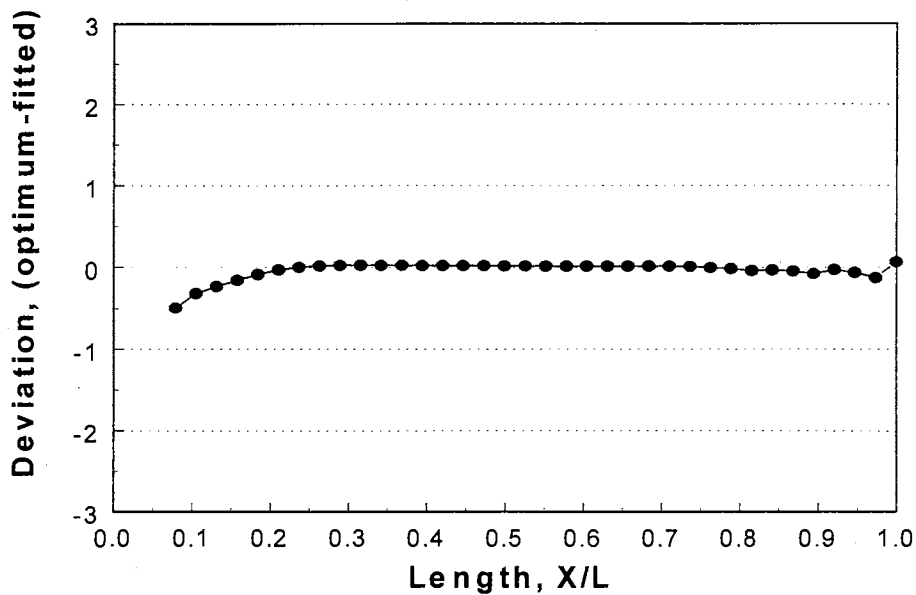


Figure 5.5: Deviations of the computed pressures for the optimized housing from the ideal pressure distributions (Numerical results)

The rest of the statistical parameters of these calculated results are as follows:

1. The root mean square of the deviations from the optimum data is $RMSE = 11.38\%$ (RMSE as in equation 2.31).

2. The average of the absolute values of the percentage of deviations AAPD =1.36% (AAPD as in equation 2.32) which is a small value.
3. The square root of the average of the absolute values of the deviations WRMS =1.17% (WRMS as in equation 2.33)

5.3 STATISTICAL ANALYSIS OF THE LDA RESULTS FOR RANDOM TESTS

Two different tests at the same flow rate ($212 \text{ m}^3/\text{hr}$) and along the centerline of the filter ($y = 0.0$ in Figure 3.7) on different days were selected for the purpose of repeatability study and statistical analysis. The repeatability results will be discussed first then the percentage of deviations and the other statistical parameters will be explained.

5.3.1 Repeatability results

Figures 5.6 and 5.7 show the repeatability results of the mean velocity at the centerline of the filter ($y = 0.0$). While the repeatability of the normal velocity looks like that of the axial velocity, the percent of deviations, presented later in this section, will give a clearer picture of the repeatability. Figures 5.8 and 5.9 show the repeatability of the fluctuation components of the velocity at the same line along the centerline of the filter.

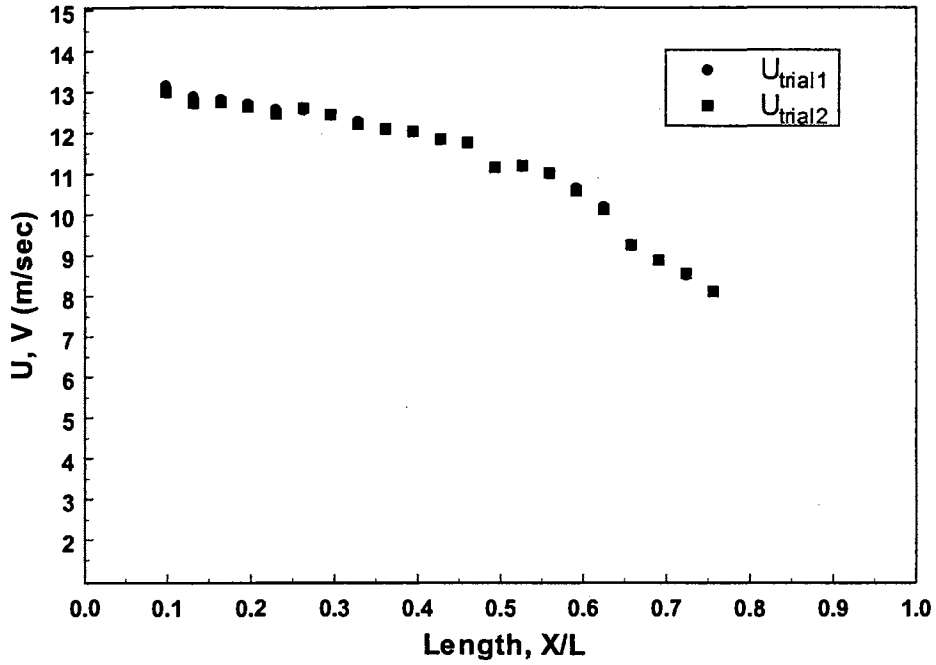


Figure 5.6: Repeatability of mean axial velocity along the centerline of filter (13 mm above filter)

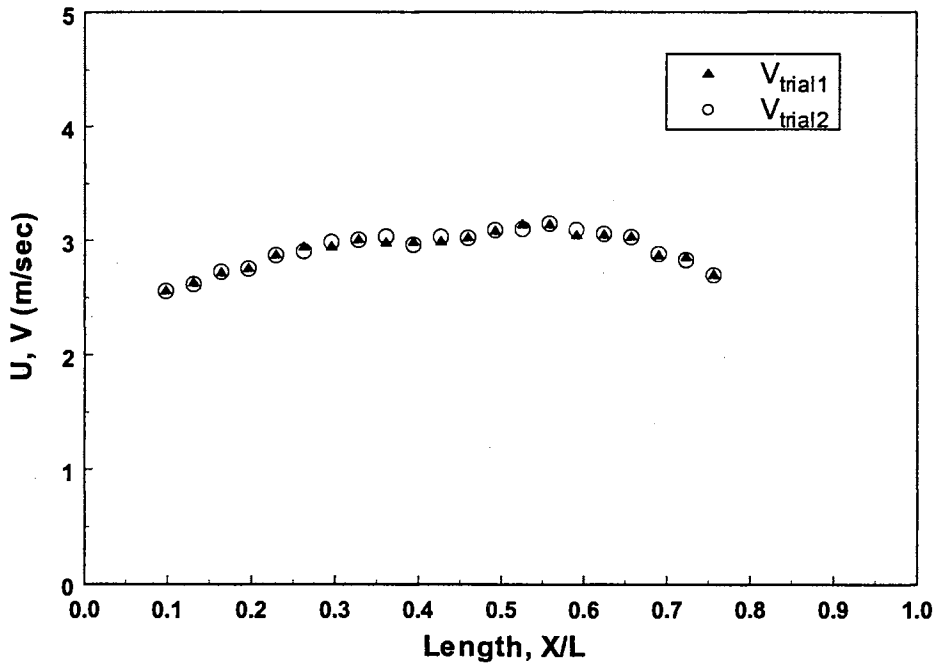


Figure 5.7: Repeatability of mean normal velocity along the centerline of filter (13 mm above filter)

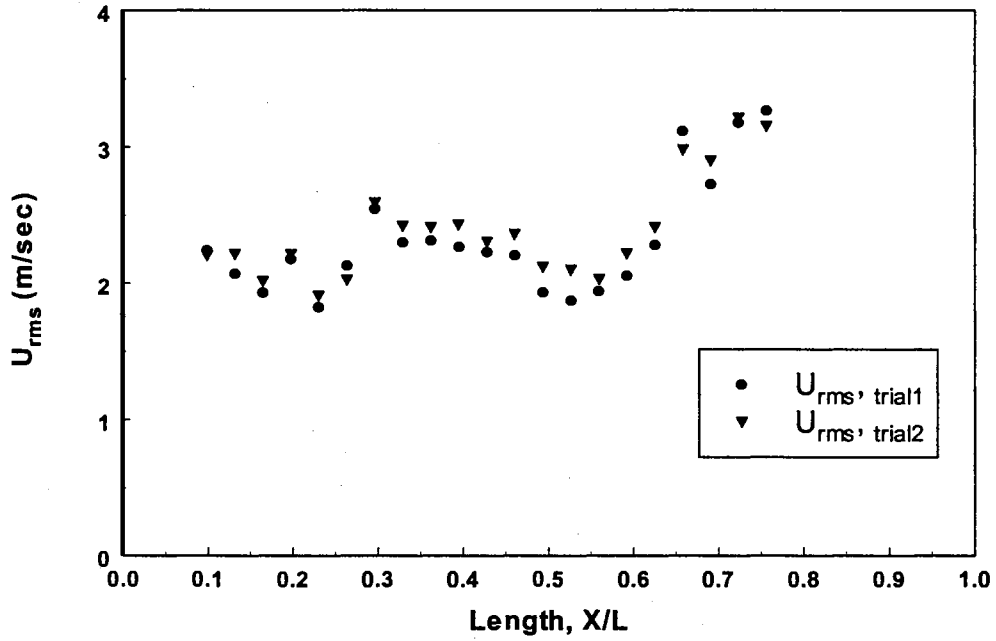


Figure 5.8: Repeatability of axial velocity fluctuating component

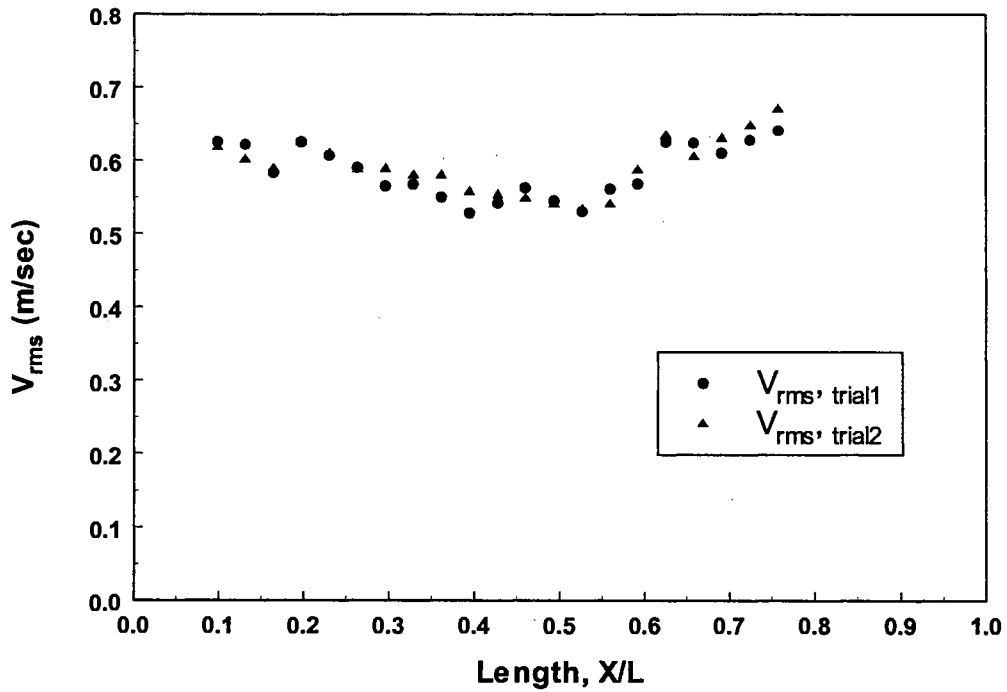


Figure 5.9: Repeatability results of fluctuating component of normal velocity

The repeatability of the mean velocity (U , V) is much better than that of the fluctuating components (U_{rms} , V_{rms}) of the velocity.

5.3.2 Percentage of deviations

The percentage of deviations of the data of trial 1 from that of trial 2 are shown in Figures 5.10 and 5.11. Figure 5.10 shows the percent of deviations of the data of trial 1 from the data of trial 2 for the axial and normal mean velocities. Figure 5.11 shows the percent of deviations for the fluctuation parts of the velocity.

From Figures 5.10 and 5.11, one can say the deviations of the normal velocity component are larger than those of the axial velocity component. This may be due to the difference in the laser power between channel 1 and 2, but this difference is very small and might be neglected. Sometimes it is hard to get very good signals in one of the channels if the power of the laser beam is very low. However, the author believes that this should not affect the results significantly, specially the mean velocities. The number of valid data points always is set to 500 points for each channel. The data acquisition is stopped when the slower of the two channels has finished acquiring the 500 samples.

One of the factors causing the deviations in the mean velocity might be the fluctuation of the flow rate. This factor is significant at low flow rates. The air flow rate through the blower fluctuates up and down about $0.85 \text{ m}^3/\text{hr}$ (0.5 scfm) at lowest flow rate case ($14 \text{ m}^3/\text{hr}$). This fluctuation of the flow rate is about 6 % of the lowest flow rate. At high flow rate case ($212 \text{ m}^3/\text{hr}$) the fluctuation was about $6.79 \text{ m}^3/\text{hr}$ (4 scfm) which is about 3.2 % of the flow rate. This fluctuation will affect the low flow rate measurements

more than the high flow rate measurements. In this analysis the high flow rate result was used for the purpose of evaluating the repeatability. The maximum percentage of deviations in the mean velocity was about 1.9%.

The percent of deviations of the fluctuation components is larger than that of the mean velocity. The maximum percent of deviation in the case of the fluctuation component was about 12.1 %. Table 5.1 below shows different statistical parameters used to understand the magnitude of the deviations in all velocity components. The maximum root mean square of the deviations (RMSE as defined in equation 2.31) was about 0.1245 and occurs in the case of the axial velocity fluctuation results. The minimum RMSE was for the normal mean velocity. The maximum average of the absolute values of the percentage of deviations (AAPD as defined in equation 2.32) was 5.15% and occurs in the case of the axial velocity fluctuation. The maximum of WRMS (the square root of the average of the absolute values of the percent of deviations, refer to equation 2.33) was about 2.27% and occurs in the case of the axial velocity fluctuation. Table 5.1 shows that the best measurements or the least uncertainty was for the mean velocity data. The uncertainty of the fluctuation component is larger than that of the mean component of the velocity.

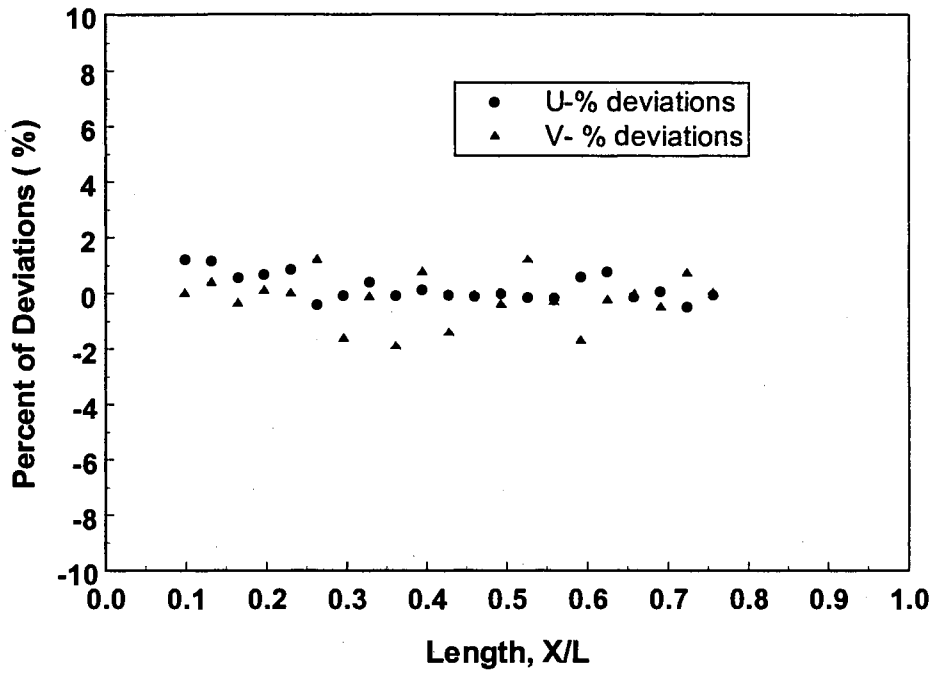


Figure 5.10: Percentage of deviations of mean velocity data

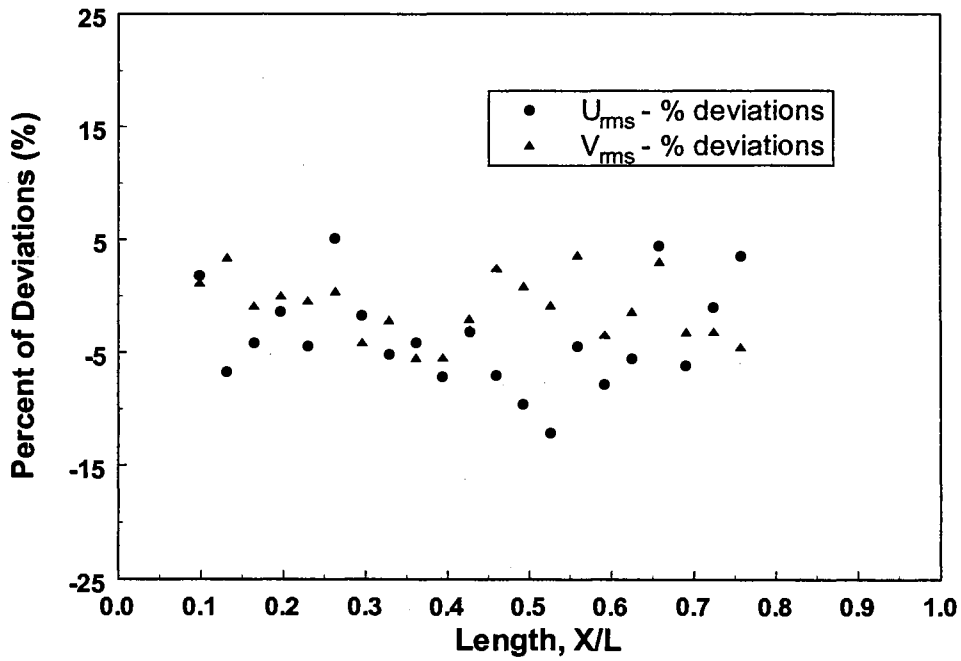


Figure 5.11: Percentage of deviations of the fluctuation component of the velocity

Table 5.1: Statistical parameters of LDA case study (212 m³/hr)

Component of velocity	RMSE (%)	AAPD (%)	WRMS (%)
Axial velocity U	6.70	0.409	0.639
Normal velocity V	2.70	0.656	0.809
Axial velocity Fluctuation	12.5	5.146	2.268
Normal velocity fluctuation	10.6	2.393	1.547

In summary the uncertainty of the fluctuation component measurements was higher than that of the mean velocity measurements.

CHAPTER 6

CONCLUSIONS AND RECOMMENDATIONS

6.1 CONCLUSIONS

The following conclusions can be drawn from the work presented:

1. For all housings, the axial and normal mean velocity distributions were not uniform.
2. For the tangential entry housings, the normal velocities displayed smaller changes with distance along the filter than the axial velocities.
3. Housings with step inlet configuration display increased normal velocities directed toward the filter near the housing entrance, suggesting more effective filtration.
4. The purely rectangular housings with tangential or step inlets displayed normal velocities directed away from the filter near the housing endwall, suggesting a vortical recirculatory flow and less effective filtration.
5. The addition of an angled upper wall to the tangential entry rectangular housings appears to suppress recirculatory flow and increase normal velocities directed toward the filter near the housing endwall.
6. The experiments show that simple changes in filter housing geometry can have significant effects on the character of the flow field and the distribution of the flow passing through the filter.
7. The optimized model housing has the most uniform flow among all housings and higher normal velocity at the endwall, suggesting more effective filtration at that area.
8. Adding the sheet to the filter makes the distribution of the pressure drop more uniform.

9. The pressure drop across the filter with the sheet added is about five times the pressure drop in the case of the filter only.
10. Based on measured pressure or velocity distributions the flow non-uniformity for the case of the filter with an additional sheet is less than that of filter only.
11. The variations of the non-dimensional pressure drop at low flow rate (laminar flow) is much higher than that at high flow rate (turbulent flow).
12. With the assumption of perfect particle adhesion, the efficiency predictions suggest nearly uniform initial filtration efficiency for particles larger than about 4 μm diameters. These efficiencies are nearly independent of the filter velocity distribution.
13. With the assumption of perfect adhesion, the overall filter efficiency for smaller particles does exhibit a dependence upon the filter velocity distribution, with regions of higher velocity tending to increase efficiency.
14. The effects of modeled imperfect adhesion significantly reduce efficiencies for particles larger than about 5 μm diameter and suggest that the housing flow field is an important factor in overall efficiency. The accuracy of the adhesion and reentrainment model correspondingly is important to the accuracy of the predictions.
15. Three regions of particle-fiber attachment in tangential entry housings may be distinguished. An increase in the collection efficiency with an increase of dust particle momentum is significant in the adhesion energy dominated region (that is, for particles up to 2.5 μm diameter). The equilibrium is reached when the adhesive energy is equal to the total energy of the dust rebound and detachment. Efficiency does not significantly change its value in this region of the filtration process (for particles from about 2.5 to 5 μm diameter). In the third region, filter efficiency decreases with increasing particle size. In this region of the filtration process more dust particles penetrate a filter with their increasing particle momentum.

6.2 RECOMMENDATIONS

The following is a listing of recommendations for future works:

1. A three-dimensional computational model should be developed. The model should be able to handle complicated geometry of the computational domain. Using finite element method, which is much better than the finite difference method in handling a complicated geometry, could do this. Turbulent flow should be better than the laminar flow solution.
2. Efficiency model could be developed that include wider range than Ptak and Jaroszczyk (1990) adhesion model. This model also could implement the effect of dust loading to provide the overall efficiency over the life of the filter.
3. Experimental measurements of filtration efficiencies should be done for different housing geometries and compared with the filtration model. This could be done using a particle counter or LDA approach.

REFERENCES

Aerometrics Inc., (1992), Doppler Signal Analyzer for Phase Doppler Particle Applications User's Manual, Sunnyvale, CA.

Al-Sarkhi, A., Yao, S., and Chambers, F. W. (1997), "Flow Distribution Dependence on the Housing Geometry for Tangential Inlet Automotive Air Filter Housing," *Advances in Filtration and Separation Technology-Advancing Filtration Solutions*, Proceeding of the Tenth Annual Meeting of the American Filtration & Separation Society, Minneapolis, MN, April 29-May 2, 1997, pp. 210-215.

Al-Sarkhi, A., Yao, S., and Chambers, F. W. (1999), "Effect of Vehicular Air Filter Housing Configuration and Filter Resistance on Filter Flow Distributions and Filtration," SAE International Congress and Exposition, Detroit, MI, March 1-4, 1999, SAE Technical Paper 1999-01-0007.

Araya R., Modi, V. (1988), "A New Algorithm for Inverse Design of Flow Headers," 1988 ASME Design Technology Conference-the Design Automation Conference, Kissimmee, Florida, September 25-28, 1988, Vol. 14, pp. 333-336.

Bokar, J. C., Ozisik, M. N. (1995), "An Inverse Analysis for Estimating the Time-Varying Inlet Temperature in Laminar Flow Inside a Parallel Plate Duct," *International Journal of Heat and Mass Transfer*, Vol. 38, No. 1, pp. 39-49.

Bradshaw, P., Cebeci, T., and Whitelaw, J., *Engineering Calculation Methods for Turbulent Flow*, Academic Press, New York, 1981.

Brown, R. C. (1993), *Air Filtration: An Integrated Approach to the Theory and Applications of Fibrous Filters*, Pergamon Press, Oxford.

Cabuk, H., and Modi, V., (1989), "On the Design of Optimum Flow Headers for Heat Exchangers," American Society of Mechanical Engineers, *1989 National Heat Transfer Conference*, Philadelphia, PA, Vol. 108, pp. 161-167.

Chandler, J. P., Hill, D. E. and Spivey, H. Q. (1972), "A Program for Efficient Integration of Rate Equations and Least Square Fitting of Chemical Reaction Data," *Computer and Biomedical Research*, Vol. 5, pp.515-534.

Chaviaropoulos, P., Dedoussis, V. and Papailiou, K. D. (1995), "On the 3-D Inverse Potential Target Pressure Problem, Part1. Theoretical Aspects and Method Formulation," *Journal of Fluid Mechanics*, Vol. 282, pp. 131-146.

- Chen, D.-R., Pui, D.Y.H., and Liu, B.Y.H. (1993), "Numerical Study and Optimization of Pleated Gas Filters," *Proceedings - Institute of Environmental Sciences Annual Technical Meeting*, pp. 414-422.
- Chen, F. and Chen, C. (1992), "Convection in Superposed Fluid and Porous Layers," *Journal of Fluid Mechanics*, Vol. 234, pp. 97-119.
- Crawford, M. (1976), *Air Pollution Control Theory*, McGraw Hill, New York, NY.
- Dedoussis, V., Chaviaropoulos and Papailiou, K. D., (1992), "A 3-D Inverse Methodology Applied to the Design of Axisymmetric Ducts," ASME paper 92-GT-290.
- Dedoussis, V., Chaviaropoulos and Papailiou, K. D. (1993), "Rotational Compressible Inverse Design Method for Two-Dimensional Internal Flow Configurations," *AIAA Journal*, Vol. 31, No.3, pp. 551-558.
- Dedoussis, V., Chaviaropoulos & Papailiou, K. D. (1995), "On the 3- D Inverse Potential Target Pressure Problem, Part2. Numerical Aspects and Application to Duct Design, " *Journal of Fluid Mechanics* , Vol. 282, pp. 147-162.
- Delery, J. M. and Formery, M. J. (1983), "A Finite Difference Method for Inverse Solution of 3-D Turbulent Boundary Layer Flow," *AIAA paper* 83-0301.
- Duran, R. (1995), "Improvement of Flow Uniformity and Modeling of Filtration Efficiencies for Automotive Air Filter Test Housings," M.S. Thesis, School of Mechanical and Aerospace Engineering, Oklahoma State University, Stillwater, OK.
- El-Mistikawy, T. M. (1994), "Solution of Keller Box Equations for Direct and Inverse Boundary-Layer Problems," *AIAA Journal*, Vol. 32, No. 7, pp. 1538 - 1550.
- Flagan, R. C., and Seinfeld J. H., (1988), *Fundamentals of Air Pollution Engineering*, Prentice Hall Englewood, NJ.
- First, M.W., and Hinds, W.C. (1976), "High Velocity Filtration of Submicron Aerosols," *Journal of the Air Pollution Control Association*, Vol. 26, No. 2, pp. 119-123.
- Freshwater, D. C., and Stenhouse, J. I. T. (1972), "The Retention of Large Particles in Fibrous Filters," *American Institute of Chemical Engineering Journal*, Vol. 18, No. 4, pp. 786-791.
- Georgiadis, J. and Catton, I. (1986), "Prandtl Number Effect on Benard Convection in Porous Media," *Journal of Heat Transfer*, Vol. 108, pp. 284-290.
- Gurumoorthy, V., Bawabe, A.J., Brown, G.A., and Lessman, R.C. (1990), "Prediction of Pressure Drop Performance in Automotive Air Induction Systems," *Proceedings of the Third Annual Meeting of the American Filtration Society*, Washington, D.C.

Grant, D. C., Liu, B. Y. and Fisher, W. (1988), "Particle Capture Mechanisms in Gases and Liquids: An Analysis of Operative Mechanisms in Membrane/Fibrous Filters," *The Journal of Environmental Science*, Vol. 31-32, pp. 43-51.

Heyda, J. F. (1960), "An Analytical Study of a Balanced Reverse Folded Flow," General Electric Company Report XDC 60-1-158, reprinted by Department of Commerce.

Hirt, C., Nichols, B., and Romero, N. (1975), "SOLA- a Numerical Solution Algorithm for Transient Fluid Flow," Los Alamos Scientific Laboratory Report LA-5852, April.

Hsun, H., and Cebeci, T. (1991), "Bordering Algorithm for Solution of Boundary-Layer Equations in Inverse Mode," *AIAA Journal*, Vol. 29, No. 12.

Jackson, L. W. (1978), "A Comparison of Selected Gradient Methods for Solving Nonlinear Least Square Problems," M. S. Thesis, Computer Science Department, Oklahoma State University, Stillwater, OK.

Jaroszcyk, T. and Wake, J. (1991), "Critical Aerosol Velocity in Nonwoven Filtration," *TAPPI Proceedings, Nonwoven Conference*, pp. 125-135.

Kuwabara, S. (1959), "The Forces Experienced by Randomly Distributed Parallel Circular Cylinders or Spheres in a Viscous Flow at Small Reynolds Numbers," *Journal of the Physical Society of Japan*, Vol. 14, pp. 527-532.

Landahl, H.D. and Herrmann, R. G. (1949), "Sampling of Liquid Aerosols by Wires, Cylinders, and Slides, and the Efficiency of Impaction of the Droplets," *Journal of Colloid Science*, Vol. 4, pp. 103-136.

Lee, K.W. and Liu, B.Y.H. (1982a), "Theoretical Study of Aerosol Filtration by Fibrous Filters," *Aerosol Science and Technology*, Vol. 1, pp. 147-161.

Lee, K. W. and Liu, B. Y. H. (1982b), "Experimental Study of Aerosol Filtration by Fibrous Filters," *Aerosol Science and Technology*, Vol. 1, Elsevier Science Publication Co., Amsterdam, pp. 35-46.

Lilley, D. (1992), "Computational Fluid Dynamics," Course notes, Oklahoma State University, Stillwater, OK.

Liu, F. B. and Ozisik, M. N. (1996), "Inverse Analysis of Transient Turbulent Forced Convection Inside Parallel Plate Ducts," *International Journal of Heat and Mass Transfer*, Vol. 39, No. 12, pp. 2615 -2618.

Liu, G., Tebbutt, C.B., Duran, R. and Chambers, F.W. (1996), "Filter Inlet Velocity Redistribution with Filter Loading," *Particulate Science and Technology*, Vol. 14, No. 3, pp. 279-291.

- Liu, G. (1994), "Velocity Measurements and CFD Predictions of Flow Redistribution Through Air Filter," Master Thesis, Oklahoma State University, Stillwater, OK.
- London, A. L., Klopfer, G. and Wolf, S. (1968), "Oblique Flow Headers for Heat Exchangers," *Journal of Engineering for Power*, pp. 271-286.
- London, A. L. and Kays, W. M. (1984), *Compact Heat Exchangers*, McGraw-Hill, third edition, NY.
- Marquardt, D. W. (1963), "An Algorithm for Least-Squares Estimation of Nonlinear Parameters," *Journal of the Society for Industrial and Applied Mathematics*, Vol. 11, No. 2, pp. 431-441.
- Newman, R. A., Duran, R., and Chambers, F.W., (1997), "Air Filter Test Housing Velocity Profile Effects on Filter Efficiencies," *Topics in Automotive Filtration Design*, Society of Automotive Engineers, Warrendale, Pennsylvania, pp. 35-48. (SAE Paper 970554)
- Newman, R. A. (1994), "Uniformity of Air Flow in Automotive Test Housings and Its Effects on the Efficiency of Fibrous Filters," M.S. Thesis, School of Mechanical and Aerospace Engineering, Oklahoma State University, Stillwater, Oklahoma.
- Pandolfi, M., and Zannatti, L. (1978), "Some Permeable Boundaries in Multidimensional Flows," *6th International Conference on Numerical Methods in Fluid Dynamics*, Tbilisi, Georgia, pp. 225-262.
- Poon, Wai, S., and Liu, B. Y. H. (1997) "Fractional Efficiency and Particle Mass Loading Characteristics of Engine Air Filters," SAE Technical Paper No. 970673, *Topics in Automotive Filtration Design (SP-1252)* SAE, Inc., Warrendale, PA, pp. 103-112.
- Poon, Wai, S., and Liu, B. Y. H. (1997) "A Bimodal Loading Test for Engine and General Purpose Air Cleaning Filters," SAE Technical Paper No. 970674, *Topics in Automotive Filtration Design (SP-1252)* SAE, Inc., Warrendale, PA, pp. 113-116.
- Ptak, T., and Jaroszczyk, T. (1990), "Theoretical-Experimental Aerosol Filtration Model for Fibrous Filters at Intermediate Reynolds Numbers," *Proceedings of the Fifth World Filtration Congress*, Nice, France, pp. 566-572.
- Radwan, S. F. and Lekoudis, S. G. (1984), "Boundary Layer Calculations in the Inverse Mode for Incompressible Flows Over Infinite Swept Wings," *AIAA Journal*, Vol. 22, No. 6, pp.737-743.
- Radwan, S. F. and Lekoudis, S. G. (1986), "Inverse Mode Calculations of the Incompressible Turbulent Boundary Layer on an Ellipsoid," *AIAA Journal*, Vol. 24, No. 10, pp. 1628-1635.

Roache, P., Mueller, T. (1970), "Numerical Solutions of Laminar Separated Flows," *AIAA Journal*, Vol. 8, No.3, pp. 530-538.

Sabnis, R.D., Cai, Q., and Chambers, F.W. (1994), "Diagnosis of the Flow Fields in a Housing for Air Filter Performance Testing," American Institute of Aeronautics and Astronautics Paper AIAA-94-0117.

Sabnis, R.D., Cai, Q., and Chambers, F.W. (1994), "Flow Distribution Effects Upon Air Filter Performance Measurements," *SAE 1994 Transactions, Journal of Engines*, Society of Automotive Engineers, Warrendale, Pennsylvania, Section 3, pp. 386-397. (Also: 1994, *Climate Control and Automotive Cabin Air Filtration*, SAE SP-1040, pp. 1-12, and SAE Paper 940317.

Sandborn, V. A and Liu, C., Y. (1968), "On Turbulent Boundary Layer Separation," *Journal of Fluid Mechanics*, Vol.32, pp. 293 -304.

Schlichting, H. (1979), *Boundary Layer Theory*, McGraw-Hill, New York, 7th ed.

Selig, M. S. and Maughmer M., D. (1992), "Generalized Multipoint Inverse Airfoil Design," *AIAA Journal*, Vol. 30, No. 11, pp. 2618 - 2625.

Stanitz, J. D. (1953), "Design of Two-Dimensional Channels With Prescribed Velocity Distributions Along the Channel Walls," *NACA Rept.* 1115.

Stanitz, J. D. (1988), "A Review of Certain Inverse Methods for the Design of Ducts with 2 - or 3 -Dimensional Flow," *Applied Mechanics Review*, Vol. 41, No. 6, pp. 217-238.

Stanitz, J. D. (1980), "General Design Method for Three-Dimensional Potential Flow Fields. I - Theory," *NASA CR 3288*.

Stanitz, J. D. (1985), "General Design Method for Three-Dimensional Potential Flow Fields. II - Computer program Din3D1 for Simple, Unbranched Ducts," *NASA CR 3926*.

Suneja, S. K, and Lee, C. H. (1974), "Aerosol Filtration by Fibrous Filters at Intermediate Reynolds Number (≤ 100)," *Atmospheric Environment*, Vol. 8, pp. 1081-1094.

White. F. M. (1974), *Viscous Fluid Flow*, McGraw-Hill, New York.

Zannetti, L. (1980), "Time Dependent Method to Solve Inverse Problems for Internal Flows," *AIAA Journal*, Vol. 18, No. 7, pp. 754 - 758.

APPENDICES

APPENDIX A: Axial Velocity Distributions

APPENDIX B: Normal Velocity Fluctuations

APPENDIX C: Optimization program results

APPENDIX D: Pressure distribution results

APPENDIX E: Mean velocity distribution at different height

APPENDIX F: Comparison of two optimized profiles

APPENDIX A

Axial mean velocity distribution in different housings are presented here. These measurements were performed at flow rate of 212 m³/hr.

- TISH: Tangential Inlet Housing with Step
- TIAH: Tangential Inlet Housing with Angled wall
- TIASH: Tangential Inlet Housing with Step and Angled wall
- OTIH: Optimized Tangential Inlet Housing resulting from the optimization program

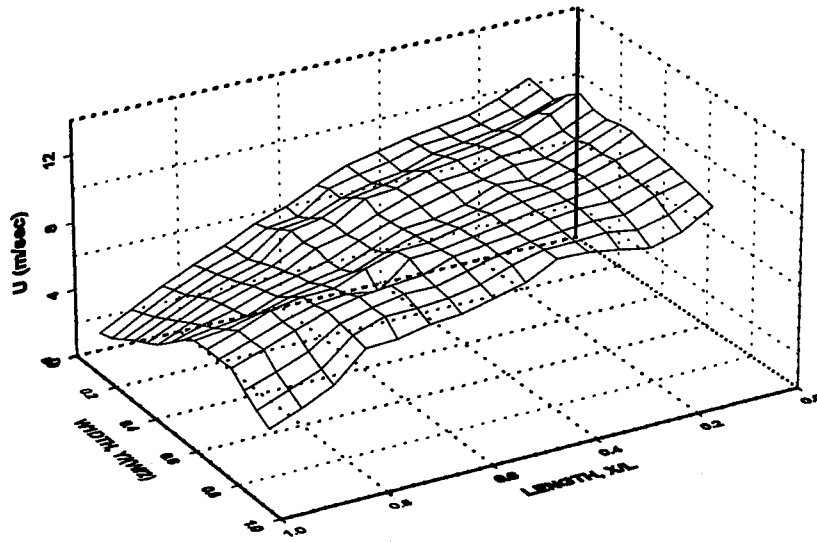


Figure A.1: Axial velocity distributions in TISH model 22 mm above filter (filter only)

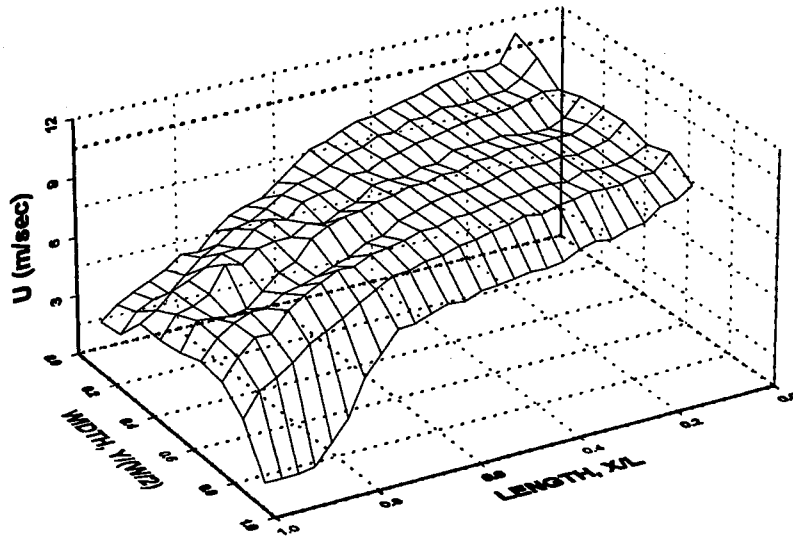


Figure A.2: Axial velocity distributions in TISH model 13 mm above filter (filter only)

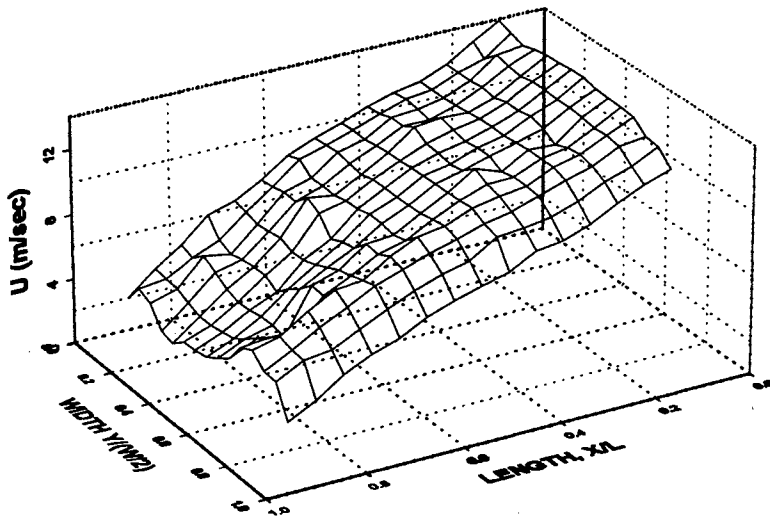


Figure A.3: Axial velocity distribution in TIAH model 13 mm above filter

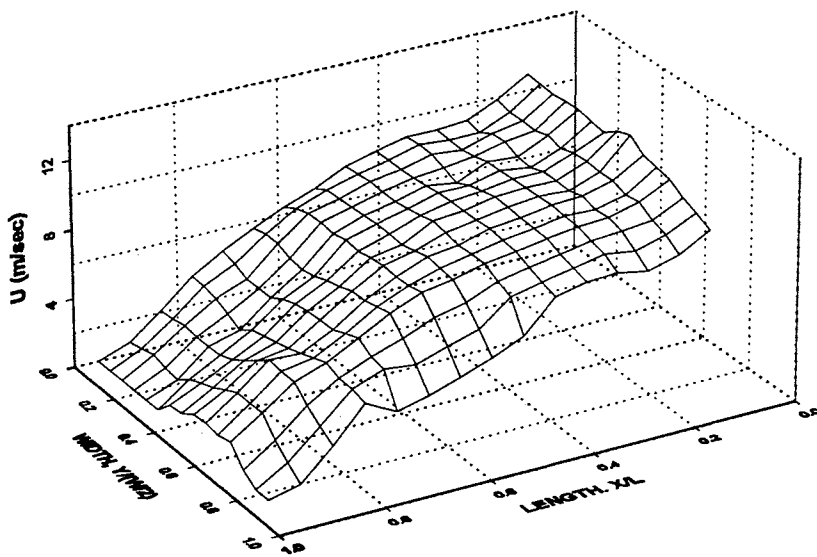


Figure A.4: Axial velocity distribution in TIASH 13 mm above filter

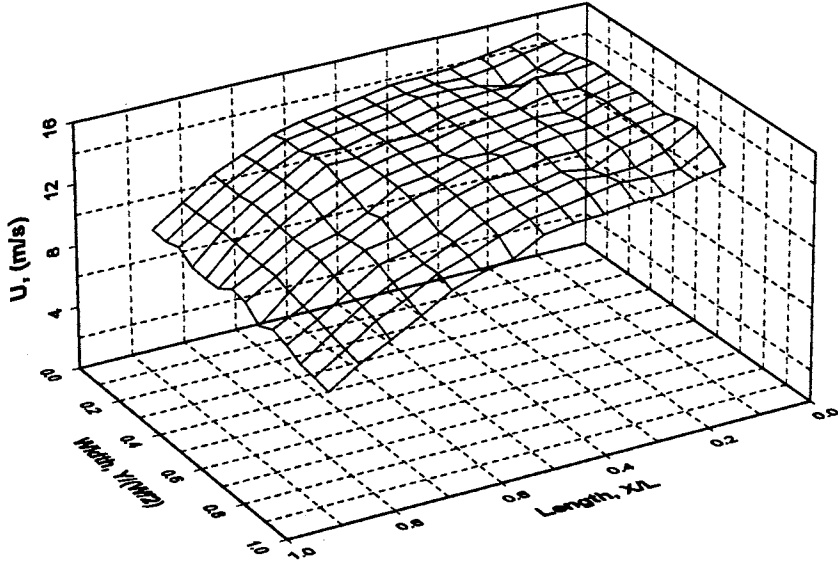


Figure A.5: Axial velocity distributions in OTIH model 8 mm above filter (filter only)

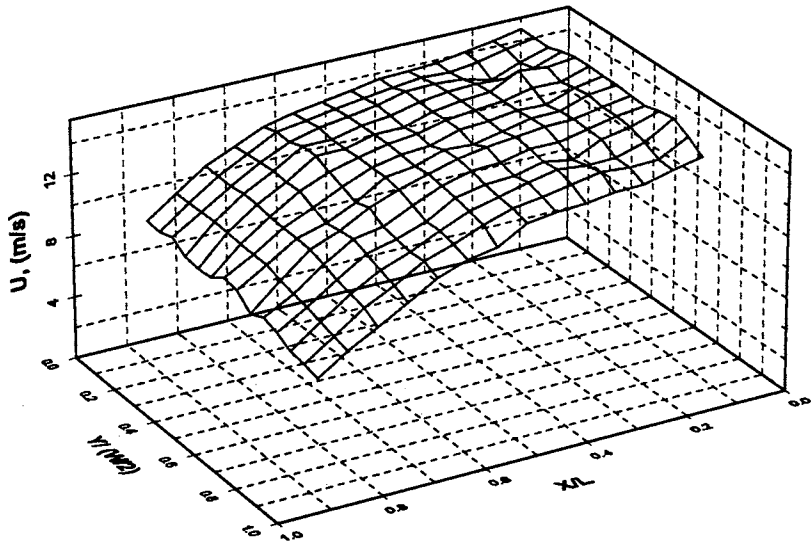


Figure A.6: Axial velocity distribution in OTIH model housing 8 mm above (filter with an additional sheet)

APPENDIX B

Normal velocity fluctuation results in different housings are presented here. These measurements were performed at a flow rate of 212 m³/hr.

- TISH: Tangential Inlet Housing with Step
- TIASH: Tangential Inlet Housing with Step and Angled wall
- TIAH: Tangential Inlet Housing with Angled wall
- OTIH: Optimized Tangential Inlet Housing resulting from the optimization program

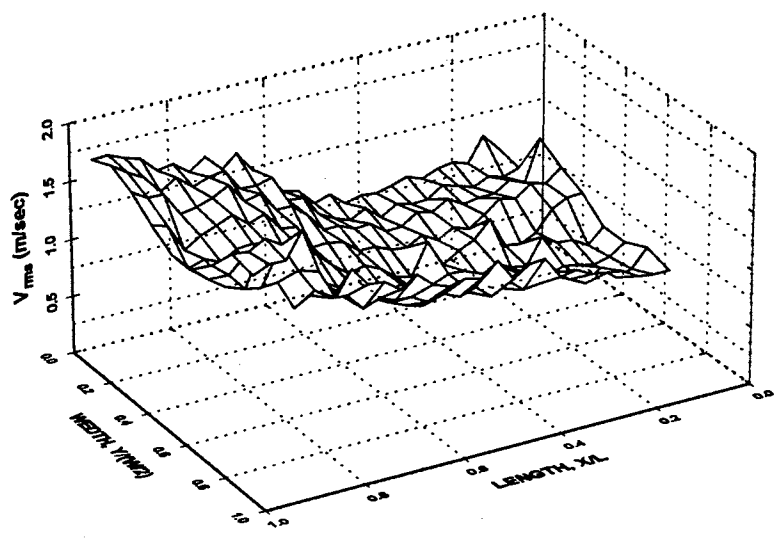


Figure B.1: Normal velocity fluctuations in TISH model 13 mm above filter

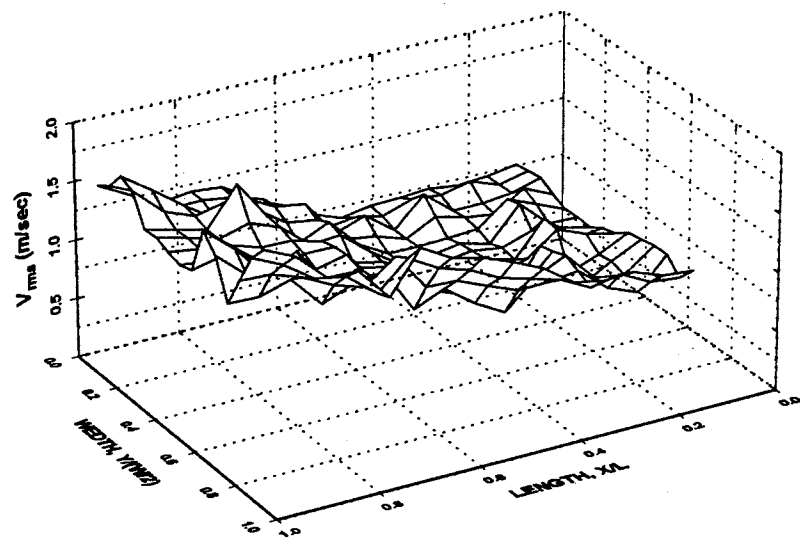


Figure B.2: Normal velocity fluctuations in TIASH model 13 mm above filter

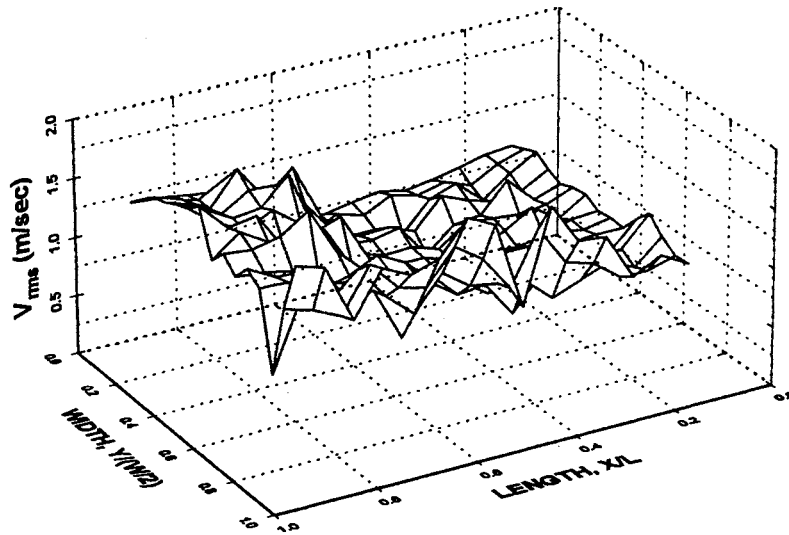


Figure B.3: Normal velocity fluctuations in (TIAH) model, 13 mm above filter

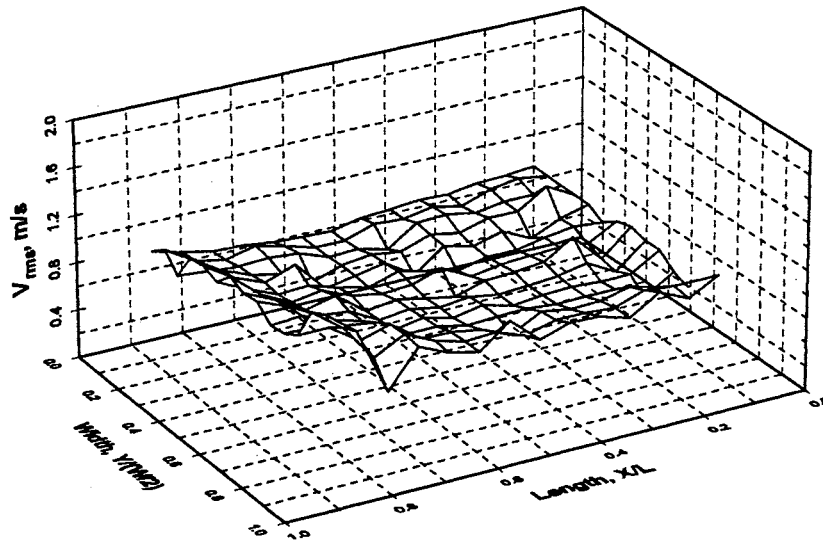


Figure B.4: Normal velocity fluctuations in OTIH model 8 mm above filter (filter only)

APPENDIX C

Optimization program results are presented in the present appendix. The first two columns are the point number and the axial grid point number in the solution domain (on the length of the filter direction). The third column is the optimum pressure that the code is trying to reach (the pressure that perfectly matches with the exit pressure distribution). The fourth column is the optimized pressure (the pressure that the optimization routine has iteratively reached at the end of the iteration process). The rest are the statistical parameters that are explained in chapter 2.

Table C.1: Optimization program output results

DATA	X(I)	Y(I)	FIT(I)	DEV	% DEV	WDEV	W(I)
No.	Axial Position	Optimum Pressure	Optimized Pressure	Deviation	Percent Deviation	Weighted Deviation	Weight
1	3.00	4.769	4.277	-.4920	-10.32	-.1032	4.769
2	4.00	4.765	4.451	-.3144	-6.598	-.0660	4.765
3	5.00	4.759	4.532	-.2275	-4.780	-.0478	4.759
4	6.00	4.752	4.602	-.1502	-3.161	-.0316	4.752
5	7.00	4.744	4.663	-.0807	-1.701	-.0170	4.744
6	8.00	4.733	4.706	-.0269	-.5691	-.0057	4.733
7	9.00	4.722	4.727	.0050	.1066	.0011	4.722
8	10.0	4.708	4.729	.0218	.4635	.0046	4.708
9	11.0	4.693	4.721	.0278	.5934	.0059	4.693
10	12.0	4.676	4.705	.0289	.6170	.0062	4.676
11	13.0	4.657	4.685	.0282	.6062	.0061	4.657
12	14.0	4.637	4.663	.0264	.5694	.0057	4.637
13	15.0	4.615	4.640	.0253	.5479	.0055	4.615
14	16.0	4.592	4.616	.0239	.5210	.0052	4.592
15	17.0	4.566	4.590	.0242	.5302	.0053	4.566
16	18.0	4.539	4.563	.0236	.5205	.0052	4.539
17	19.0	4.511	4.533	.0220	.4886	.0049	4.511
18	20.0	4.481	4.502	.0207	.4613	.0046	4.481
19	21.0	4.449	4.468	.0193	.4332	.0043	4.449
20	22.0	4.415	4.434	.0188	.4260	.0043	4.415
21	23.0	4.379	4.398	.0193	.4411	.0044	4.379
22	24.0	4.342	4.360	.0183	.4211	.0042	4.342
23	25.0	4.304	4.322	.0178	.4141	.0041	4.304
24	26.0	4.263	4.281	.0179	.4197	.0042	4.263
25	27.0	4.221	4.236	.0148	.3495	.0035	4.221
26	28.0	4.177	4.189	.0116	.2787	.0028	4.177
27	29.0	4.132	4.134	.0016	.0386	.0004	4.132
28	30.0	4.085	4.071	-.0144	-.3521	-.0035	4.085
29	31.0	4.036	3.999	-.0372	-.9208	-.0092	4.036
30	32.0	3.985	3.956	-.0295	-.7415	-.0074	3.985
31	33.0	3.932	3.888	-.0437	-1.110	-.0111	3.932
32	34.0	3.878	3.803	-.0753	-1.943	-.0194	3.878
33	35.0	3.822	3.796	-.0258	-.6757	-.0068	3.822
34	36.0	3.764	3.703	-.0614	-1.632	-.0163	3.764
35	37.0	3.703	3.579	-.1240	-3.349	-.0335	3.703
36	38.0	3.640	3.708	.0681	1.870	.0187	3.640

APPENDIX D

The pressure distributions in the inlet and exit plenum are shown in this appendix. These are the dimensional forms of the normalized results presented in chapter 4. These measurements were performed on a plane 6 mm above and 6 mm below the filter using the pressure transducer.

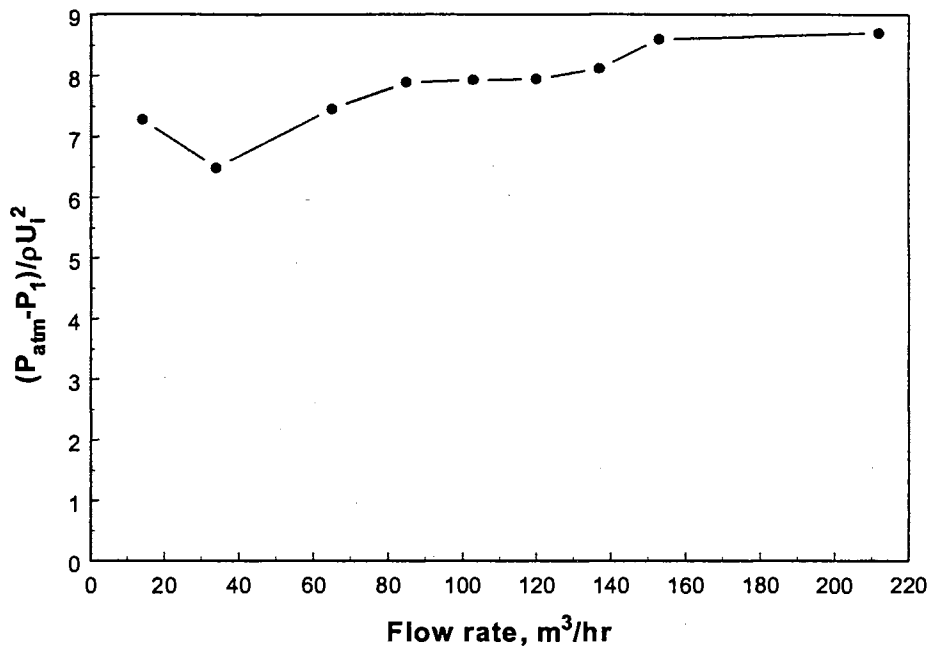


Figure D.1: Normalized pressure drop: ambient to port 1 (inlet plenum, filter only)

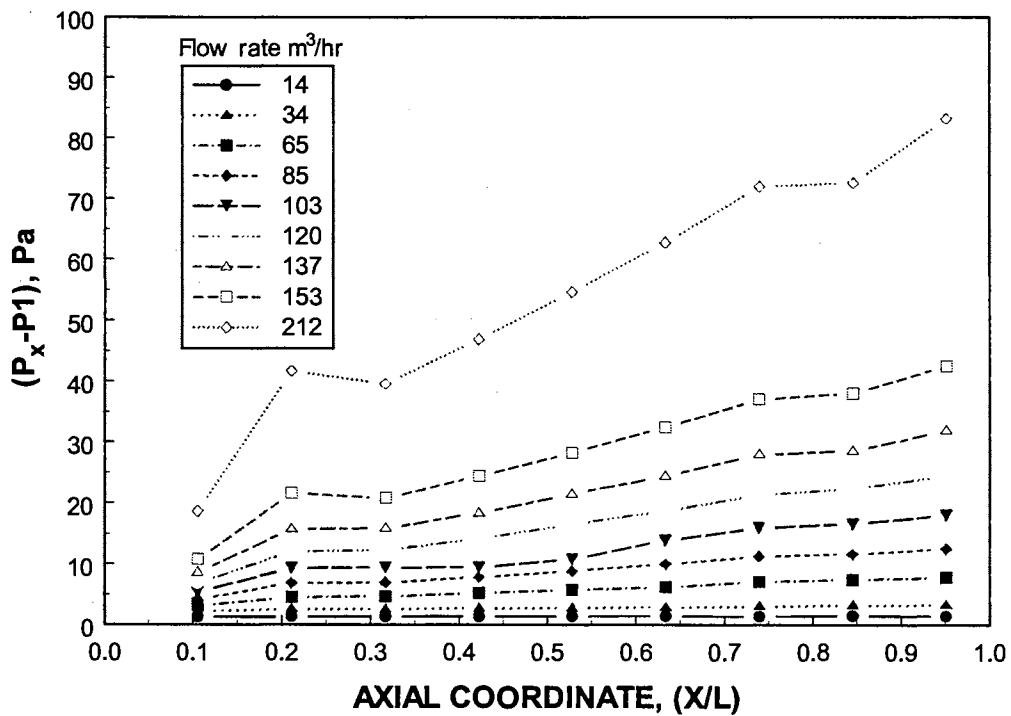


Figure D.2: Pressure distributions in inlet plenum along the filter (filter only)

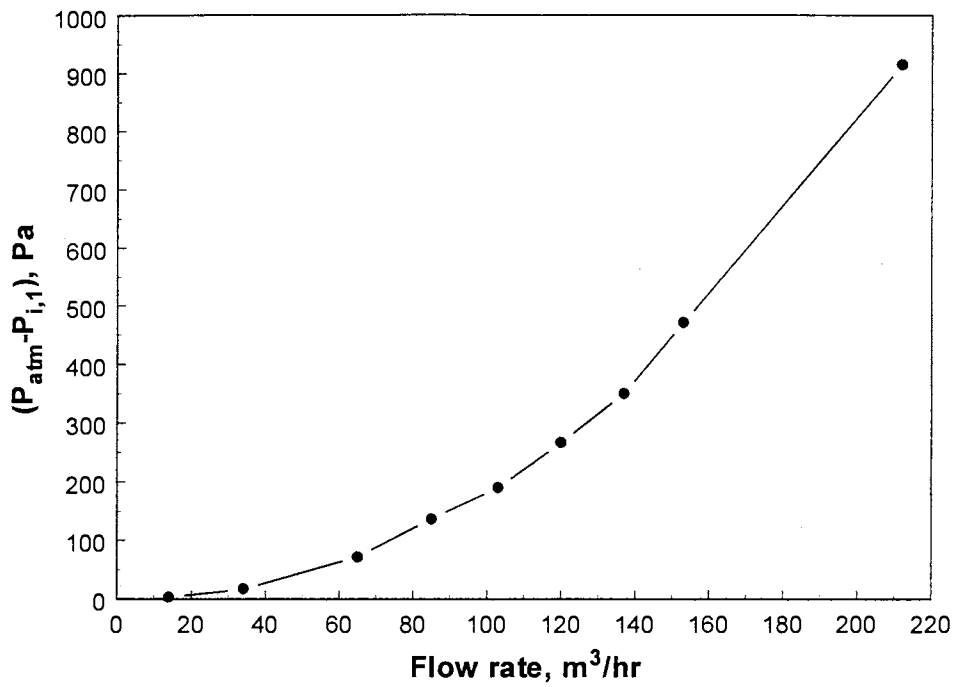


Figure D.3: Pressure drop: ambient to port 1 (filter with an additional sheet)

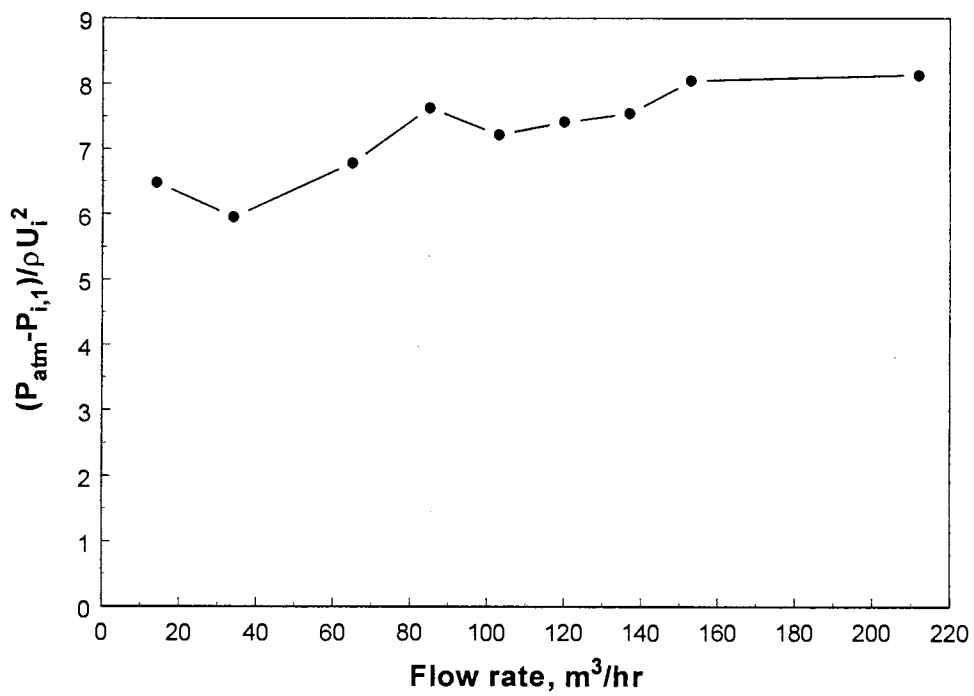


Figure D.4: Normalized pressure drop: ambient to port 1 (filter with an additional sheet)

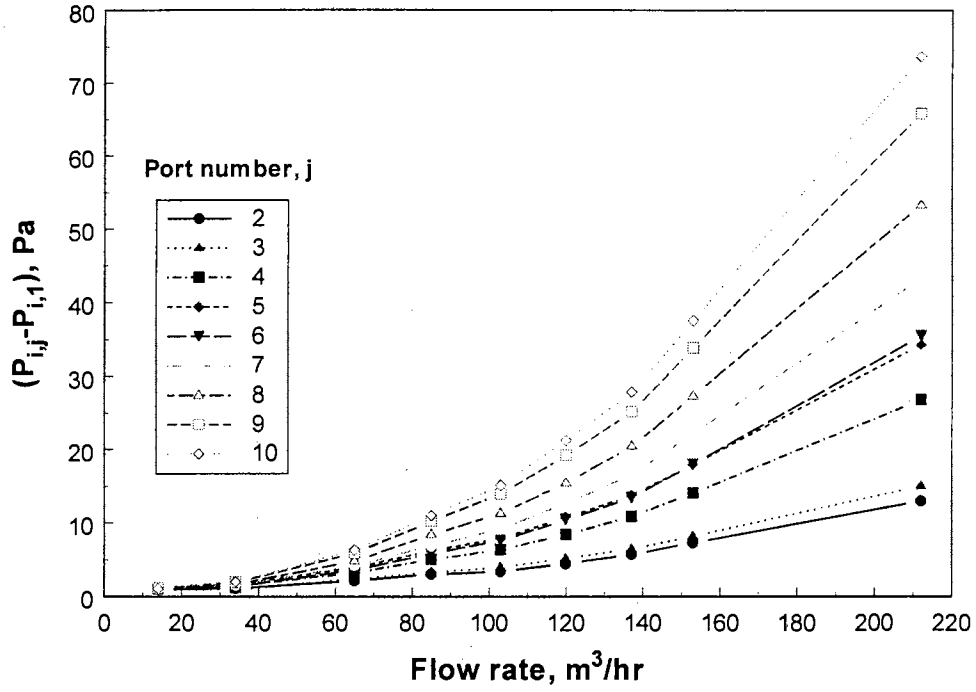


Figure D.5: Pressure distributions in inlet plenum (filter with an additional sheet)

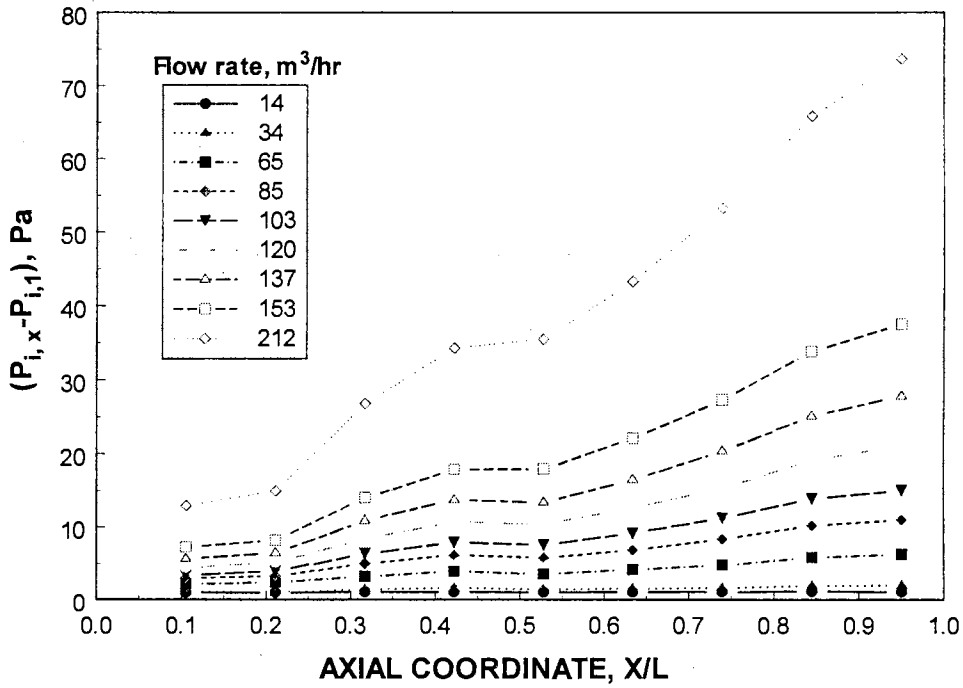


Figure D.6: Pressure distributions in inlet plenum along the filter (filter with an additional sheet)

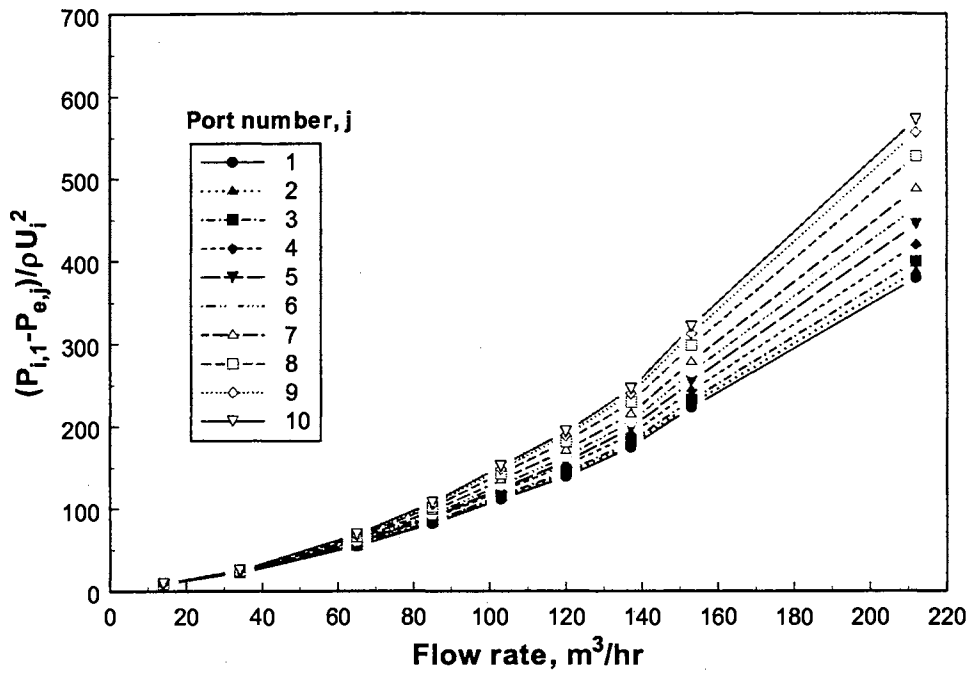


Figure D.7: Pressure distributions in exit plenum (filter only)

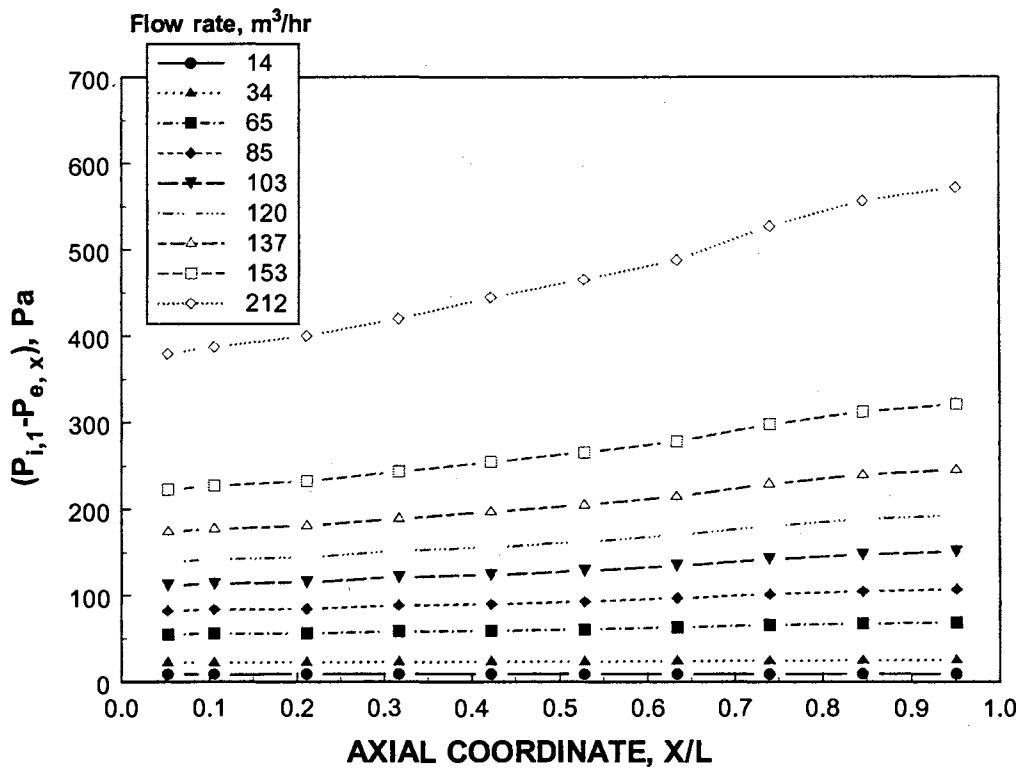


Figure D.8: Pressure distributions in exit part along the filter (filter only)

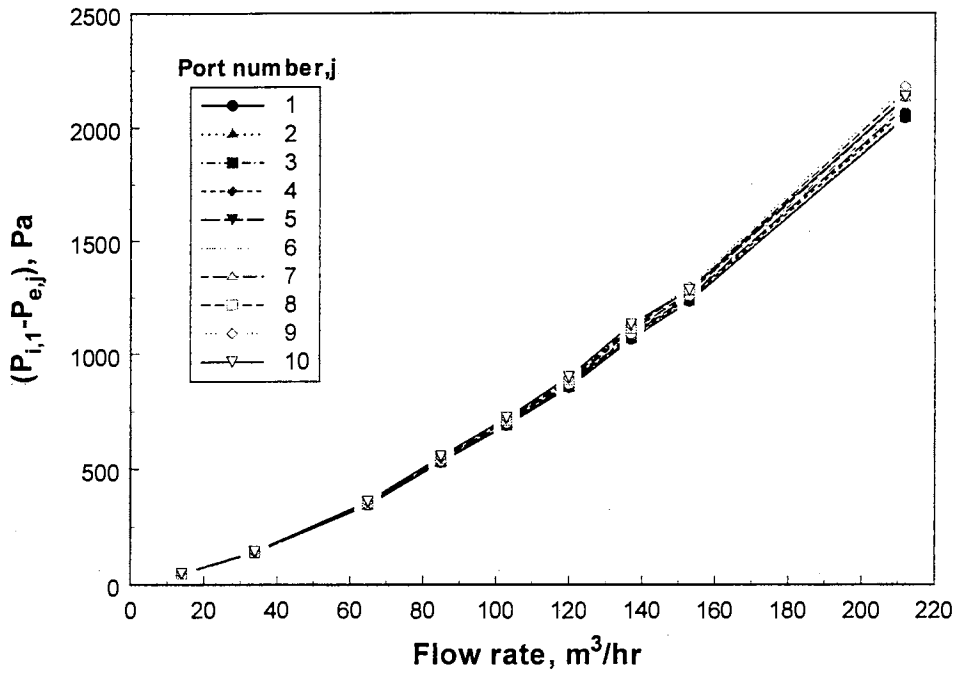


Figure D.9: Pressure distributions in exit plenum (filter with an additional sheet)

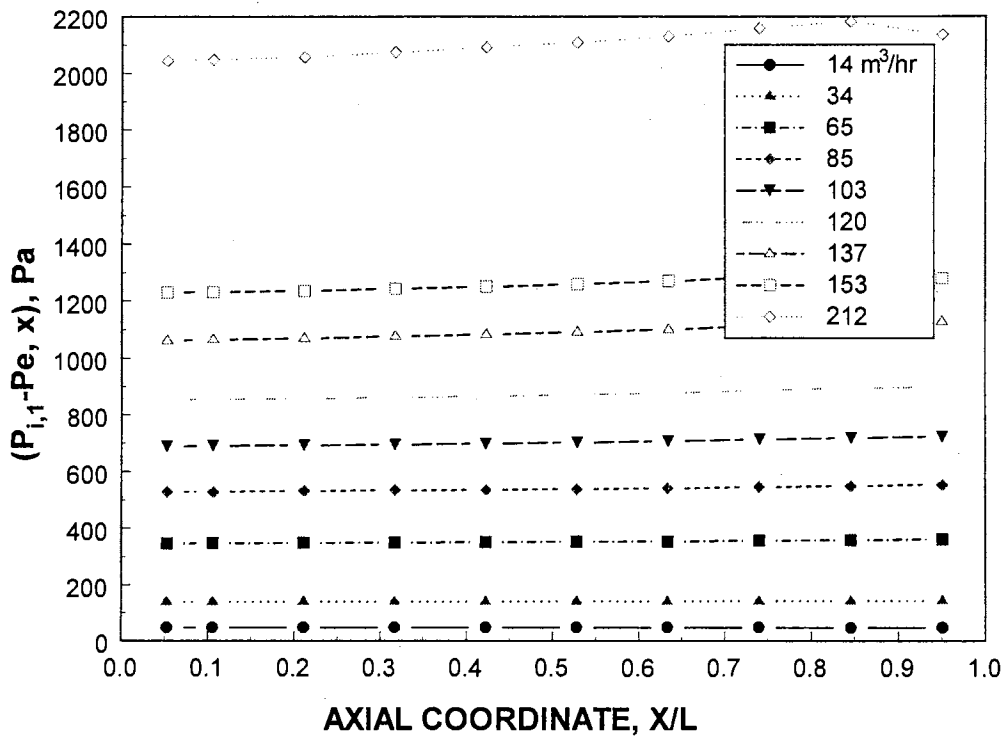


Figure D.10: Pressure distributions in exit part along the filter (filter with an additional sheet)

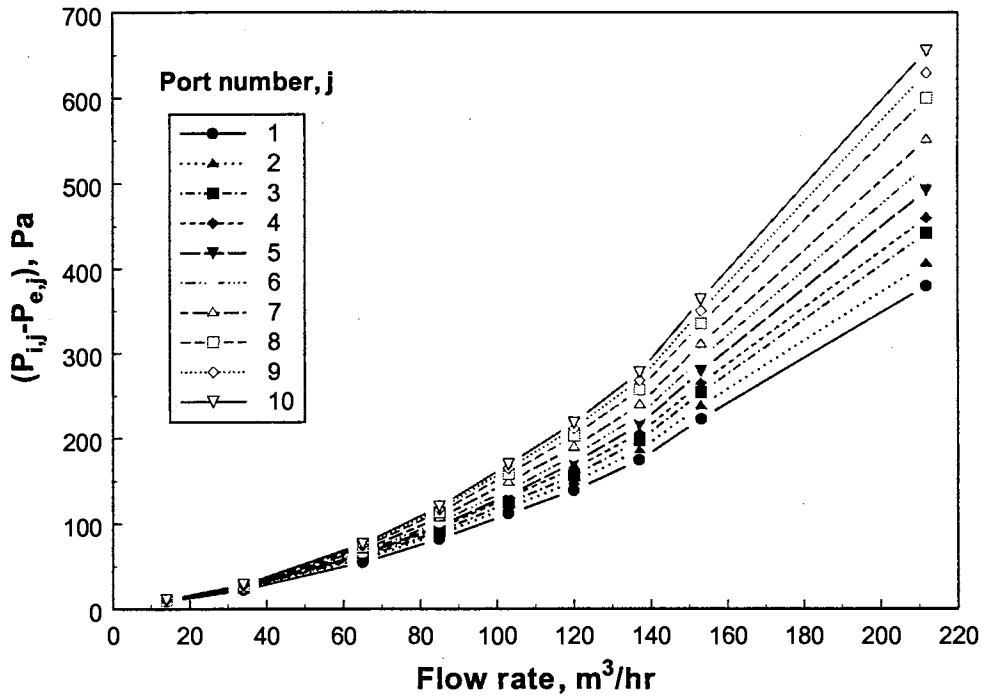


Figure D.11: Pressure drop across the filter (filter only)

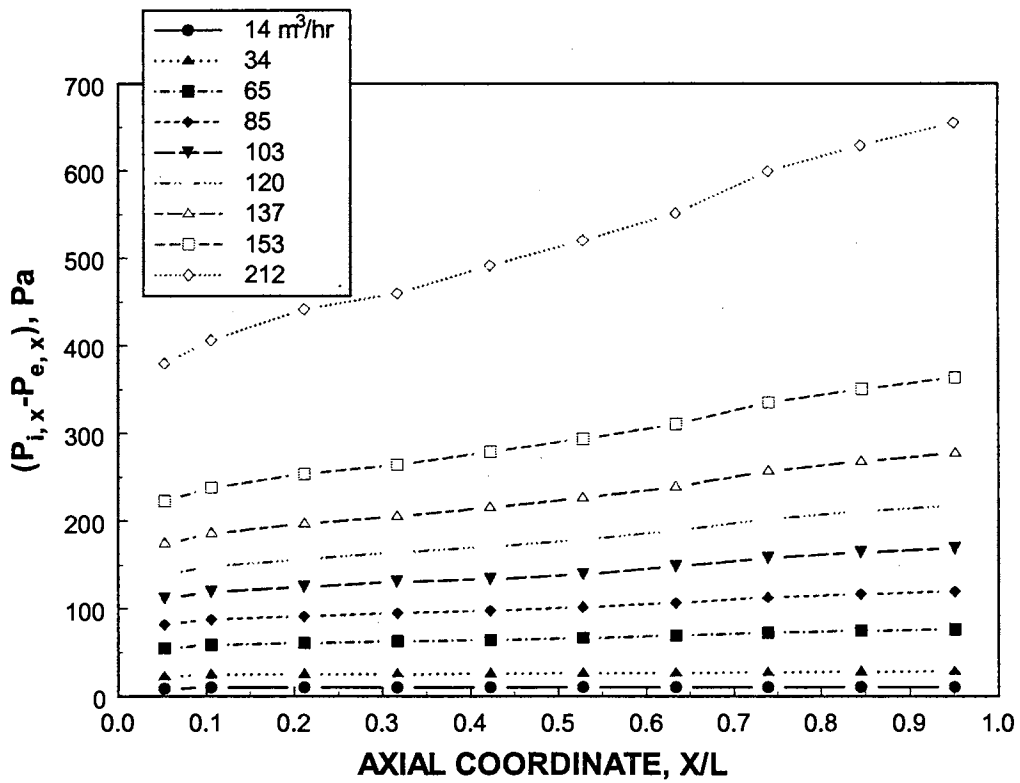


Figure D.12: Pressure distributions across the filter (filter only)

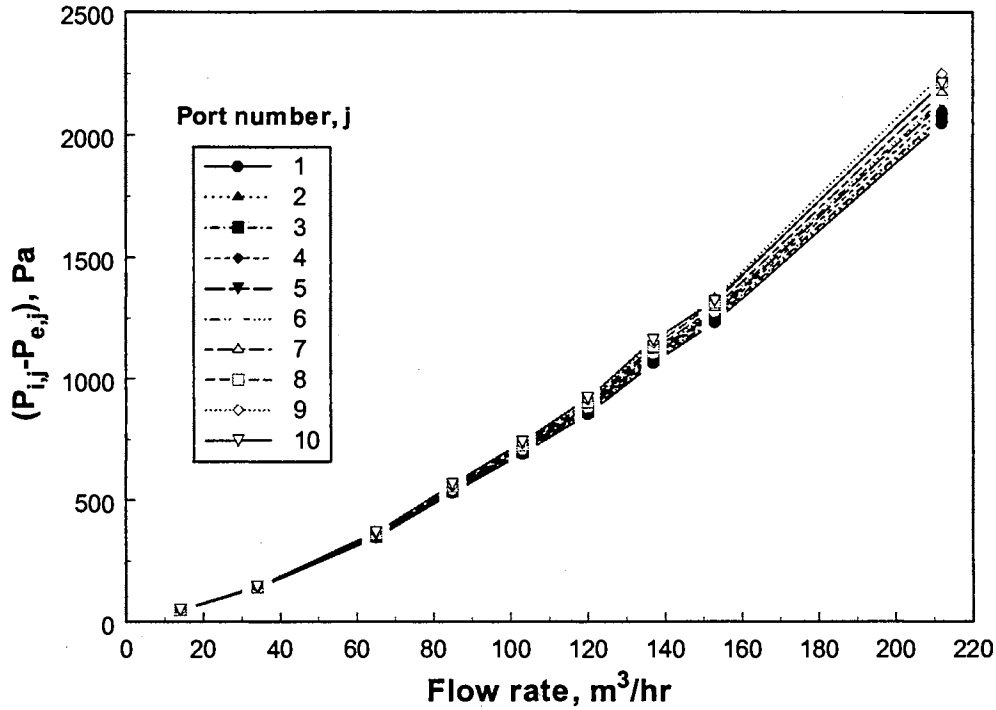


Figure D.13: Pressure distributions across the filter (filter with an additional sheet)

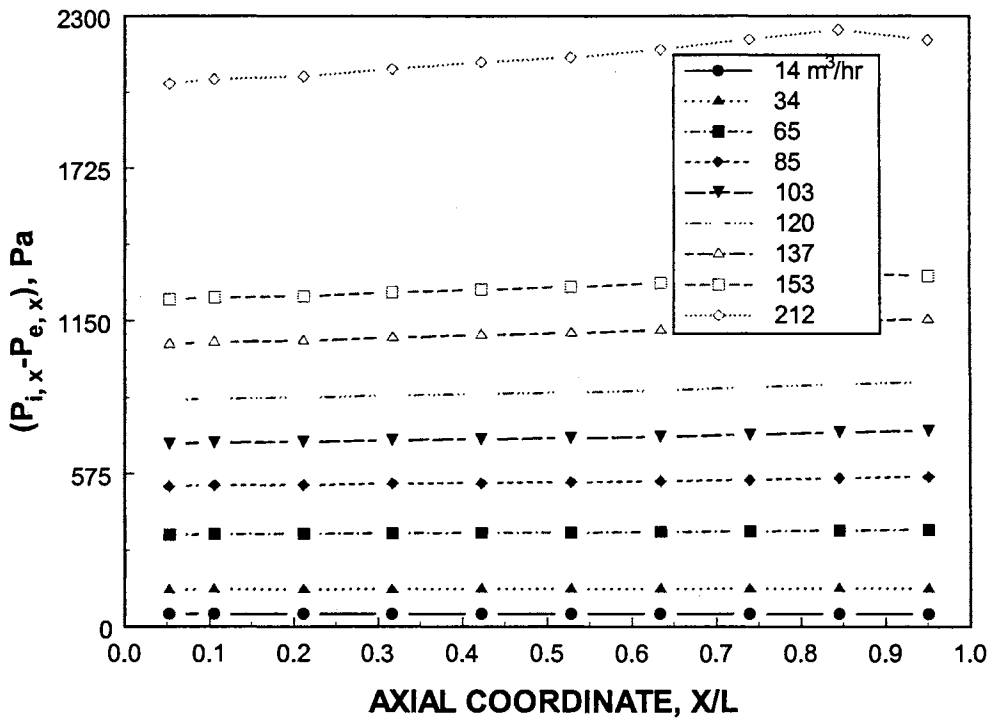


Figure D.14: Pressure distributions across the filter (filter with an additional sheet)

APPENDIX E

Axial and normal velocity distributions at different heights above the filter are presented in this appendix. These measurements were performed at the centerline of the filter. The two horizontal beams measure the axial velocity and the two vertical beams measure the normal velocity. The two horizontal beams can go very close to the surface of the filter since the axis of these two beams is parallel to the filter surface. The vertical beams can not go very close to the surface of the filter since the axis of these two beams is orthogonal to the surface of the filter. The lower beam will hit the filter and disappear as it goes very close to the surface of the filter.

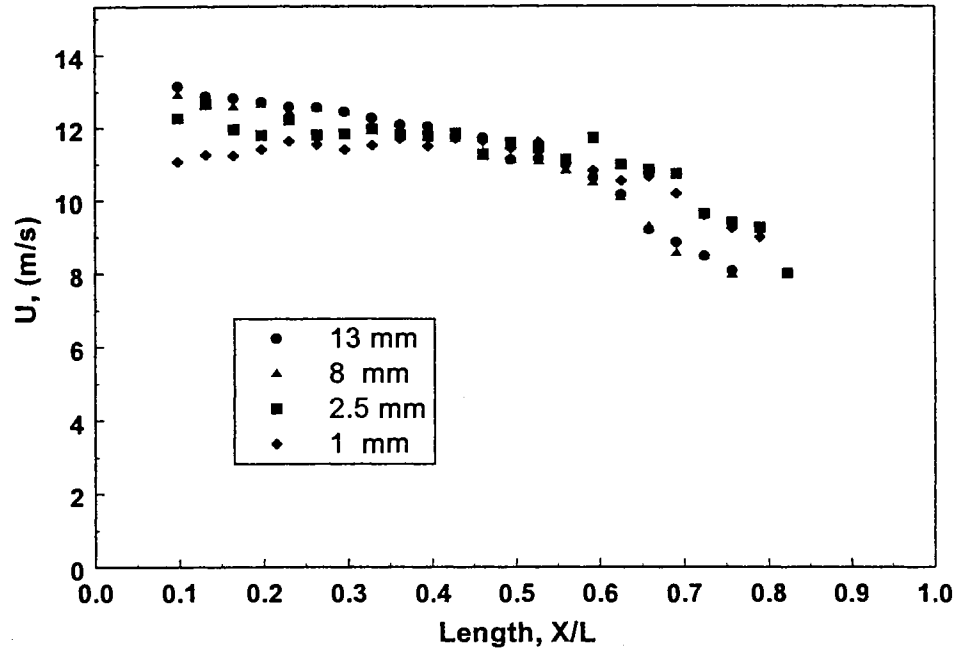


Figure E.1: Axial velocity distribution at different heights above the filter

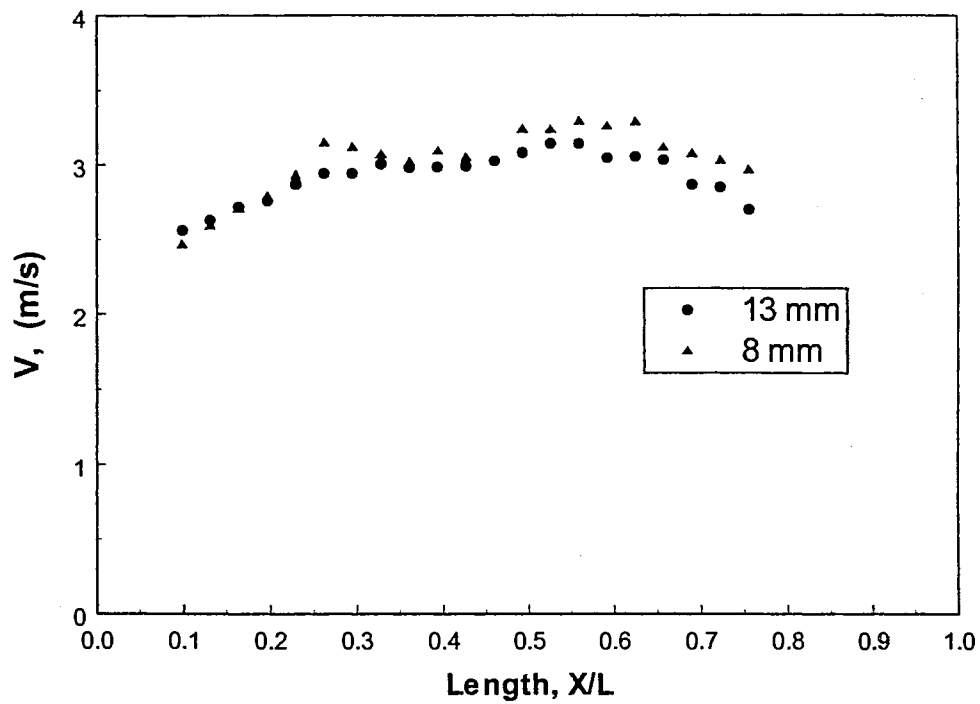


Figure E.2: Normal Velocity distribution at different heights above the filter

APPENDIX F

A comparison between two different profiles resulted from the optimization program is presented in this section. Figure F.1 shows the two profiles and Table F.1 shows a comparison of all statistical parameters corresponds to every profile.

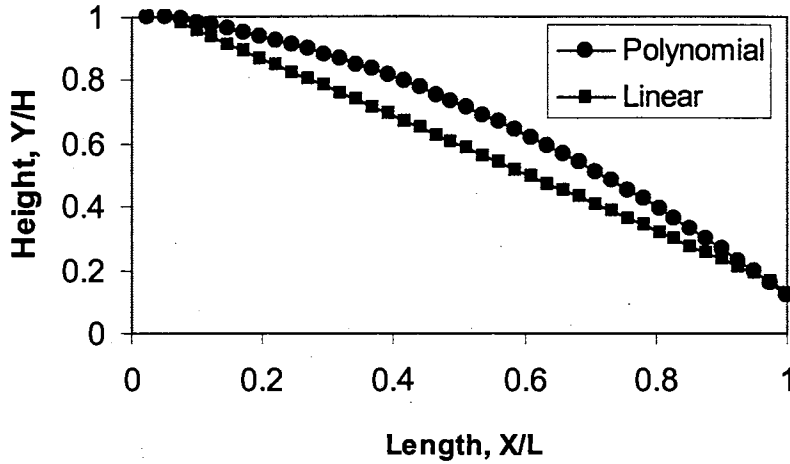


Figure F.1: Different housing roof profiles from the optimization program

	Linear Profile	Polynomial Profile
PHI (Optimized function)	0.021	0.170
RMSE	0.114	0.281
AAPD	1.36 %	5.24 %
WRMS	1.17 %	2.29 %

Table F.1: Statistical parameters of two profiles resulting from the optimization program
 The statistical parameters in Table F.1 are defined in section 2.3.3, The parameter PHI is the sum of the squares defined in equation 2.27 (optimized function). The linear profile shows less value of the optimized function and the other parameters, means that the linear profile is better.

VITA

Abdel Salam Al-Sarkhi
Candidate for the degree of
Doctor of Philosophy

Thesis: OPTIMIZATION TECHNIQUE FOR DESIGN OF AUTOMOTIVE AIR
FILTER HOUSINGS WITH IMPROVED FLUID DYNAMIC PERFORMANCE

Major Field: Mechanical Engineering

Biographical:

Personal Data: Born in Zarka, Jordan, March 1, 1968, son of Mohammed and Amenah Al-Sarkhi

Education: Graduated from Jordan University of Science and Technology in 1990, Irbid, Jordan in 1991 with a Bachelor of Science degree in Mechanical Engineering. In 1993 received Master of Science degree in Mechanical Engineering from the same school. Completed the requirements for the Doctor of philosophy degree at Oklahoma State University in December 1999.

Professional Experience: Teaching Assistant, School of Mechanical and Aerospace Engineering, January 1999 to December 1999.

Research Assistant, School of Mechanical and Aerospace Engineering, January 1996 to January 1999.

Design Engineer, Karl Wess factory/Molds and Spare Parts Company, Austria/Jordan, Design and maintenance of different types of Molds (Plastic Injection, Blow and Die Casting molds), March 1994 to April 1995.

Design Engineer, AMARAH Consulting Engineering, Design and lay out of air-conditioning systems for residential and commercial buildings, September 1993 to March 1994.

Name: Abdel Salam Al-Sarkhi

Date of Degree: December, 1999

Institution: Oklahoma State University

Location: Stillwater, Oklahoma

Title of Study: OPTIMIZATION TECHNIQUE FOR DESIGN OF AUTOMOTIVE AIR FILTER HOUSING WITH IMPROVED FLUID DYNAMIC PERFORMANCE

Pages in Study: 178

Candidate for the Degree of Doctor of Philosophy

Major Field: Mechanical Engineering

Scope and Method of Study: Automotive air filter housings often are designed with major consideration given to fitting the available space rather than to providing the filter with a well-behaved, uniform flow. The development of a filter housing design technique that determines the housing geometry required to provide a user-specified velocity distribution through the filter was accomplished. Computations were performed for the case of a uniform velocity distribution through the filter. The uniform velocity distribution corresponds to a uniform, constant pressure drop across the filter from the upstream to the downstream side. Computational Fluid Dynamic (CFD) calculations of the viscous laminar flow upstream and downstream of the filter were performed using 2-D Navier-Stokes equations. A computational optimization method was applied to minimize the variation in the pressure drop along the filter by changing the geometry of the upper wall. As the upper wall is moved, the CFD solution for the computations is repeated and the pressure drop variation is re-evaluated. An experimental verification was performed using a model filter housing constructed with the geometry specified by the results of the computational design technique. A Laser Doppler Anemometer (LDA) was used to measure the velocity distribution above the filter.

Findings and Conclusions: The optimization results have produced a pressure distribution that is very close to the specified uniform distribution. The measured velocity distributions in this housing were compared with measured velocity distributions for different housing models. The model designed with the computational technique shows a much more uniform flow distribution above the filter than the other housings. The pressure distribution across the filter was measured using a pressure transducer. A filtration model was used with the measured velocity distributions, predicting local efficiency distributions and overall filter efficiencies. The results show that filter resistance and housing geometry can have large effects on the flow field. The filter efficiency is strongly dependent on the flow field. Hence the housing geometry and filter resistance may have significant effects upon filter efficiency for both smaller and larger particles.

ADVISER'S APPROVAL FRANK Chambers